Adaptive Mesh Euler Equation Computation of Vortex Breakdown in Delta Wing Flow

by

David Laurence Modiano

S. B. Massachusetts Institute of Technology (1987)
S. M. Massachusetts Institute of Technology (1989)

SUBMITTED TO THE DEPARTMENT OF
AERONAUTICS AND ASTRONAUTICS
IN PARTIAL FULFILLMENT OF THE REQUIREMENTS
FOR THE DEGREE OF

Doctor of Philosophy
at the
Massachusetts Institute of Technology

February 1993

Signature of Author _____
Department of Aeronautics and Astronautics
February, 1993

Certified by _____
Professor Earll M. Murman
Thesis Supervisor, Head, Department of Aeronautics and Astronautics

Certified by _____
Professor Mårten Landahl
Department of Aeronautics and Astronautics

Certified by _____
Dr Michael B. Giles
Rolls-Royce Reader in CFD, Oxford University

Accepted by _____
Professor Harold Y. Wachman
Chairman, Department Graduate Committee

Adaptive Mesh Euler Equation Computation of Vortex Breakdown in Delta Wing Flow

by

David Laurence Modiano

Submitted to the Department of Aeronautics and Astronautics
on January 28th, 1993
in partial fulfillment of the requirements for the degree of
Doctor of Philosophy in Aeronautics and Astronautics

A solution method for the three-dimensional Euler equations is formulated and implemented. The solver uses an unstructured mesh of tetrahedral cells and performs adaptive refinement by mesh-point embedding to increase mesh resolution in regions of interesting flow features. The fourth-difference artificial dissipation is increased to a higher order of accuracy using the method of Holmes and Connell. A new method of temporal integration is developed to accelerate the explicit computation of unsteady flows. The solver is applied to the solution of the flow around a sharp edged delta wing, with emphasis on the behavior of the leading edge vortex above the leeside of the wing at high angle of attack, under which conditions the vortex suffers from vortex breakdown. Large deviations in entropy, which indicate vortical regions of the flow, specify the region in which adaptation is performed. Adaptive flow calculations are performed at ten different angles of attack, at seven of which vortex breakdown occurs. The aerodynamic normal force coefficients show excellent agreement with wind tunnel data measured by Jarrah, which demonstrates the importance of adaptation in obtaining an accurate solution. The pitching moment coefficient and the location of vortex breakdown are compared with experimental data measured by Hummel and Srinivasan, with which fairly good agreement is seen in cases in which the location of breakdown is over the wing. A series of unsteady calculations involving a pitching delta wing were performed. The use of the acceleration technique is validated. A hysteresis in the normal force is observed, as in experiments, and a lag in the breakdown position is demonstrated.

Thesis Supervisor: Earll M. Murman,
Head, Department of Aeronautics and Astronautics

Acknowledgments

Sometimes a scream is better than a thesis.

Ralph Waldo Emerson

There have been many times during the past five (three, sir) ...three years that could have driven me to scream. I would like to thank all those who have prevented me from needing to do so. First and foremost is my advisor, Earll Murman, who helped me through a thesis that was more (or at lest seemed) trouble-ridden than most. I am also grateful to my other committee members, Mårten Landahl and Mike Giles, for their insightful comments and last-minute intercontinental discussions. In addition, Mark Drela helped me understand the practical aerodynamic aspects of this work. This thesis also owes a lot to Liz Zotos, departmental graduate administrator. I would also like to thank Lori Martinez, for being such a nice person, and for always maintaining a supply of interesting food items for public consumption.

I would also like to thank my colleagues at the Cluster, first among them Dana Lindquist and Dave Darmofal, fellow long-term survivors and system maintainers; and my office-mates Yannis Kallinderis, Sandy Landsberg, Brian Nishida, and Eric Sheppard. Life here would have been much grimmer without the Thursday evening custom of trips to the Cambridge Brewery. I'd like to thank Bob Haimes, Gerry Guenette and Mike Giles for starting this tradition.

I'd also like to thank the residents of Jürgendûr and Ikayama, and the members of the West Somerville Alumni Association — namely Rob, Laura, Susie, Phil, Brian, Eon, Dave, David, Charles, John, Donna, Francis, Kate, Mike, Derrick, and Glenn — for being cool neighbors; and other members of the midnight Illuminati crowd, for helping me get less sleep :)

And last, but by no means least, I owe a lot to my parents, for always believing that I could finish this, even when I didn't believe it myself.

This research was supported by Air Force Office of Scientific Research contract number AFOSR-89-0395A, monitored by Dr. L. Sakell; and by the McDonnell Aircraft Company, under MDC/MDRL IRAD Sponsorship. The mesh generation system was provided by Jaime Peraire of the Imperial College of Science, Technology, and Medicine, London, England, and Ken Morgan of the University College of Swansea, Wales. Three-dimensional visualization was performed using VISUAL3, developed by Robert Haimes of MIT.

Contents

List of Figures

List of Tables

Nomenclature

Refer also to sections 2.4 and 2.5.

Roman symbols

a	speed of sound
$\vec{a}$	fluid acceleration
b	wing span
$\vec{b}$	unit binormal vector
c	wing chord
c_R	wing root chord
$\bar{c}$	wing mean aerodynamic chord
c_p	coefficient of pressure
c_{p_0}	coefficient of total pressure
C	characteristic vector
C_n	chordwise coefficient of lift
C_D	coefficient of drag
C_L	coefficient of lift
C_N	coefficient of normal force
C_M	coefficient of pitching moment
D	artificial dissipation
D	wing drag
$\mathcal{D}^2$	second difference operator
e	internal energy per unit mass
E	total internal energy per unit mass
f	time step acceleration factor
$\vec{F}$	flux vector
F, G, H	Cartesian components of flux vector
h	total enthalpy
h_r	total rothalpy
J	Jacobian
J^{-1}	inverse Jacobian
k	reduced frequency
$\mathcal{K}$	nondimensional pitching rate
L	wing lift
$\mathcal{L}$	Lagrangian function
M	mass matrix
M	wing pitching moment

M	Mach number
$\vec{n}$	surface unit normal vector
n	surface normal coordinate
N	wing normal force
N	interpolation function
$\tilde{N}$	test function
N_C	number of mesh cells
N_E	number of mesh edges
N_P	number of mesh nodes
p	fluid static pressure
p_0	fluid total pressure
q	fluid speed
Q	a quantity
$\vec{r}$	position vector
r	not quite the spectral radius
R	residual vector
R_X, R_Y, R_Z	residual matrices
R_{in}, R_{out}	Riemann invariants
s	entropy
s	shock smoothing switch
$\vec{S}$	face area vector
S	source vector
$\vec{t}$	unit tangent vector
t	time
t	wing thickness
u, v, w	Cartesian components of fluid velocity
$\vec{v}$	fluid velocity
U	state vector
V	cell or supercell volume
x, y, z	Cartesian coordinates

Greek symbols

α	angle of attack
$\alpha_1, \ldots$	Runge-Kutta coefficients
β	angle of yaw
β	wing leading and trailing edge bevel angle
γ	ratio of specific heats
Δt	time step
Δp_0	total pressure loss
ε_2, ε_4	empirical coefficients of second- and fourth-difference smoothing terms
ε_i^C	weights for fourth difference smoothing terms
ζ_1, ζ_2, ζ_3, ζ_4	tetrahedral volume coordinates
λ	Courant-Friedrichs-Levy number
λ_x, λ_y, λ_z	Lagrange multipliers

Greek symbols

Λ	characteristic matrix
Λ	wing leading edge sweepback angle
ρ	fluid density
ω	rotational velocity
Ω	angular frequency

Subscripts and superscripts

$()_\infty$	free stream
$()_a$	in absolute (inertial) frame of reference
$()_i$	mesh node quantity
$()_i$, $()_j$, $()_{ij}$	tensor indicial notation
$()_n$	in surface normal direction
$()_r$	in rotational (noninertial) frame of reference
$()_w$	at solid wall
$()^C$	mesh cell quantity
$()^F$	mesh face quantity
$()^*$	nondimensionalized quantity

Chapter 1

Introduction

> We never see the beginning. We come in after the lights have gone down and try to make sense of what we have seen.
>
> Neil Gaiman
> *The Sandman*

The latest generation of high performance fighter aircraft are being designed to be capable of extreme maneuvers, which require the aircraft to fly at very high angles of attack that previous aircraft were designed to avoid. At these extreme angles of attack, the leading edge vortex that forms above the aircraft's delta wing suffers breakdown, which degrades the aircraft's handling characteristics. In this section, the delta wing leading edge vortex, and the phenomenon of vortex breakdown are described, and a set of wind tunnel experiments of a pitching delta wing are summarized. In addition, previous numerical simulations involving leading edge vortex flows, and vortex breakdown, are mentioned.

1.1 Background

The aerodynamics of delta wing flows is of great interest for two main reasons. The first is that when a symmetric and stable set of vortices forms, the wing experiences an increase in lift and aerodynamic moments, leading to enhanced aircraft maneuverability. The second is that an asymmetric or unstable set of vortices can cause a loss in lift and

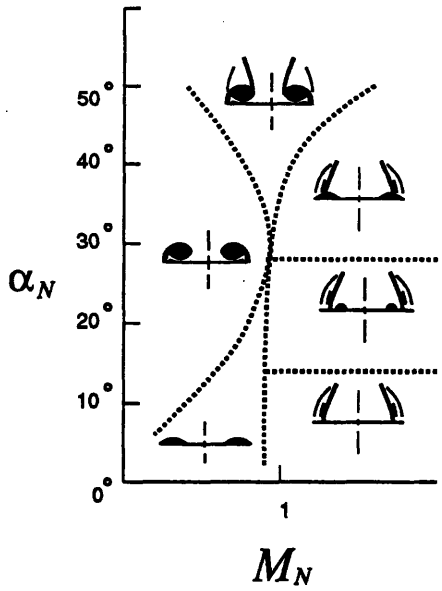

Figure 1.1: Classification of delta wing flow regimes [53]

a strong rolling moment, even with no angle of yaw. Either of these consequences can lead to disaster for a maneuvering aircraft.

Stanbrook and Squire [76], and later Miller and Wood [53], classified the various regimes of flow behavior around a delta wing. The classification system of Miller and Wood is summarized in figure 1.1, in terms of the Mach number and angle of attack normal to the leading edge of the wing. These quantities are defined to be

$$M_N = M_\infty \cos\Lambda \sqrt{1 + \sin^2\alpha \tan^2\Lambda} \tag{1.1}$$

$$\alpha_N = \tan^{-1}\frac{\tan\alpha}{\cos\Lambda} \tag{1.2}$$

in which Λ is the sweep angle of the leading edge of the wing. The regime at low normal Mach number and moderate angle of attack is that which involves separation at the leading edge, and is the regime in which the flows of interest in this thesis occur.

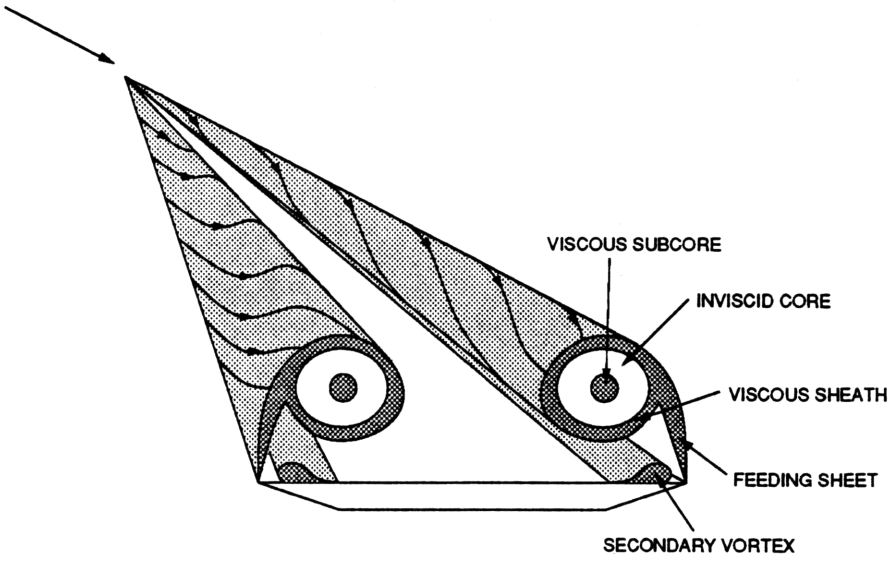

Figure 1.2: Leading edge vortex structure

1.1.1 Leading Edge Vortex Structure

At sufficiently high angle of attack, the fluid flow will separate at the leading edge of a delta wing, resulting in the formation of a large pair of primary vortices above the lee side of the wing. A large body of experimental investigations of the leading edge vortex structure indicates that the vortex can be divided into three parts, each with its own distinctive properties. The structure is shown in figure 1.2. The feeding sheet, or umbilical shear layer, is a viscous thin shear layer emanating from the leading edge of the wing. The vortex itself has two parts. The outer core is a nearly inviscid, rotational region of mostly conical flow. Towards the center of the core the axial velocity is seen to increase dramatically. At the center of the core is the viscous subcore, at the outer edge of which the swirl velocity reaches a maximum, and the axial velocity continues to increase to a maximum at the axis. At the center of the viscous subcore the swirl velocity must vanish. The difference between maximum swirl velocity at the edge of the subcore and zero on the axis causes viscous dissipation which is largely independent of Reynolds number. In addition, Lee [42] describes a model, based on experimental data gathered by Verhaagen and van Ransbeeck [84], in which the rotational core is separated from the external, irrotational flow by a viscous shear layer called the viscous sheath,

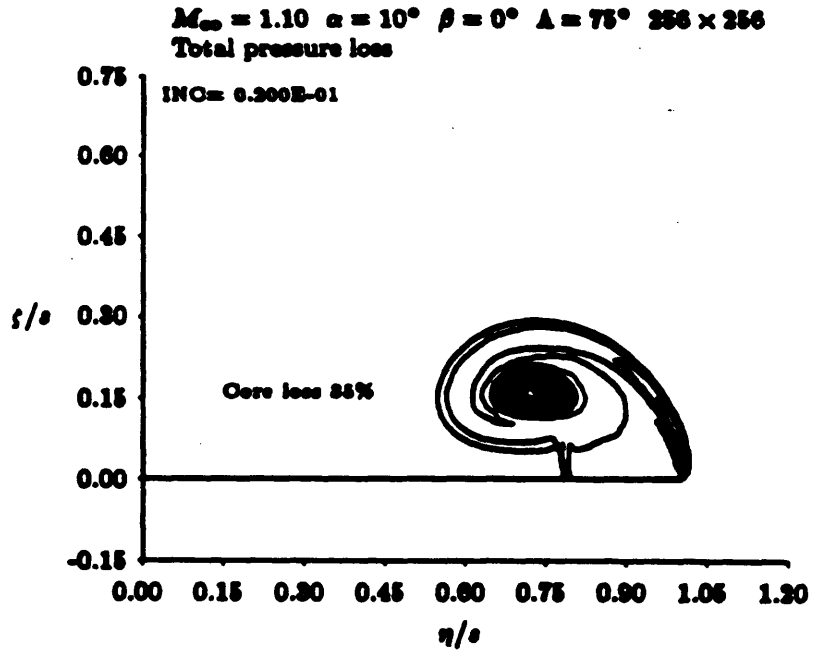

Figure 1.3: Fine mesh conical flow solution from Powell [64], possibly showing the viscous sheath.

which is formed as the feeding sheet rolls up and intersects with itself. Conical flow Euler solutions by Powell [64], one of which is shown in figure 1.3, also provide evidence for the existence of the viscous sheath. Due to the use of the Euler model, the effects of viscosity upon the solution in figure 1.3 are due only to the artificial dissipation and truncation error.

The flow on the leeward surface of the wing is accelerated due to the proximity of the vortex, resulting in a region of lower pressure which increases the lift and pitching moment of the wing. A secondary vortex forms due to boundary layer separation in the adverse pressure gradient as the fluid moves outboard from the pressure minimum directly beneath the primary vortex. Similarly, a tertiary vortex can also appear due to separation beneath the secondary vortex. Simulation of the secondary and tertiary vortices requires the inclusion of viscous effects. The characteristics of the secondary vortex has been shown to affect the structure of the primary vortex in transonic flow conditions [54], but not in supersonic flow [50].

Some experimental investigations into the characteristics of delta wing flow were performed by Earnshaw [16], Hummel [28], Verhaagen and Kruisbrink [85] and Verhaagen

and van Ransbeeck [84], who measured velocity and pressure in the region of the vortex, and Fink and Taylor [19], who studied the variation of total pressure. More recently, Kjelgaard and Sellers [37, 36] and Roos and Kegelman [70] performed exhaustive flow field surveys.

The numerical solution of delta wing flows can sometimes be simplified by use of the conical assumption, in which flow quantities are taken to be constant on rays emanating from the apex of the wing. This simplification is only valid for supersonic flow of an inviscid fluid around a sharp edged wing of a suitable shape. Powell [64] performed a study of leading edge vortex flows with the use of embedded structured grids to increase resolution. Batina [7, 5] formulated and solved the conical Euler equations using an unstructured mesh of triangles, and adaptive refinement, and Kandil and Chuang [35] used the conical model to study the unsteady flow that results from a rolling wing.

Fully three-dimensional solutions of delta wing flow are necessary in situations in which streamwise variations occur. Rizzi *et al.* [68, 55, 67] have performed numerous calculations, particularly for transonic flows. Melton [51] performed adaptive computations in three dimensions using hexahedral cells, and Borsi *et al.* [10] made use of adaptation using a mesh of tetrahedral cells. In addition, in the absence of vortex breakdown simpler models can provide accurate solutions. An example is the method developed by Tavares [78] using slender wing theory with an explicit vortex wake.

1.1.2 Vortex Breakdown

Vortex breakdown, also known as vortex bursting, is a phenomenon that was first observed in delta wing flows by Peckham and Atkinson in 1957 [58], and was studied in detail by Lambourne and Bryer [39]. It occurs when a vortex is subjected to a sufficiently strong adverse pressure gradient. The basic features of vortex breakdown are a sudden enlargement of the vortex core, followed by a stagnation region on the axis. The vortex that reforms downstream of breakdown is often diffuse and erratic. Two types

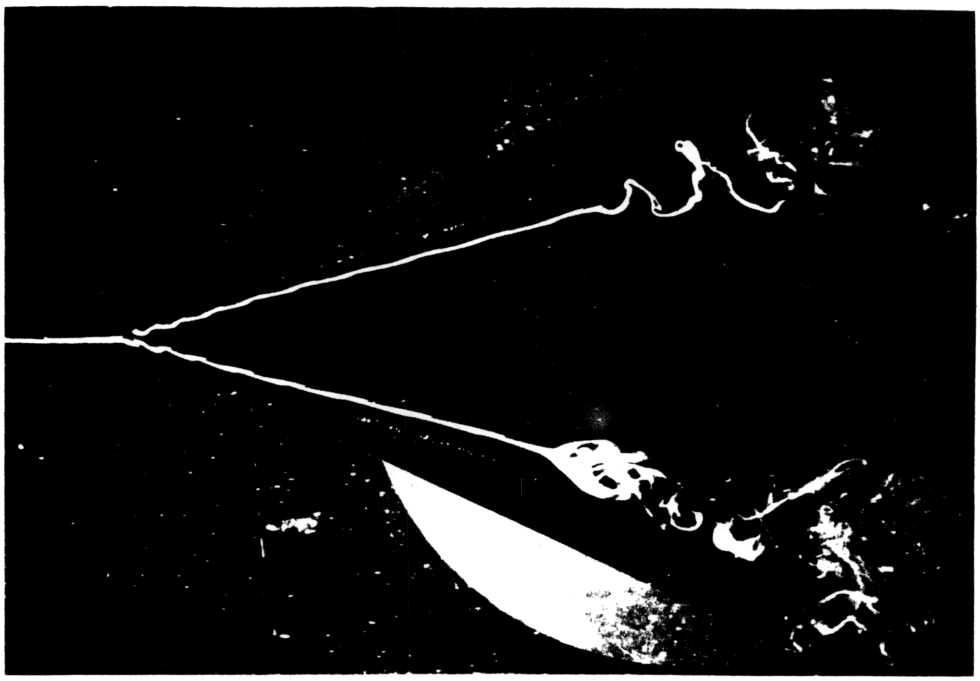

Figure 1.4: Flow visualization of vortex breakdown over a delta wing

of vortex breakdown can be seen in figure 1.4, from Lambourne and Bryer. The upper vortex is experiencing the axisymmetric "bubble" type of breakdown, while the lower vortex is undergoing the asymmetric "spiral" type of breakdown. Breakdown has also been observed [57] to alternate periodically in time between the bubble and spiral types, and Sarpkaya [72] reports forms of breakdown intermediate between the two types. The effects of vortex breakdown are a significant decrease in lift and pitching moment, and a large rolling moment due to the possibility of asymmetric breakdown (such as appears in figure 1.4). The deleterious effects of vortex breakdown increase with the angle of attack of the wing, as the location of breakdown moves forward from the trailing edge.

The flow conditions under which vortex breakdown occurs in incompressible flow are summarized in figure 1.5. The angle of attack at which breakdown appears decreases as the sweep angle Λ decreases, which is to say, as the wing becomes less slender. For very slender wings, asymmetrical vortex lift-off occurs, in which one leading edge vortex retreats from the wing surface, while the other approaches the wing. This produces an anomalous rolling moment, and can lead to an oscillatory motion called wing rock [56, 11].

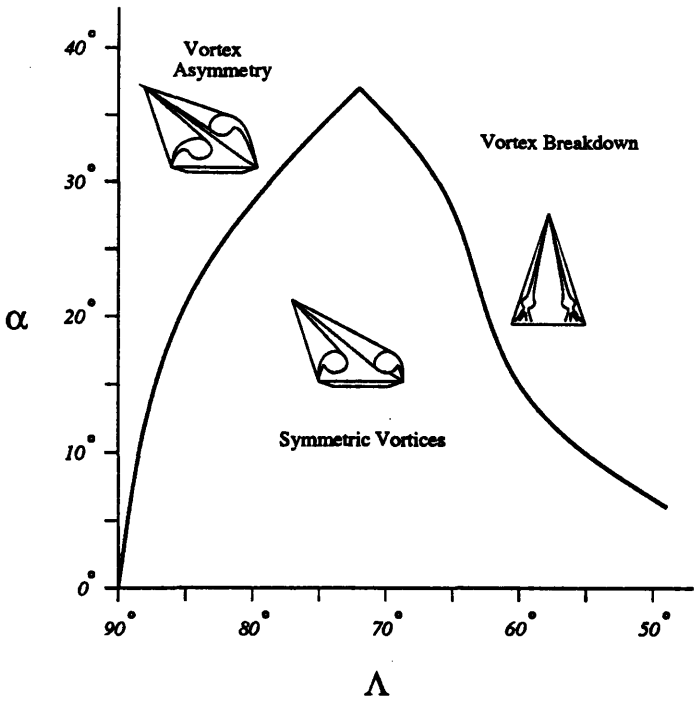

Figure 1.5: Flow conditions leading to vortex breakdown ad vortex lift-off in incompressible flow [63]

Surveys of vortex breakdown in general and proposed theoretical explanations of it are presented by Landahl and Widnall [40], Hall [25], Leibovich [43] and Escudier [18]. Numerical investigation of the breakdown process was first performed by Grabowski and Berger [23] for the axisymmetric breakdown in a swirling pipe flow. Numerical simulations of vortex breakdown over a delta wing have also been reported. Fujii and Kutler [20] possibly captured the onset of breakdown, with more demonstrative calculations being performed by Thomas, Krist and Anderson [80], Hartwich, Hsu, Luckring and Liu [26], Ekaterinas and Schiff [17], Agrawal, Barnett and Robinson [1], Deese, Agarwal and Johnson [15] and Webster and Shang [87]. The bubble type of breakdown was specifically noted by Thomas *et al.* and by Ekaterinas and Schiff, while Webster and Shang characterized their solution as the spiral type of breakdown.

1.1.3 Pitching Delta Wing

Modern fighter aircraft are being designed to perform extreme maneuvers, known as "supermaneuvers," which involve flight at very high angles of attack, where vortex

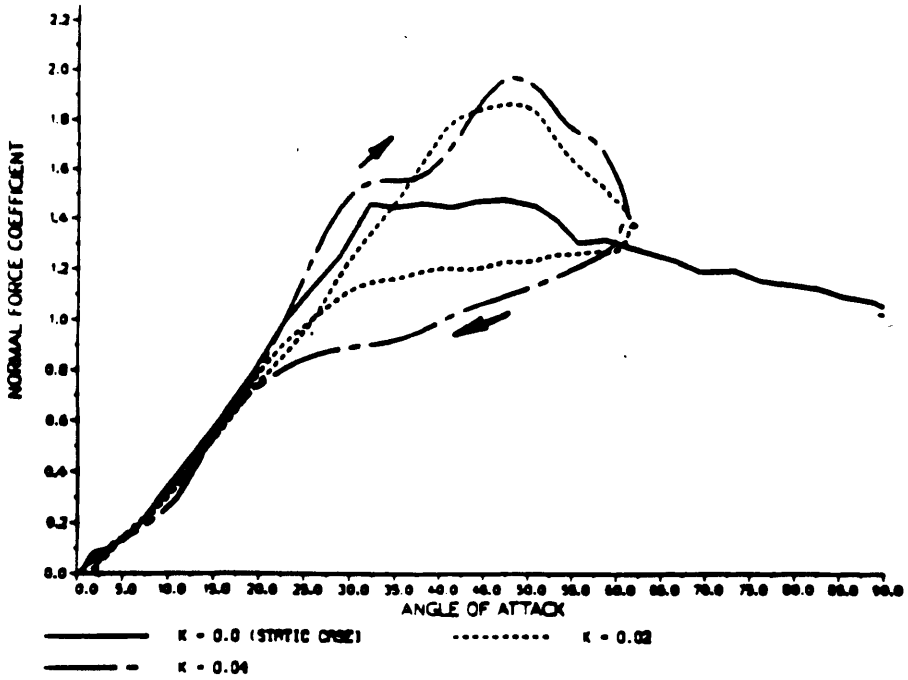

Figure 1.6: Measured aerodynamic coefficients on a pitching delta wing [31, 32]

breakdown is likely to occur. Previous aircraft have been designed to remain at lower angles of attack to avoid vortex bursting and wing stall. In order to study aircraft performance in this extreme flight regime, Jarrah [32, 31] analyzed three canonical supermaneuvers and determined that the aircraft dynamics could be represented by either a sinusoidal or a ramp variation of angle of attack. Jarrah then subjected a delta wing in a low-speed wind tunnel to pitching motions with both the sinusoidal and ramp variation, and found a large hysteresis in the unsteady aerodynamic forces on the wing, as shown in figure 1.6. The hysteresis persisted even at low reduced frequencies at which Jarrah expected to observe quasi-steady flow. Jarrah attributed the hysteresis to a lag in the vortex breakdown, whereby the angle of attack at which the vortex breaks down during the upward motion is greater than the angle of attack at which the vortex re-establishes itself during the downward notion. Experiments by Thompson, Batill, and Nelson [81] also indicate the lag in burst location. It is the goal of this work to simulate the unsteady flow around a pitching delta wing and study the behavior of vortex breakdown in this flow. Jarrah and Thompson *et al.*, both found the effect of Reynolds number on this flow to be weak, so that the Euler equations are adequate to simulate the flow around a sharp-edged delta wing. The unsteady flow around a pitching wing for very small amplitudes of motion was studied by Kandil and Chuang [34].

1.2 Validity of the Euler Equations

In general, there are two conditions for the validity of the Euler equations for modeling delta wing flows. First, the wing geometry must have a sharp leading edge to provide a Kutta condition for flow separation, and second, the flow solution algorithm must provide a dissipative mechanism to bring the swirl velocity to zero at the vortex core. The wing geometry used for all computations in this thesis has a sharp leading edge, and the artificial dissipation added to the flow solution scheme serves the latter purpose. Experimental investigations indicate that a changing Reynolds number does not affect the structure of the primary vortices [37] or the lift variation with angle of attack [70]. There is also evidence [72] that in the high Reynolds number limit the behavior or vortex breakdown also is independent of Reynolds number.

1.3 Thesis Summary

The goal of the present research is the application of adaptive refinement via mesh-point embedding to the solution of the unsteady inviscid flow around a pitching sharp-edged delta wing. The main body of the thesis is divided into three parts. In chapter two, the governing equations for the flow of an inviscid, ideal gas, the Euler equations, will be presented in an inertial reference frame, and transformed into a rotating reference frame fixed to the wing. Also, suitable physical boundary conditions will be discussed. In chapter three, the procedure for solving the Euler equations numerically will be described. This includes the spatial discretization by means of the Galerkin finite element method, the artificial dissipation with the Holmes-Connell extension, the temporal integration procedure, the implementation of the boundary conditions, and a detailed description of the adaptive refinement method. In chapter four, stationary and pitching wing flow solutions will be discussed and interpreted. Ultimately, some conclusions will be drawn and some recommendations for further work will be made.

Chapter 2

Governing Equations

> Fluid dynamics is much less interesting if it is treated largely as an exercise in mathematics.
>
> From the point of view of a 'pure' scientist concerned only with basic laws, there seems to be little need to go further.
>
> The set of governing equations is much too complicated for a direct mathematical approach to be feasible.
>
> G. K. Batchelor

In this chapter, the governing equations for inviscid, compressible flow in an inertial reference frame are derived, and appropriate choices for nondimensionalization and boundary conditions are described. In addition, the equations for the flow are transformed into a non-inertial reference frame, which is specialized to rotation about a fixed center.

2.1 Inertial Frame of Reference

The Euler equations are a system of partial differential equations that describe the behavior of an compressible, inviscid, non-conducting fluid. They are derived from the integral form of the laws of conservation of mass, momentum, and energy, in an inertial frame of reference.

For an arbitrary fixed control volume V, the law of conservation of mass can be expressed as

$$\frac{\partial}{\partial t}\int_V \rho \, dV = -\int_{\partial V} \rho \, (u_j n_j) \, dS \tag{2.1}$$

where ρ is the density, u_j is the fluid velocity, expressed using indicial notation, and n_j is the outward-pointing unit normal vector at the surface of the control volume. This states that the rate of change of the mass of the fluid in the control volume is equal to the transport of mass across the control volume boundary, ∂V. Gauss' divergence theorem is used to transform the surface integral into a volume integral over V. Then, by requiring the resulting integral equation to hold for any infinitesimal control volume, the differential form of the law of mass conservation is found to be

$$\frac{\partial \rho}{\partial t} + \frac{\partial}{\partial x_j}(\rho u_j) = 0 \tag{2.2}$$

which holds everywhere that the flow quantities are continuous and differentiable. At discontinuities, only the integral form is valid.

The integral form of the law of conservation of momentum can be written as

$$\frac{\partial}{\partial t}\int_V \rho u_i \, dV = -\int_{\partial V} \rho u_i \, (u_j n_j) \, dS - \int_{\partial V} p \, n_i \, dS \tag{2.3}$$

where p is the static pressure of the fluid. The index i spans the three equations, and the repeated index j indicates summation. These equations state that the momentum of the fluid within the control volume is changed by the transport of momentum across the surface, and by the action of fluid pressure on the surface ∂V. Again, the divergence theorem is used to transform the surface integral terms. The differential form of the momentum equation,

$$\frac{\partial}{\partial t}(\rho u_i) + \frac{\partial}{\partial x_j}(\rho u_i u_j + p) = 0 \tag{2.4}$$

results. Again, the differential form is not valid at flow discontinuities.

The integral form of the law of conservation of energy can be written as

$$\frac{\partial}{\partial t}\int_V \rho E \, dV = -\int_{\partial V} \rho E \, (u_j n_j) \, dS - \int_{\partial V} u_j \, (p \, n_j) \, dS \tag{2.5}$$

where E is the total internal energy per unit mass. This states that the energy within the control volume is changed by the transport of energy across the surface, and by the work done by the action of the fluid pressure upon the surface of V. By application of the divergence theorem, the energy equation can be transformed into its differential form,

$$\frac{\partial}{\partial t}(\rho E) + \frac{\partial}{\partial x_j}([\rho E + p] \, u_j) = 0 \tag{2.6}$$

which is only valid in continuous regions of the flow.

Since the three conservation laws have analogous terms, they can be grouped together to form a system of equations,

$$\frac{\partial U}{\partial t} + \frac{\partial F}{\partial x} + \frac{\partial G}{\partial y} + \frac{\partial H}{\partial z} = 0 \tag{2.7}$$

where the state vector U is

$$U = \begin{bmatrix} \rho \\ \rho u \\ \rho v \\ \rho w \\ \rho E \end{bmatrix} \tag{2.8}$$

and the Cartesian components of the flux vector, F, G and H are

$$F = \begin{bmatrix} \rho u \\ \rho u^2 + p \\ \rho uv \\ \rho uw \\ \rho uh \end{bmatrix} \quad G = \begin{bmatrix} \rho v \\ \rho uv \\ \rho v^2 + p \\ \rho vw \\ \rho vh \end{bmatrix} \quad H = \begin{bmatrix} \rho w \\ \rho uw \\ \rho vw \\ \rho w^2 + p \\ \rho wh \end{bmatrix}. \tag{2.9}$$

The momentum equation is written as the three equations for its Cartesian compo-

nents, u, v and w. The quantity h is the total enthalpy, defined to be

$$h = E + \frac{p}{\rho}. \tag{2.10}$$

The system is closed by the equation of state for a perfect gas,

$$p = (\gamma - 1)\,\rho e, \tag{2.11}$$

where e is the internal energy per unit mass, which is defined by the thermodynamic relation

$$E = e + \tfrac{1}{2}(u^2 + v^2 + w^2), \tag{2.12}$$

and γ is the ratio of specific heats, c_p/c_v.

2.2 Rotating Frame of Reference

To express the Euler equations in a moving, non-inertial frame of reference, in which derivatives are denoted by a prime superscript, substitute the following transformations for the derivatives of an arbitrary scalar and an arbitrary vector into the Euler equations:

$$\frac{DQ}{Dt} = \frac{D'Q}{Dt'} \qquad \frac{D\vec{Q}}{Dt} = \frac{D'\vec{Q}}{Dt'} + \vec{\omega}\times\vec{Q} \tag{2.13}$$

or, expanding the total derivatives:

$$\frac{\partial Q}{\partial t} = \frac{\partial' Q}{\partial t'} - \vec{v}_t\cdot\nabla Q \qquad \frac{\partial \vec{Q}}{\partial t} = \frac{\partial' \vec{Q}}{\partial t'} - \vec{v}_t\cdot\nabla\vec{Q} + \vec{\omega}\times\vec{Q} \tag{2.14}$$

where

$$\vec{v}_t = \vec{v}_a - \vec{v}_r = \vec{v}_0 + \vec{\omega}\times\vec{r} \tag{2.15}$$

is the transformation velocity from the absolute frame of motion, in which the fluid velocity is $\vec{v}_a$, to the moving, relative frame, in which the fluid velocity is $\vec{v}_r$. The

relative motion can have both a translational velocity, $\vec{v}_0$, and a rotational velocity about a fixed point, from which the position vector $\vec{r}$ is referenced. The rotation need not be steady. When the transformations 2.14 are substituted into the Euler equations (2.7, 2.8, 2.9), the system gains a source term, S, which contains terms related to the motion of the frame:

$$\frac{\partial' U}{\partial t'} + \frac{\partial F}{\partial x} + \frac{\partial G}{\partial y} + \frac{\partial H}{\partial z} = S. \tag{2.16}$$

Also, several of the primitive variables have changed meaning, so that the state vector is now

$$U = \begin{bmatrix} \rho \\ \rho u_r \\ \rho v_r \\ \rho w_r \\ \rho E_r \end{bmatrix} \tag{2.17}$$

and the flux vector is

$$F = \begin{bmatrix} \rho u_r \\ \rho u_r^2 + p \\ \rho u_r v_r \\ \rho u_r w_r \\ \rho u_r h_r \end{bmatrix}, \; G = \begin{bmatrix} \rho v_r \\ \rho u_r v_r \\ \rho v_r^2 + p \\ \rho v_r w_r \\ \rho v_r h_r \end{bmatrix}, \; H = \begin{bmatrix} \rho w_r \\ \rho u_r w_r \\ \rho v_r w_r \\ \rho w_r^2 + p \\ \rho w_r h_r \end{bmatrix}. \tag{2.18}$$

This is the same form of the unsteady Euler equations as used by Kandil and Chuang [35, 34]. The fluid velocities are now measured in the relative frame of reference, and the total energy and enthalpy are replaced with new quantities, which are related to the quantities of the absolute frame by

$$E_r = E - \vec{v}_a \cdot \vec{v}_t \tag{2.19}$$

$$h_r = h - \vec{v}_a \cdot \vec{v}_t. \tag{2.20}$$

The quantity h_r is called the total rothalpy, and is constant in steady flows in a rotating reference frame, as is the total enthalpy in a nonrotating frame. The source term S has

the complicated form

$$S = \begin{bmatrix} 0 \\ -\rho a_{tx} \\ -\rho a_{ty} \\ -\rho a_{tz} \\ -\rho \left\{ \vec{v}_a \cdot (\vec{a}_0 + \dot{\vec{\omega}} \times \vec{r}) + \vec{v}_0 \cdot (\vec{\omega} \times \vec{v}_a) \right\} \end{bmatrix} \tag{2.21}$$

where

$$\vec{a}_t = \frac{D\vec{v}_a}{Dt} - \frac{D'\vec{v}_r}{Dt'} \tag{2.22}$$

$$= \vec{a}_0 + \dot{\vec{\omega}} \times \vec{r} + 2\vec{\omega} \times \vec{v}_r + \vec{\omega} \times (\vec{\omega} \times \vec{r}) \tag{2.23}$$

is the relative acceleration of the two frames, having linear, angular, Coriolis, and centripetal terms, respectively.

The cumbersome form of the energy source term is reduced by restricting the form of the transformation velocity. In this case, the motion is required to be purely rotational, so that the translational terms, $\vec{v}_0$ and $\vec{a}_0$, vanish, giving a source term with the form

$$S = \begin{bmatrix} 0 \\ -\rho a_{tx} \\ -\rho a_{ty} \\ -\rho a_{tz} \\ -\rho \left\{ (\vec{v}_r + \vec{\omega} \times \vec{r}) \cdot (\dot{\vec{\omega}} \times \vec{r}) \right\} \end{bmatrix}. \tag{2.24}$$

In the case of pitching motion, the axis of rotation points in the spanwise direction, and

the angular velocity ω is equal to the pitch rate, $\dot{\alpha}$. The source term now can be written

$$S = \begin{bmatrix} 0 \\ -\rho(\dot{\omega}z + 2\omega w_r - \omega^2 x) \\ 0 \\ -\rho(-\dot{\omega}x - 2\omega u_r - \omega^2 z) \\ -\rho\dot{\omega}\left\{(u_r z - w_r x) + \omega(x^2 + z^2)\right\} \end{bmatrix} \tag{2.25}$$

where x and z are measured from the center of rotation. In addition, the variation of the angle of attack, and thus the rotation rate ω, is taken to vary sinusoidally with an angular frequency of Ω. Specifically, the angle of attack varies as

$$\alpha = \alpha_0 + \tfrac{1}{2}\Delta\alpha(1 - \cos\Omega t) \tag{2.26}$$

The rotation rate is then

$$\omega = \tfrac{1}{2}\Omega\Delta\alpha \sin\Omega t, \tag{2.27}$$

which has a maximum value of

$$\omega_{\max} = \tfrac{1}{2}\Delta\alpha\Omega. \tag{2.28}$$

In addition, the angular acceleration is

$$\dot{\omega} = \tfrac{1}{2}\Omega^2\Delta\alpha \cos\Omega t. \tag{2.29}$$

The energy source term in equations 2.24 and 2.25 vanish if the rotation is steady, as occurs in most turbomachinery and rotorcraft flows. However, the Coriolis and centripetal contributions to the momentum source terms remain.

2.3 Physical Boundary Conditions

There are three different physical boundary conditions to apply to the Euler equations. The implementation of these boundary conditions is discussed in section 3.3.

2.3.1 Solid wall

At a solid wall, no flux is permitted through the surface. This condition is written as

$$\vec{u} \cdot \vec{n} = 0 \tag{2.30}$$

where $\vec{n}$ is the unit vector normal to the surface. This condition also applies at symmetry surfaces.

2.3.2 Kutta condition

Since there is a multitude of solutions for the flow around an arbitrary body, some condition must be imposed to collapse to a single solution. For the flows that will be considered in this thesis, the Kutta condition can be applied at sharp edges of the wing to fix the lift. For sharp-edged delta wings, both the leading and trailing edges are treated this way.

2.3.3 Far field

In the far field, the flow should approach a uniform free stream in the inertial reference frame. By use of equation 2.15, this is transformed in the rotating frame into a free stream with time-varying solid body rotation imposed. Since it is impossible to model variations at infinity using the numerical methods described in this thesis, the implementation of this boundary condition will be the most mathematically complex.

2.4 Nondimensionalization

It is often desirable to make the Euler equations dimensionless to solve them numerically. This makes the problem independent of the choice of units, clarifies the scales relevant to the problem, and can reduce the sensitivity of the solution procedure to numerical round-off errors. The reference parameters used are the freestream density, ρ_∞, the freestream speed of sound, a_∞, and a characteristic length. In this thesis, the wing root chord, c_R, is chosen as a length scale. The nondimensionalization factors for some flow quantities are listed in table 2.1. There are three important nondimensional parameters, which appear in table 2.2. The freestream Mach number, M_∞, measures the importance of compressibility, while both the reduced frequency, k, and the nondimensional pitch rate, $\mathcal{K}$, both measure the importance of unsteady effects. The reduced frequency measures the frequency of unsteady effects, and the nondimensional pitch rate measures the amplitude of unsteady effects. The latter two parameters are related by

$$k = \frac{2\mathcal{K}}{\Delta\alpha} \tag{2.31}$$

where $\Delta\alpha$ is the range of angle of attack variation during the unsteady cycle. The flows in this thesis have a low Mach number in the subsonic range. A flow with a low reduced frequency is referred to as quasi-steady, meaning that the evolution of the flow with time is a succession of steady flows, with varying parameters.

The form of the Euler equations is unchanged by this nondimensionalization, but the free stream boundary conditions are altered. With this set of reference parameters, the freestream state vector takes the form

$$\begin{bmatrix} \rho \\ \rho u \\ \rho v \\ \rho w \\ \rho E \end{bmatrix} = \begin{bmatrix} 1 \\ M_\infty \cos\alpha\cos\beta - \omega z \\ M_\infty \sin\beta \\ M_\infty \sin\alpha\cos\beta + \omega x \\ \frac{1}{\gamma(\gamma-1)} + \frac{1}{2}M_\infty^2 \end{bmatrix} \tag{2.32}$$

Quantity	Reference	Freestream Value
ρ	ρ_∞	1
u, v, w, a	a_∞	$M_\infty \cos\alpha \cos\beta - \omega z$, $M_\infty \sin\beta$, $M_\infty \sin\alpha \cos\beta + \omega x$, 1
E, h	a_∞^2	$\frac{1}{2}M_\infty^2 + \frac{1}{\gamma(\gamma-1)}$, $\frac{1}{2}M_\infty^2 + \frac{1}{\gamma-1}$
p	ρa_∞^2	$1/\gamma$
x, y, z	c_R	—
t	c_R/a_∞	—
ω, Ω	a_∞/c_R	—, $2M_\infty k$
N, L, D	$\rho_\infty a_\infty^2 c_R^2$	—
M	$\rho_\infty a_\infty^2 c_R^3$	—

Table 2.1: Nondimensionalization of flow quantities

Parameter	Symbol	Definition
freestream Mach number	M_∞	$\frac{q_\infty}{a_\infty}$
reduced frequency	k	$\frac{\Omega c_R}{2q_\infty}$
nondimensional pitch rate	$\mathcal{K}$	$\frac{\omega_{\max} c_R}{2q_\infty}$

Table 2.2: Nondimensional parameters

Coefficient	Symbol	Dimensional	Nondimensional
normal force	C_N	$\frac{N}{\frac{1}{2}\rho_\infty q_\infty^2 S}$	$\frac{N^*}{\frac{1}{8}M_\infty^2 AR}$
lift	C_L	$\frac{L}{\frac{1}{2}\rho_\infty q_\infty^2 S}$	$\frac{L^*}{\frac{1}{8}M_\infty^2 AR}$
drag	C_D	$\frac{D}{\frac{1}{2}\rho_\infty q_\infty^2 S}$	$\frac{D^*}{\frac{1}{8}M_\infty^2 AR}$
pitching moment	C_M	$\frac{M}{\frac{1}{2}\rho_\infty q_\infty^2 S\bar{c}}$	$\frac{M^*}{\frac{1}{12}M_\infty^2 AR}$

Table 2.3: Nondimensional aerodynamic coefficients

in which M_∞ is the freestream Mach number, α and β are the angles of attack and yaw, respectively, and ω is the rotation rate.

The forces that act on a wing are characterized by the dimensionless aerodynamic coefficients of normal force, lift, drag and pitching moment. The definitions of these coefficients, in terms of both dimensional and dimensionless quantities, are given in table 2.3. The forces are normalized by the freestream dynamic pressure and the wing area. The pitching moment has an additional normalization factor, $\bar{c}$, the mean aerodynamic chord of the wing. For a triangular wing, this has the value of two-thirds of the wing root chord. In addition, these formulae assume that the forces are due to the effect of the entire wing. When simulating flows about a wing at zero angle of yaw, one can take advantage of the symmetrical nature of the problem to compute a solution within a domain of half the size. In such a case, the aerodynamic force coefficients must be doubled to obtain their values for the entire wing.

2.5 Auxiliary Quantities

The following is a list of auxiliary quantities, defined in terms of the primitive variables:

Quantity	Definition	Freestream
Local flow speed:	$q = \sqrt{u^2 + v^2 + w^2}$	M_∞
Local speed of sound:	$a = \sqrt{\frac{\gamma p}{\rho}}$	1
Local Mach number:	$M = \frac{q}{a}$	M_∞
Total pressure:	$p_0 = p\left(1 + \frac{\gamma - 1}{2} M^2\right)^{\frac{\gamma}{\gamma - 1}}$	$\frac{1}{\gamma}\left(1 + \frac{\gamma - 1}{2} M_\infty^2\right)^{\frac{\gamma}{\gamma - 1}}$
Total pressure loss:	$\Delta p_0 = 1 - \frac{p_0}{p_{0\infty}}$	0
Entropy:	$s = \log \frac{\gamma p}{\rho^\gamma}$	0

Chapter 3

Numerical solution procedure

God made integers, all else is the work of man.

Leopold Kronecker
Jahresberichte der Deutschen Mathematicker Vereinigung, bk. 2

In this chapter, the numerical solution method for solving the governing equations is derived. The procedure used is a finite element method based on a mesh of tetrahedral cells. Also, the temporal integration procedure is discussed, along with the implementation of the physical boundary conditions and the numerical smoothing procedure. The chapter also includes a description of the adaptive refinement procedure.

3.1 Mesh geometry

The tetrahedral cell is the basis for most of the calculations described here. The faces and nodes of a cell are numbered such that node j is opposite face j. Thus each face is defined by the three nodes with different numbers. The outward-pointing area normal $\vec{S}$ of each cell face is frequently used. It is constructed by taking the cross product of any two edge vectors of the face, with the requirement that it point outwards. Thus,

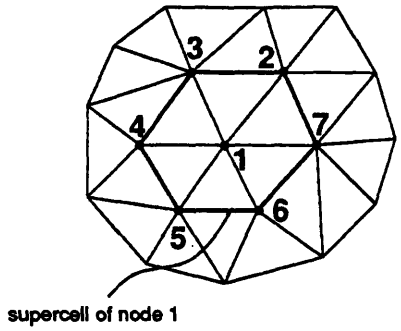

Figure 3.1: Section of a triangular mesh

$$\vec{S}_1 = \tfrac{1}{2}(\vec{x}_{32} \times \vec{x}_{42}) \quad \begin{cases} S_{x1} &= \tfrac{1}{2}(y_{32}z_{42} - z_{32}y_{42}) \\ S_{y1} &= \tfrac{1}{2}(z_{32}x_{42} - x_{32}z_{42}) \\ S_{z1} &= \tfrac{1}{2}(x_{32}y_{42} - y_{32}x_{42}) \end{cases} \tag{3.1}$$

$$\vec{S}_2 = \tfrac{1}{2}(\vec{x}_{41} \times \vec{x}_{31}) \quad \begin{cases} S_{x2} &= \tfrac{1}{2}(y_{41}z_{31} - z_{41}y_{31}) \\ S_{y2} &= \tfrac{1}{2}(z_{41}x_{31} - x_{41}z_{31}) \\ S_{z2} &= \tfrac{1}{2}(x_{41}y_{31} - y_{41}x_{31}) \end{cases} \tag{3.2}$$

$$\vec{S}_3 = \tfrac{1}{2}(\vec{x}_{21} \times \vec{x}_{41}) \quad \begin{cases} S_{x3} &= \tfrac{1}{2}(y_{21}z_{41} - z_{21}y_{41}) \\ S_{y3} &= \tfrac{1}{2}(z_{21}x_{41} - x_{21}z_{41}) \\ S_{z3} &= \tfrac{1}{2}(x_{21}y_{41} - y_{21}x_{41}) \end{cases} \tag{3.3}$$

$$\vec{S}_4 = \tfrac{1}{2}(\vec{x}_{31} \times \vec{x}_{21}) \quad \begin{cases} S_{x4} &= \tfrac{1}{2}(y_{31}z_{21} - z_{31}y_{21}) \\ S_{y4} &= \tfrac{1}{2}(z_{31}x_{21} - x_{31}z_{21}) \\ S_{z4} &= \tfrac{1}{2}(x_{31}y_{21} - y_{31}x_{21}) \end{cases} \tag{3.4}$$

where $x_{ij} = x_i - x_j$, $y_{ij} = y_i - y_j$ and $z_{ij} = z_i - z_j$. Although it is far from obvious based on the above formulas, the vector sum of the areas of the four faces of a tetrahedron is zero. This is a general result for a closed surface.

The union of all cells that contain a node is called the *supercell* of that node, as represented for the analogous two-dimensional situation in Figure 3.1. The volume of the supercell of node i is the sum of the volumes of the cells of which node i is a vertex.

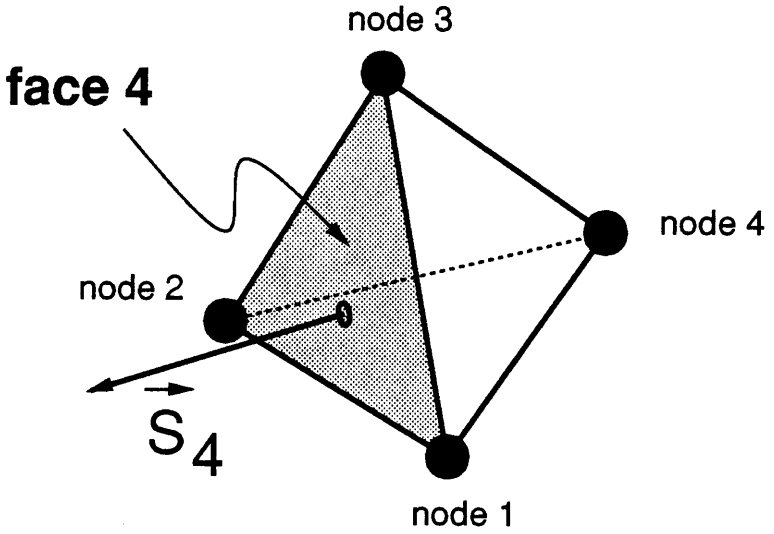

Figure 3.2: Tetrahedral cell nomenclature

The volume of a tetrahedral cell is

$$V^C = \frac{1}{6}\begin{vmatrix} x_{21} & y_{21} & z_{21} \\ x_{31} & y_{31} & z_{31} \\ x_{41} & y_{41} & z_{41} \end{vmatrix} \tag{3.5}$$

$$= \frac{1}{6}\left(x_{21}y_{31}z_{41} + y_{21}z_{31}x_{41} + z_{21}x_{31}y_{41} - z_{21}y_{31}x_{41} - x_{21}z_{31}y_{41} - y_{21}x_{31}z_{41}\right) \tag{3.6}$$

where

$$\vec{x}_{ij} = \vec{x}_i - \vec{x}_j \tag{3.7}$$

is the edge vector between the ith and jth nodes of the tetrahedron. The vertices of the cell are numbered so that nodes 1, 2 and 3 are in a counterclockwise orientation when viewed from node 4. A single tetrahedral cell is seen in figure 3.2, showing the node and face numbering, and a typical face area vector.

The boundaries of the mesh are arranged so that the nodes are numbered in the counterclockwise direction when viewed from the interior of the computational domain. The surface normal at a boundary node is the area-weighted average of the normals of

the boundary faces that contain the node. The boundary normal is the cross product of two edge vectors that yield the correct direction. Thus,

$$\begin{aligned} \vec{S}^F &= \tfrac{1}{2}(\vec{x}_{21} \times \vec{x}_{31}) = \tfrac{1}{2}(\vec{x}_{32} \times \vec{x}_{12}) = \tfrac{1}{2}(\vec{x}_{13} \times \vec{x}_{23}) \\ S_x^F &= \tfrac{1}{2}(y_{21}z_{31} - z_{21}y_{31}) \\ S_y^F &= \tfrac{1}{2}(z_{21}x_{31} - x_{21}z_{31}) \\ S_z^F &= \tfrac{1}{2}(x_{21}y_{31} - y_{21}x_{31}) \end{aligned} \tag{3.8}$$

All boundary normals point into the computational domain.

3.1.1 Mesh Generation

Tetrahedral meshes are generated by the advancing wavefront method, using a mesh generator developed by Peraire, *et al.* [59, 61]. A three-dimensional mesh is generated in two steps. First, a surface mesh, composed of triangular elements, is generated. Then, using the surface mesh as an input, a volume mesh, composed of tetrahedra, is generated in the flow field. Mesh generation begins with the assembly of a front of triangles, which is initialized to be the surface mesh. Then, every triangle is examined, and a tetrahedron is created with the triangle as a base, and having a height calculated according to a mesh point spacing function, which is controlled by the user. The node at the peak of the tetrahedron will be an existing node of the mesh if a suitable node exists, or, if not, it is created. The original triangle is then removed from the front. The procedure continues until the front does not contain any triangles.

3.2 Finite element method

Spatial discretization is by means of the Galerkin finite element method with tetrahedral cells. The mass matrix is lumped, resulting in a scheme identical to the cell-vertex finite volume method in which control volume for node i is the supercell of the node.

However, the finite element and finite volume methods lead to different discretizations when viscous effects are modeled. A detailed discussion of the finite element method can be found in Cook [12], although with an emphasis on applications to structural mechanics.

The basis of the finite element method is that the spatial variation of the state and flux variables is represented in terms of nodal values of these quantities, $U_i(t)$, $F_i(t)$, $G_i(t)$, $H_i(t)$ and $S_i(t)$, and interpolation functions $N_i(x, y, z)$, so that

$$\begin{aligned} U(x,y,z,t) &= N_i(x,y,z)\, U_i(t) \\ F(x,y,z,t) &= N_i(x,y,z)\, F_i(t) \\ G(x,y,z,t) &= N_i(x,y,z)\, G_i(t) \\ H(x,y,z,t) &= N_i(x,y,z)\, H_i(t) \\ S(x,y,z,t) &= N_i(x,y,z)\, S_i(t) \end{aligned} \tag{3.9}$$

in which the repeated index i indicates a sum over the nodes of the mesh. The interpolation functions N_i have a value of unity at the node i, and a value of zero at all other nodes. The sum of all the interpolation functions must be unity, so that a uniform field results when all the nodal quantities are equal. A distinction of the finite element method, as opposed to other interpolation methods, is that the global interpolation functions are a piecewise combination of local interpolation functions, one per cell. This means that the variation of a quantity inside a cell is a function only of the nodal quantities and interpolation functions associated with the nodes of that cell. The local interpolation functions are taken to be zero outside the cell. The superscript C is used to represent a quantity associated with a cell.

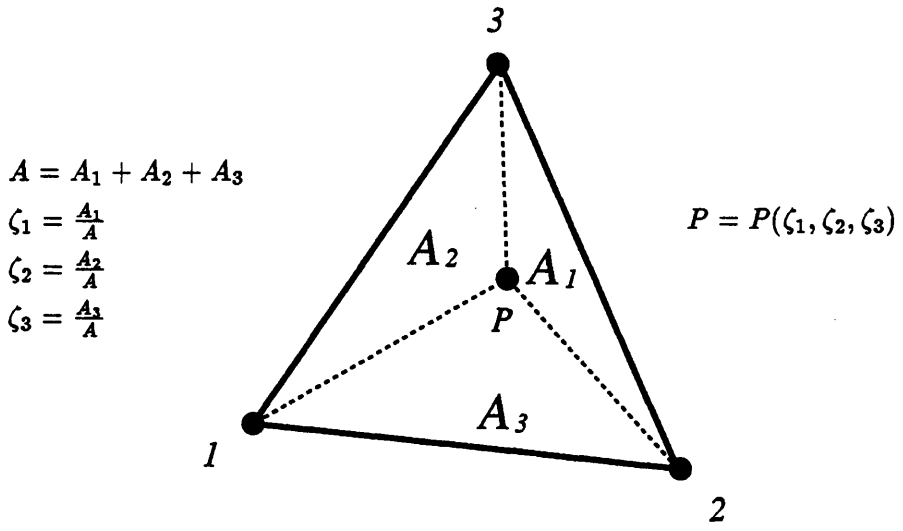

Figure 3.3: Triangular area coordinates

3.2.1 Interpolation functions

The local interpolation functions used here are trilinear. They are defined in terms of a local coordinate system, which is the set of tetrahedral volume coordinates ζ_1, ζ_2, ζ_3 and ζ_4, which are shown for the analogous two-dimensional situation in Figure 3.3. An arbitrary point P divides the tetrahedron into four sub-tetrahedra. The volume coordinates are defined as ratios of the volumes of the sub-tetrahedra to the volume of the entire tetrahedron:

$$\zeta_1 = \frac{V_1}{V^C},\ \zeta_2 = \frac{V_2}{V^C},\ \zeta_3 = \frac{V_3}{V^C},\ \zeta_4 = \frac{V_4}{V^C}. \tag{3.10}$$

Since $V^C = V_1 + V_2 + V_3 + V_4$ these coordinates are not independent, but satisfy the relation

$$\zeta_1 + \zeta_2 + \zeta_3 + \zeta_4 = 1. \tag{3.11}$$

Therefore ζ_4 is replaced by $1 - \zeta_1 - \zeta_2 - \zeta_3$. The volume coordinates each have a value of unity at the node with which they are associated, and a value of zero at the other three nodes of the tetrahedron. Since these are the properties desired in a set of interpolation functions, the interpolation functions are taken to be exactly the volume coordinates,

so that

$$\begin{aligned} N_1^C &= \zeta_1 \\ N_2^C &= \zeta_2 \\ N_3^C &= \zeta_3 \\ N_4^C &= \zeta_4 = 1 - \zeta_1 - \zeta_2 - \zeta_3. \end{aligned} \tag{3.12}$$

The local coordinates are often referred to as *natural coordinates.*

3.2.2 Spatial Discretization

The discretization of the Euler equations proceeds as follows. First, the interpolated representations of the state, source and flux quantities (Eqn. 3.9) are substituted into the Euler equations, giving

$$N_i \frac{dU_i}{dt} = N_i S_i - \frac{\partial N_i}{\partial x} F_i - \frac{\partial N_i}{\partial y} G_i - \frac{\partial N_i}{\partial z} H_i \tag{3.13}$$

in which indicial notation is again used. Note that this is a *single* vector equation, not a system of equations. The interpolation imposes a form on the solution that is unlikely to satisfy the Euler equations at every point in the field. Therefore it is necessary to recast the equations in the weak form by projecting them onto the space of *test functions* $\tilde{N}_j$ and integrating over the solution domain. The test functions, which are again associated with the mesh nodes, roughly correspond to control volumes over which the integral equations are satisfied. In the Galerkin approach, the test functions are identical to the interpolation functions for the same node. We now have a set of equations

$$\frac{dU_i}{dt} \int N_i N_j \, dV = S_i \int N_i N_j \, dV - F_i \int \frac{\partial N_i}{\partial x} N_j \, dV - G_i \int \frac{\partial N_i}{\partial y} N_j \, dV - H_i \int \frac{\partial N_i}{\partial z} N_j \, dV \tag{3.14}$$

in which the repeated index i indicates summation over the set of nodes, while the non-repeated index j spans the set of equations. Equations 3.14 can be written as

$$M_{ij}\frac{dU_i}{dt} = M_{ij}S_i - R_{X,ij}F_i - R_{Y,ij}G_i - R_{Z,ij}H_i \tag{3.15}$$

in which M_{ij} is the consistent mass matrix, and $R_{X,ij}$, $R_{Y,ij}$ and $R_{Z,ij}$ are the residual matrices. These matrices are defined by integration over the entire domain. However, since the interpolation and test functions are defined piecewise with regard to the cells, these integrals can be broken up into a sum of integrals over the individual cells, so that

$$M_{ij}^C = \int_{V^C} N_i N_j \, dV \tag{3.16}$$

$$R_{X,ij}^C = \int_{V^C} \frac{\partial N_i}{\partial x} N_j \, dV \tag{3.17}$$

$$R_{Y,ij}^C = \int_{V^C} \frac{\partial N_i}{\partial y} N_j \, dV \tag{3.18}$$

$$R_{Z,ij}^C = \int_{V^C} \frac{\partial N_i}{\partial z} N_j \, dV. \tag{3.19}$$

It is now possible to write equation 3.15 as

$$\left(\sum_{\text{cells}} M_{ij}^C\right)\frac{dU_i}{dt} = \left(\sum_{\text{cells}} M_{ij}^C\right)S_i - \left(\sum_{\text{cells}} R_{X,ij}^C\right)F_i - \left(\sum_{\text{cells}} R_{Y,ij}^C\right)G_i - \left(\sum_{\text{cells}} R_{Z,ij}^C\right)H_i. \tag{3.20}$$

The range of summation is the group of cells that contain node i, which form the supercell of the node.

3.2.3 Calculation of Matrices

Integration of Equations 3.16 through 3.19 is carried out in the local coordinate system $(\zeta_1, \zeta_2, \zeta_3)$. The spatial derivatives of the interpolation functions are evaluated by the chain rule, as

$$\frac{\partial N_i}{\partial x} = \frac{\partial N_i}{\partial \zeta_1}\frac{\partial \zeta_1}{\partial x} + \frac{\partial N_i}{\partial \zeta_2}\frac{\partial \zeta_2}{\partial x} + \frac{\partial N_i}{\partial \zeta_3}\frac{\partial \zeta_3}{\partial x}$$

$$\begin{aligned}\frac{\partial N_i}{\partial y} &= \frac{\partial N_i}{\partial \zeta_1}\frac{\partial \zeta_1}{\partial y} + \frac{\partial N_i}{\partial \zeta_2}\frac{\partial \zeta_2}{\partial y} + \frac{\partial N_i}{\partial \zeta_3}\frac{\partial \zeta_3}{\partial y} \\ \frac{\partial N_i}{\partial z} &= \frac{\partial N_i}{\partial \zeta_1}\frac{\partial \zeta_1}{\partial z} + \frac{\partial N_i}{\partial \zeta_2}\frac{\partial \zeta_2}{\partial z} + \frac{\partial N_i}{\partial \zeta_3}\frac{\partial \zeta_3}{\partial z}.\end{aligned} \tag{3.21}$$

This is particularly convenient since

$$\begin{aligned}\partial N_1/\partial \zeta_1 = 1 \quad \partial N_1/\partial \zeta_2 = 0 \quad \partial N_1/\partial \zeta_3 = 0 \\ \partial N_2/\partial \zeta_1 = 0 \quad \partial N_2/\partial \zeta_2 = 1 \quad \partial N_1/\partial \zeta_3 = 0 \\ \partial N_3/\partial \zeta_1 = 0 \quad \partial N_3/\partial \zeta_2 = 0 \quad \partial N_3/\partial \zeta_3 = 1 \\ \partial N_4/\partial \zeta_1 = -1 \quad \partial N_4/\partial \zeta_2 = -1 \quad \partial N_4/\partial \zeta_3 = -1.\end{aligned} \tag{3.22}$$

Combining equations 3.21 and 3.22 yields

$$\begin{array}{lll} \frac{\partial N_1}{\partial x} = \frac{\partial \zeta_1}{\partial x} & \frac{\partial N_1}{\partial y} = \frac{\partial \zeta_1}{\partial y} & \frac{\partial N_1}{\partial z} = \frac{\partial \zeta_1}{\partial z} \\ \frac{\partial N_2}{\partial x} = \frac{\partial \zeta_2}{\partial x} & \frac{\partial N_2}{\partial y} = \frac{\partial \zeta_2}{\partial y} & \frac{\partial N_2}{\partial z} = \frac{\partial \zeta_2}{\partial z} \\ \frac{\partial N_3}{\partial x} = \frac{\partial \zeta_3}{\partial x} & \frac{\partial N_3}{\partial y} = \frac{\partial \zeta_3}{\partial y} & \frac{\partial N_3}{\partial z} = \frac{\partial \zeta_3}{\partial z} \\ \frac{\partial N_4}{\partial x} = -\frac{\partial \zeta_1}{\partial x} - \frac{\partial \zeta_2}{\partial x} - \frac{\partial \zeta_3}{\partial x} & \frac{\partial N_4}{\partial y} = -\frac{\partial \zeta_1}{\partial y} - \frac{\partial \zeta_2}{\partial y} - \frac{\partial \zeta_3}{\partial y} & \frac{\partial N_4}{\partial z} = -\frac{\partial \zeta_1}{\partial z} - \frac{\partial \zeta_2}{\partial z} - \frac{\partial \zeta_3}{\partial z}. \end{array} \tag{3.23}$$

To evaluate the spatial derivatives of the volume coordinates in equations 3.23, the spatial coordinates x, y and z are represented via interpolation between the nodes, in the same manner as are the state quantities, so that

$$\begin{aligned} x^C(\zeta_1,\zeta_2,\zeta_3) &= x_i N_i^C(\zeta_1,\zeta_2,\zeta_3) \\ &= x_1\zeta_1 + x_2\zeta_2 + x_3\zeta_3 + x_4(1-\zeta_1-\zeta_2-\zeta_3) \\ &= (x_1-x_4)\zeta_1 + (x_2-x_4)\zeta_2 + (x_3-x_4)\zeta_3 + x_4 \end{aligned} \tag{3.24}$$

$$\begin{aligned} y^C(\zeta_1,\zeta_2,\zeta_3) &= y_i N_i^C(\zeta_1,\zeta_2,\zeta_3) \\ &= y_1\zeta_1 + y_2\zeta_2 + y_3\zeta_3 + y_4(1-\zeta_1-\zeta_2-\zeta_3) \\ &= (y_1-y_4)\zeta_1 + (y_2-y_4)\zeta_2 + (y_3-y_4)\zeta_3 + y_4 \end{aligned} \tag{3.25}$$

$$\begin{aligned} z^C(\zeta_1,\zeta_2,\zeta_3) &= z_i N_i^C(\zeta_1,\zeta_2,\zeta_3) \\ &= z_1\zeta_1 + z_2\zeta_2 + z_3\zeta_3 + z_4(1-\zeta_1-\zeta_2-\zeta_3) \\ &= (z_1-z_4)\zeta_1 + (z_2-z_4)\zeta_2 + (z_3-z_4)\zeta_3 + z_4. \end{aligned} \tag{3.26}$$

From Equations 3.24 – 3.26, the Jacobian matrix of the transformation is found to be

$$\begin{aligned} J &= \frac{\partial(x,y,z)}{\partial(\zeta_1,\zeta_2,\zeta_3)} \\ &= \begin{bmatrix} x_{14} & x_{24} & x_{34} \\ y_{14} & y_{24} & y_{34} \\ z_{14} & z_{24} & z_{34} \end{bmatrix} \end{aligned} \tag{3.27}$$

where $\vec{x}_{ij} = \vec{x}_i - \vec{x}_j$ is the edge vector between the ith and jth nodes of the tetrahedron. Inverting the Jacobian matrix yields

$$\begin{aligned} J^{-1} &= \frac{\partial(\zeta_1,\zeta_2,\zeta_3)}{\partial(x,y,z)} \\ &= \frac{1}{|J|}\begin{bmatrix} y_{24}z_{34} - z_{24}y_{34} & z_{24}x_{34} - x_{24}z_{34} & x_{24}y_{34} - y_{24}x_{34} \\ z_{14}y_{34} - y_{14}z_{34} & x_{14}z_{34} - z_{14}x_{34} & y_{14}x_{34} - x_{14}y_{34} \\ y_{14}z_{24} - z_{14}y_{24} & z_{14}x_{24} - x_{14}z_{24} & x_{14}y_{24} - y_{14}x_{24} \end{bmatrix} \\ &= -\frac{1}{3V^C}\begin{bmatrix} S_{x1} & S_{y1} & S_{z_1} \\ S_{x2} & S_{y2} & S_{z2} \\ S_{x3} & S_{y3} & S_{z3} \end{bmatrix} \end{aligned} \tag{3.28}$$

in which V^C is the volume of the cell, and $S_{x,j}$, $S_{y,j}$ and $S_{z,j}$ are the Cartesian components of the area vector of the jth face of the cell. Finally, we obtain the spatial derivatives of the interpolation functions by substituting the elements of J^{-1} into Equation 3.23, producing

$$\begin{array}{lll} \frac{\partial N_1}{\partial x} = -\frac{S_{x1}}{3V^C} & \frac{\partial N_1}{\partial y} = -\frac{S_{y1}}{3V^C} & \frac{\partial N_1}{\partial z} = -\frac{S_{z1}}{3V^C} \\ \frac{\partial N_2}{\partial x} = -\frac{S_{x2}}{3V^C} & \frac{\partial N_2}{\partial y} = -\frac{S_{y2}}{3V^C} & \frac{\partial N_2}{\partial z} = -\frac{S_{z2}}{3V^C} \\ \frac{\partial N_3}{\partial x} = -\frac{S_{x3}}{3V^C} & \frac{\partial N_3}{\partial y} = -\frac{S_{y3}}{3V^C} & \frac{\partial N_3}{\partial z} = -\frac{S_{z2}}{3V^C} \\ \frac{\partial N_4}{\partial x} = \frac{S_{x1}+S_{x2}+S_{x3}}{3V^C} = -\frac{S_{x4}}{3V^C} & \frac{\partial N_4}{\partial y} = \frac{S_{y1}+S_{y2}+S_{y3}}{3V^C} = -\frac{S_{y4}}{3V^C} & \frac{\partial N_4}{\partial z} = \frac{S_{z1}+S_{z2}+S_{z3}}{3V^C} = -\frac{S_{z4}}{3V^C}. \end{array} \tag{3.29}$$

The fact that the vector sum of the four facial areas of a tetrahedron is zero has been used to rearrange the derivatives of N_4.

Evaluation of the mass matrix is straightforward. Applying a coordinate transformation to Equation 3.16 yields

$$\begin{aligned} M_{ij}^C &= \int_{V^C} N_i(x,y,z) N_j(x,y,z)\, dV \\ &= \int_0^1 \int_0^{1-\zeta_1} \int_0^{1-\zeta_1-\zeta_2} N_i(\zeta_1,\zeta_2,\zeta_3)\, N_j(\zeta_1,\zeta_2,\zeta_3)\, |J|\, d\zeta_3\, d\zeta_2\, d\zeta_1 \end{aligned} \tag{3.30}$$

where $|J| = 6V^C$, as above. Because of geometrical symmetry, all the diagonal entries of M^C will have the same value, and all the off-diagonal entries will be identical as well. The diagonal terms are

$$\begin{aligned} M_{ii}^C &= M_{11}^C = 6V^C \int_0^1 \int_0^{1-\zeta_1} \int_0^{1-\zeta_1-\zeta_2} N_1^2\, d\zeta_3\, d\zeta_2\, d\zeta_1 \\ &= 6V^C \int_0^1 \int_0^{1-\zeta_1} \int_0^{1-\zeta_1-\zeta_2} \zeta_1^2\, d\zeta_3\, d\zeta_2\, d\zeta_1 \\ &= \tfrac{1}{10} V^C \end{aligned} \tag{3.31}$$

and the off-diagonal terms are

$$\begin{aligned} M_{ij}^C &= M_{12}^C = 6V^C \int_0^1 \int_0^{1-\zeta_1} \int_0^{1-\zeta_1-\zeta_2} N_1 N_2\, d\zeta_3\, d\zeta_2\, d\zeta_1 \\ &= 6V^C \int_0^1 \int_0^{1-\zeta_1} \int_0^{1-\zeta_1-\zeta_2} \zeta_1 \zeta_2\, d\zeta_3\, d\zeta_2\, d\zeta_1 \\ &= \tfrac{1}{20} V^C. \end{aligned} \tag{3.32}$$

In order to obtain a solution using this method, the global mass matrix M_{ij} must be inverted. Because of the off-diagonal terms, this is a difficult and computationally expensive process. For greater efficiency, the mass matrix can be diagonalized to produce the *lumped mass matrix*, which can be inverted trivially. This causes no loss of accuracy if only a steady-state time-asymptotic solution is desired. The lumped mass matrix is formed by summing all the terms of a row of the mass matrix. From Equations 3.31

and 3.32, the terms of the local lumped mass matrix can be found to be

$$M_{ii}^{C} = \tfrac{1}{4} V^{C}. \tag{3.33}$$

The global lumped mass matrix is the sum of the individual local mass matrices. Thus, the entry for a particular node will be one-fourth of the sum of the volumes of the cells that contain that node, which is one-fourth of the supercell volume.

The lumping procedure can be thought to model the unsteady left-hand side in a manner that concentrates the mass, momentum and energy at the mesh node with which each equation is associated. This has the effect of ignoring the rotational inertia of the control volume [12], which results in a loss of order of accuracy. With the use of the lumped mass matrix, the scheme is identical to a finite volume scheme in which the control volume for each node is the supercell of the node.

The residual matrices are also simple to evaluate. Only the residual matrix for the x-direction will be considered in detail. The residual matrices for the y- and z-directions are analogous.

A direct transformation of coordinates applied to Equation 3.17 results in

$$\begin{aligned} R_{X,ij}^{C} &= \int_{V^C} \frac{\partial N_i}{\partial x} N_j \, dV \\ &= \left(\frac{\partial N_i}{\partial x}\right) \int_0^1 \int_0^{1-\zeta_1} \int_0^{1-\zeta_1-\zeta_2} N_j(\zeta_1, \zeta_2, \zeta_3) \, |J| \, d\zeta_3 \, d\zeta_2 \, d\zeta_1 \\ &= -\tfrac{1}{3} S_{x,i} \int_0^1 \int_0^{1-\zeta_1} \int_0^{1-\zeta_1-\zeta_2} \zeta_j \, d\zeta_3 \, d\zeta_2 \, d\zeta_1. \end{aligned} \tag{3.34}$$

As with the mass matrix, many of the terms will be equal. Only the choice of the index i will affect the value of $R_{X,ij}$. For example,

$$\begin{aligned} R_{X,ij}^{C} &= R_{X,i1}^{C} = -\tfrac{1}{3} S_{x,i} \int_0^1 \int_0^{1-\zeta_1} \int_0^{1-\zeta_1-\zeta_2} \zeta_1 \, d\zeta_3 \, d\zeta_2 \, d\zeta_1 \\ &= -\tfrac{1}{12} S_{x,i}. \end{aligned} \tag{3.35}$$

Similarly,

$$\begin{aligned} R^C_{Y,ij} &= -\tfrac{1}{12} S_{y,i} \\ R^C_{Z,ij} &= -\tfrac{1}{12} S_{z,i}. \end{aligned} \tag{3.36}$$

It is now possible to assemble all the pieces to form the semidiscrete form of the Euler equations that is actually used in the solution procedure. Substituting the expressions in Equations 3.33, 3.35 and 3.36 into Equation 3.20, and multiplying by 4, we can obtain

$$V_i \frac{dU_i}{dt} = V_i S_i - \sum_{\text{cells}} R^C = -R_i \tag{3.37}$$

where V_i is the volume of the supercell of node i, and R^C is the flux residual of the cell. The range of the sum is the set of cells that contain node i. The cell residual is given by

$$\begin{aligned} R^C &= -\tfrac{1}{3} \left(\vec{F}_1 \cdot \vec{S}_1 + \vec{F}_2 \cdot \vec{S}_2 + \vec{F}_3 \cdot \vec{S}_3 + \vec{F}_4 \cdot \vec{S}_4 \right) \\ &= -\tfrac{1}{3} \left(F_1 S_{x1} + F_2 S_{x2} + F_3 S_{x3} + F_4 S_{x4} + G_1 S_{y1} + G_2 S_{y2} + G_3 S_{y3} + G_4 S_{y4} \right. \\ &\quad \left. + H_1 S_{z1} + H_2 S_{z2} + H_3 S_{z3} + H_4 S_{z4} \right) \end{aligned} \tag{3.38}$$

This is equivalent to the finite volume form

$$\begin{aligned} R^C &= \tfrac{1}{3} \left(\vec{F}_2 + \vec{F}_3 + \vec{F}_4 \right) \cdot \vec{S}_1 + \tfrac{1}{3} \left(\vec{F}_1 + \vec{F}_3 + \vec{F}_4 \right) \cdot \vec{S}_2 + \tfrac{1}{3} \left(\vec{F}_1 + \vec{F}_2 + \vec{F}_4 \right) \cdot \vec{S}_3 \\ &\quad + \tfrac{1}{3} \left(\vec{F}_1 + \vec{F}_2 + \vec{F}_3 \right) \cdot \vec{S}_4 \end{aligned} \tag{3.39}$$

because the sum of the areas of the four faces of a cell is zero.

3.3 Numerical Boundary Conditions

The physical boundary conditions that are applied to the Euler equations were described in section 2.3. These boundary conditions can be enforced at two types of physical surfaces. At a solid wall boundary, normal velocities are made to vanish, and no flux is permitted through the solid wall. Due to the inviscid nature of the flow, the same conditions are applied at a symmetry surface as at a solid wall. At a far field surface, far-field characteristic boundary conditions are prescribed. In addition, special boundary conditions are imposed at the intersection of certain surfaces.

3.3.1 Choice of Boundary Condition at Intersecting Surfaces

Since the type of boundary condition is specified at the boundary faces, while the boundary conditions are implemented at the nodes, the type of boundary condition to apply at the nodes at the intersection of two faces is ambiguous. Shapiro [74] and Landsberg [41] have found empirically that the far field surface boundary condition should be applied at the nodes at the intersection of a solid surface with a far field surface. In the flows considered in this thesis, all such intersections will actually be between a far field surface and a symmetry surface, but the situation is analogous.

3.3.2 Solid Wall Boundary Condition

Two boundary conditions are applied at a solid boundary. First, the fluxes are restricted so that the non-pressure terms normal to the wall vanish. This condition is applied at the triangular surface faces of the mesh. The flux vectors for a boundary face are

required to have the form

$$F = \begin{bmatrix} \rho u_w \\ \rho u_w u + p \\ \rho u_w v \\ \rho u_w w \\ \rho u_w h \end{bmatrix}, \; G = \begin{bmatrix} \rho v_w \\ \rho u v_w \\ \rho v v_w + p \\ \rho v_w w \\ \rho v_w h \end{bmatrix}, \; H = \begin{bmatrix} \rho w_w \\ \rho u w_w \\ \rho v w_w \\ \rho w_w + p \\ \rho w_w h \end{bmatrix} \tag{3.40}$$

where $\vec{u}_w$ is the tangent component of the velocity, which is given by

$$\begin{aligned} \vec{u}_w &= \vec{u} - u_n \vec{n} \\ &= \vec{u} - (\vec{u} \cdot \vec{n}) \, \vec{n} \end{aligned} \tag{3.41}$$

in which u_n, the normal velocity at the wall, is subtracted from the total velocity. Since the flux integration procedure is cell-based, this boundary condition is implemented by constructing a correction flux term, to be added to all nodes whose supercells contain a solid wall face. This includes not only the nodes of the triangles on the surface, but the "peak" nodes of the tetrahedra that have a solid surface triangle one of their faces. The cell residual expression of equation 3.38 is modified to be

$$R^C = -\tfrac{1}{3} \left(\vec{F}_1 \cdot \vec{S}_1 + \vec{F}_2 \cdot \vec{S}_2 + \vec{F}_3 \cdot \vec{S}_3 + \vec{F}_4 \cdot \vec{S}_4 \right) + \tfrac{1}{3} \delta \vec{F} \cdot \vec{S}^F, \tag{3.42}$$

where $\vec{S}^F$ is the area vector of the face, and

$$\delta \vec{F} = \vec{F}_w - \vec{F}^F \tag{3.43}$$

is the corrective flux vector, where the quantity $\vec{F}_w$ is the wall flux vector whose components are given in equation 3.40, and $\vec{F}^F$ is the uncorrected face flux vector, which is the average of the flux vectors at the three nodes of the face. The pressure terms cancel, and the difference between the wall tangent velocity, $\vec{u}_w$, and the uncorrected velocity, $\vec{u}$, is simply the normal velocity, $\vec{u}_n$. The components of the corrective flux

vector are thus

$$\delta F = \begin{bmatrix} \rho u_n \\ \rho u u_n + p \\ \rho u_n v \\ \rho u_n w \\ \rho u_n h \end{bmatrix}, \delta G = \begin{bmatrix} \rho v_n \\ \rho u v_n \\ \rho v v_n + p \\ \rho v_n w \\ \rho v_n h \end{bmatrix}, \delta H = \begin{bmatrix} \rho w_n \\ \rho u w_n \\ \rho v w_n \\ \rho w w_n + p \\ \rho w_n h \end{bmatrix} \tag{3.44}$$

It is possible that a single tetrahedral cell may border more than one solid face. In this situation, the appropriate face boundary conditions are applied separately to the nodes.

It is also necessary to explicitly force the velocity to be tangent to the wall. The velocity at each node on a solid boundary is set to its tangent component $\vec{u}_w$, which is found using equation 3.41. This enforcement is necessary since the condition of no flux across the surface boundary can be satisfied in the presence of an odd-even type of error mode at the boundary nodes, which averages to the correct flux values at the faces. The unit normal vector at the nodes in calculated as an area-weighted average of the normal vectors of the triangular boundary faces that contain the node.

3.3.3 Symmetry Surface Boundary Condition

The boundary conditions that are applied at a symmetry boundary are the same as those applied at a solid wall.

3.3.4 Edge Boundary Condition

Special boundary conditions are applied at some nodes that are at the intersection of two solid or symmetry surfaces. There are two different kinds of intersection boundaries, which are termed edge boundaries and corner boundaries.

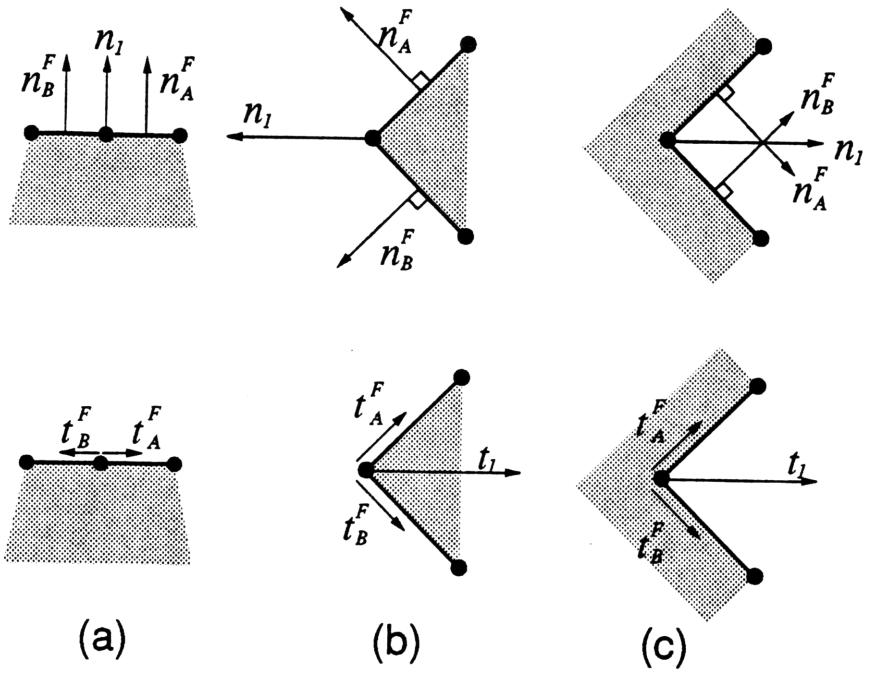

Figure 3.4: Normal and tangent vectors at a node on the boundary: (a) flat surface, (b) sharp edge, (c) sharp corner.

An edge boundary is located at the intersection of two solid surfaces in the case that the solid body protrudes into the fluid, such as at the trailing edge of a wing. To treat such a point as if it were on a solid boundary would invite the fluid velocity to become infinite, as the radius of curvature of the surface would approach zero. The Kutta condition explicitly constrains the fluid velocity to be finite, and is physically enforced through the action of viscosity. Numerically, artificial dissipation is sufficient to impose the Kutta condition. At sharp edge nodes, no boundary condition is directly applied. Instead, the switch that controls the numerical smoothing (see section 3.4) is adjusted so that the second-difference smoothing is applied at the edge nodes, and at the nodes nearby.

3.3.5 Corner Boundary Condition

A corner boundary is located at the intersection of a symmetry surface with a solid surface, in the case that the fluid protrudes into the solid body. In theory, the intersection of two solid boundaries, such as at the fuselage-wing juncture, could also be

treated as a corner boundary. However, it is valid to model such an intersection as part of a solid surface in which the normal direction is taken to be the average of the two normal directions of the surfaces that intersect. Such an approach is inappropriate if one surface is a symmetry boundary.

The boundary condition that is applied at the corner is that the flow has no component normal to either of the two intersecting surfaces. The velocity is set to

$$\vec{u}_c = \vec{u} - (\vec{u}\cdot\vec{n}_1)\,\vec{n}_1 - (\vec{u}\cdot\vec{n}_2)\,\vec{n}_2 \tag{3.45}$$

where $\vec{n}_1$ and $\vec{n}_2$ are the surface normal vectors of the two intersecting boundaries.

An intersection boundary is categorized as an edge boundary or a corner boundary based on the relative orientation of two vectors, the nodal surface normal vector, and the nodal surface tangent vector (see figure 3.4). The nodal surface normal vector is the area-weighted average of the normal vectors of all boundary faces of which a node is a corner, while the nodal surface tangent vector is the area-weighted average of the vectors from the node in question to the centroid of each of the boundary faces of which a node is a corner. If the boundary is flat, and the surface mesh is uniform, the nodal tangent vector vanishes. If the surface mesh is stretched, but still flat, the tangent vector is in the plane of the surface, and of course, orthogonal to the normal vector. If the surface normal is discontinuous, which will be the case at all nodes on a sharp intersection boundary, the tangent vector will roughly bisect the dihedral angle of the surface. Since the average normal vector points into the fluid, the sign of the scalar product of the normal and tangent vectors will indicate whether a node is a member of an edge boundary or of a corner boundary.

3.3.6 Far Field Surface Boundary Condition

The analytical far field boundary condition is that the flow approaches a limiting form as distance approaches infinity. Numerically, boundaries must be located at a finite distance. The boundary condition that is imposed is derived with the goal that transient disturbances are transmitted through the boundary with minimal reflection. The derivation follows Jameson and Baker's [30] application of the method of characteristics. To begin the derivation, the Euler equations are written in a coordinate system, (n, t, b), that is normal and tangential to the boundary. The equations are then linearized, and it is assumed that derivatives in the normal direction are much larger than those in the tangential directions. This results in a one-dimensional partial differential equation. This equation is diagonalized by the assumption of locally isentropic flow (which Landsberg [41] found is valid for vortex flows), to produce the characteristic equation,

$$\frac{\partial C}{\partial t} = \Lambda \frac{\partial C}{\partial n} \tag{3.46}$$

in which the five equations are decoupled. The characteristic quantities are

$$\begin{bmatrix} C_1 \\ C_2 \\ C_3 \\ C_4 \\ C_5 \end{bmatrix} = \begin{bmatrix} R_{\text{in}} \\ R_{\text{out}} \\ u_{\text{t}} \\ u_{\text{b}} \\ e^s \end{bmatrix} = \begin{bmatrix} u_{\text{n}} + \frac{2a}{\gamma - 1} \\ u_{\text{n}} - \frac{2a}{\gamma - 1} \\ (\vec{u} - u_{\text{n}}\vec{n}) \cdot \vec{t} \\ (\vec{u} - u_{\text{n}}\vec{n}) \cdot \vec{b} \\ \frac{p}{\rho^\gamma} \end{bmatrix} \tag{3.47}$$

where R_{in} and R_{out} are the Riemann invariants, and s is the entropy. The wave speeds associated with the characteristics are

$$\begin{aligned} R_{\text{in}} &: u_{\text{n}} + a \\ R_{\text{out}} &: u_{\text{n}} - a \\ \vec{u}_{\text{t}} &: u_{\text{n}} \\ e^s &: u_{\text{n}}. \end{aligned} \tag{3.48}$$

The tangential velocity is kept as a vector, $\vec{u}_t$, to avoid the necessity of computing the tangential coordinate directions. This velocity has only two degrees of freedom, not three.

The sign of the associated wave speed determines whether the characteristic quantities are convected from within the computational domain or from without, which corresponds to whether they are calculated based on the internal or prescribed state quantities. This is summarized in the following table:

	Inflow		Outflow	
	$(u_n \geq 0)$		$(u_n < 0)$	
	$M_n > 1$	$M_n < 1$		$M_n > 1$
R_{in}	P	P	P	I
$\vec{u}_t \quad e^s$	P	P	I	I
R_{out}	P	I	I	I

where $M_n = u_n/a$ is the Mach number normal to the boundary, as computed by the internal field flow solver. Inflow conditions are applied at nodes where $u_n \geq 0$, while outflow conditions are applied at nodes where $u_n < 0$. Note that since the normal velocity u_n is formed by a dot product with an inward-pointing normal vector, the behavior of the Riemann invariants R_{in} and R_{out} at the outflow boundary are the reverse of what may appear in some references.

The primitive variables are recovered from the characteristic variables by

$$\begin{aligned} u_n &= \tfrac{1}{2}\left(R_{in} + R_{out}\right) \\ a &= \tfrac{\gamma-1}{4}\left(R_{in} - R_{out}\right) \\ \vec{u} &= u_n\vec{n} + u_t\vec{t} + u_b\vec{b} \\ \rho &= \left(\frac{a^2}{\gamma e^s}\right)^{\frac{1}{\gamma-1}} \\ p &= \frac{\rho a^2}{\gamma} \end{aligned} \tag{3.49}$$

from which the state vector is recomputed.

In two-dimensional computations, the prescribed far field is frequently expressed as a free stream with corrective terms added, so that accuracy can be maintained with the external boundary closer to the body [82]. The corrective terms frequently are based on the potential flows due to a point vortex, to model lift, or a doublet, to model volume. While analogous expressions exist for three-dimensional lifting wings [38], Steger and Bailey [2] demonstrated that, for three-dimensional potential flow calculations, including the corrective terms does not produce a substantial improvement in accuracy. Therefore, the free stream is used as the prescribed far field flow in this thesis.

3.4 Artificial Dissipation

Artificial dissipation is necessary to achieve temporal and spatial stability. The dissipation at a node i is a mix of second- and fourth-difference terms, which can be represented as

$$D_i = D(U_i) = \mathcal{D}\left(\kappa_2 \mathcal{D} U_i - \kappa_4 \mathcal{D}(\mathcal{D}^2 U_i)\right) \tag{3.50}$$

where the second- and fourth-difference terms are weighted by

$$\begin{aligned} \kappa_2 &= \frac{V}{\Delta t_{\max}} s\varepsilon_2 \\ \kappa_4 &= \frac{V}{\Delta t_{\max}} (1-s)\varepsilon_4 \end{aligned} \tag{3.51}$$

and $\mathcal{D}$ and $\mathcal{D}^2$ are first- and second-difference operators, respectively. The combination $\mathcal{D}(\kappa_2 \mathcal{D} U_i)$ is actually a type of second-difference operator. The fourth-difference operator is evaluated as two nested second-difference operators. The details of these operators will be discussed below.

The amount of second- and fourth-difference dissipation in equation 3.50 is controlled by a pressure switch s originally designed to locate shocks. The switch is calculated at the nodes as

$$s_i = \frac{|\mathcal{D}^2 p_i|}{p_i} \tag{3.52}$$

and is then normalized by its greatest value in the flow field so that $0 \leq s_i \leq 1$. In addition, the second-difference smoothing is used to enforce the Kutta condition at sharp edges, as discussed in section 3.3. This is attained by setting the value of the switch s_i to unity at nodes on or near a sharp edge at which the Kutta condition is imposed.

If it is known *a priori* that there will be no shocks and no separation in the flow field, only fourth-difference smoothing is used, and the pressure switch is unnecessary.

The quantities ε_2 and ε_4 are empirical coefficients for the second- and fourth-difference dissipation. The values of the coefficients are chosen to achieve rapid convergence without excessively corrupting the solution. Typical values are around $\varepsilon_4 = 0.01$, and the range $\varepsilon_2 = 0.05$ to $\varepsilon_2 = 0.15$

There are two types of second difference operators $\mathcal{D}^2$ that will be discussed, the conservative low-accuracy operator, and the high-accuracy nonconservative operator. The latter is only used to form the fourth-difference operator.

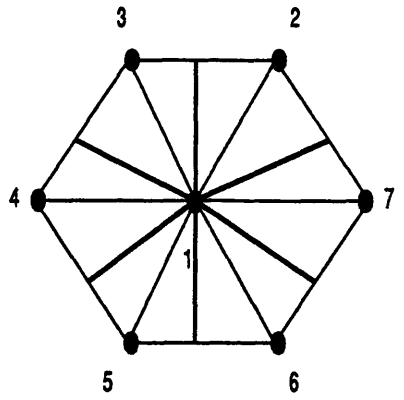

Figure 3.5: Section of an unstructured mesh, with node-to-face-center edges

3.4.1 Conservative low-accuracy second difference operator

The conservative low-accuracy second-difference operator is based on an analogy to the structured grid operator for the second difference of a quantity Q,

$$\mathcal{D}^2 Q_{ijk} = Q_{i+1,jk} + Q_{i-1,jk} + Q_{i,j+1,k} + Q_{i,j-1,k} + Q_{ij,k+1} + Q_{ij,k-1} - 6Q_{ijk} \quad (3.53)$$

which can be rewritten as the sum of the differences along the edges that emanate from the node at which the difference is calculated,

$$\begin{aligned} \mathcal{D}^2 Q_{ij} &= (Q_{i+1,j,k} - Q_{i,j,k}) + (Q_{i-1,j,k} - Q_{i,j,k}) + (Q_{i,j+1,k} - Q_{i,j,k}) \\ &+ (Q_{i,j-1,k} - Q_{i,j,k}) + (Q_{i,j,k+1} - Q_{i,j,k}) + (Q_{i,j,k-1} - Q_{i,j,k}). \end{aligned} \quad (3.54)$$

The analogous formula for the second difference at a node of an unstructured mesh is constructed as the sum of the differences along line segments that join the node to the centers of the faces of its supercell, a two-dimensional analogy of which is shown in figure 3.5. In the figure, the edges that join node 1 to to the face centers are bold lines. Thus, the second difference at node 1 is given by

$$\mathcal{D}^2 Q_1 = \sum_{\substack{\text{faces of} \\ \text{supercell}}} (Q_{\text{face}} - Q_1). \quad (3.55)$$

For a tetrahedron, the term resulting from the face with corners nodes 2, 3 and 4 is

$$\begin{aligned} \mathcal{D}^2 Q_{1,234} &= Q_{234} - Q_1 \\ &= \tfrac{1}{3}(Q_2 + Q_3 + Q_4) - Q_1. \end{aligned} \tag{3.56}$$

The advantage of this representation is that the contribution from the face can be thought of as the contribution from cell C, which is defined by node 1 and the face in question.

$$\begin{aligned} \mathcal{D}^2 Q_1^C &= \tfrac{1}{3}(Q_2 + Q_3 + Q_4) - Q_1 \\ &= \tfrac{1}{3}(Q_2 + Q_3 + Q_4 - 3Q_1) \\ &= \tfrac{1}{3}(Q_1 + Q_2 + Q_3 + Q_4 - 4Q_1) \\ &= \tfrac{4}{3}\left(Q^C - Q_1\right) \end{aligned} \tag{3.57}$$

where Q^C, the value at cell C, is the average of the values at nodes 1, 2 3, and 4. The second difference can be scaled by a constant without affecting its behavior, so that the factor of $\frac{4}{3}$ can be dropped. The cell C will contribute to its nodes the amounts

$$\begin{aligned} \mathcal{D}^2 Q_1^C &= Q^C - Q_1 \\ \mathcal{D}^2 Q_2^C &= Q^C - Q_2 \\ \mathcal{D}^2 Q_3^C &= Q^C - Q_3 \\ \mathcal{D}^2 Q_4^C &= Q^C - Q_4. \end{aligned} \tag{3.58}$$

The total contribution from cell C to its four nodes is zero. Therefore the net change in the entire solution is zero, so this operator is conservative.

The advantage of this operator is that it is quick to compute, and it is conservative. The disadvantage is that a two-dimensional solver that uses this type of operator to calculate smoothing is less than second-order accurate on an irregular mesh, as demonstrated by Lindquist [45]. In this context, an irregular mesh is a mesh in which there is variation in the number of faces of the supercells of the nodes. Since there is no

regular tessellation of three-dimensional space with tetrahedra, it is expected than any three-dimensional mesh will be irregular.

3.4.2 High-accuracy nonconservative second difference operator

The high-accuracy nonconservative second-difference operator is based on the low-accuracy second-difference operator of section 3.4.1. The goal in creating the high-accuracy operator is that it does not smooth a linear function, which will be referred to here as being second-order accurate. In order to attain second-order accuracy, the operator 3.58 is modified by the insertion of a weight ε_i^C for each node of each cell. The modified smoothing operator is

$$\mathcal{D}_x^2 Q_1^C = \left(Q^C - Q_1\right)\left(1 + \varepsilon_1^C\right) \tag{3.59}$$

with the result that the smoothing of the linear function $Q(x, y, z) = x$ is

$$\mathcal{D}_x^2 x = \sum_{\text{cells}} \left(x^C - x_1\right)\left(1 + \varepsilon_1^C\right). \tag{3.60}$$

The smoothing weights ε_1^C for one node are solved for by minimizing the norm

$$\sum_{\text{cells}} \left(\varepsilon_1^C\right)^2 \tag{3.61}$$

subject to the requirement that a linear function is not smoothed. This approach was first implemented in two dimensions by Holmes and Connell [27], and extended to three dimensions by Saxer [73]. The requirement is equivalent to the three constraints

$$\begin{aligned} \mathcal{D}_x^2 x_i &= 0 \\ \mathcal{D}_y^2 y_i &= 0 \\ \mathcal{D}_z^2 z_i &= 0 \end{aligned} \tag{3.62}$$

where $\mathcal{D}_y^2 Q_i$ and $\mathcal{D}_z^2 Q_i$ are defined in a manner similar to equation 3.59. The constrained minimization is performed by the technique of Lagrange multipliers [77], with the Lagrangian function being

$$\mathcal{L}(\varepsilon_1^C, \lambda_x, \lambda_y, \lambda_z) = \sum_{\text{cells}} \left(\varepsilon_1^C\right)^2 + \lambda_x \sum_{\text{cells}} \left(x^C - x_1\right)\left(1 + \varepsilon_1^C\right) + \lambda_y \sum_{\text{cells}} \left(y^C - y_1\right)\left(1 + \varepsilon_1^C\right) + \lambda_z \sum_{\text{cells}} \left(z^C - z_1\right)\left(1 + \varepsilon_1^C\right). \tag{3.63}$$

Differentiating with respect to the Lagrange multipliers recovers the constraint equations, while differentiating with respect to ε_1^C results in

$$\frac{\partial \mathcal{L}}{\partial \varepsilon_1^C} = 2\varepsilon_1^C + \lambda_x \left(x^C - x_1\right) + \lambda_y \left(y^C - y_1\right) + \lambda_z \left(z^C - z_1\right). \tag{3.64}$$

Setting this to zero allows the smoothing weights to be expressed as

$$\varepsilon_1^C = -\tfrac{1}{2}\left[\lambda_x \left(x^C - x_1\right) + \lambda_y \left(y^C - y_1\right) + \lambda_z \left(z^C - z_1\right)\right] \tag{3.65}$$

which is then substituted into the constraints (3.62) to produce the system of equations

$$\begin{aligned} I_{xx}\lambda_x + I_{xy}\lambda_y + I_{xz}\lambda_z &= R_x \\ I_{xy}\lambda_x + I_{yy}\lambda_y + I_{yz}\lambda_z &= R_y \\ I_{xz}\lambda_x + I_{yz}\lambda_y + I_{zz}\lambda_z &= R_z \end{aligned} \tag{3.66}$$

where

$$\begin{aligned} I_{xx} &= \sum_{\text{cells}} \left(x^C - x_1\right)^2 & I_{xy} &= \sum_{\text{cells}} \left(x^C - x_1\right)\left(y^C - y_1\right) & I_{xz} &= \sum_{\text{cells}} \left(x^C - x_1\right)\left(z^C - z_1\right) \\ I_{yy} &= \sum_{\text{cells}} \left(y^C - y_1\right)^2 & I_{yz} &= \sum_{\text{cells}} \left(y^C - y_1\right)\left(z^C - z_1\right) & I_{zz} &= \sum_{\text{cells}} \left(z^C - z_1\right)^2 \\ R_x &= 2\sum_{\text{cells}} \left(x^C - x_1\right) & R_y &= 2\sum_{\text{cells}} \left(y^C - y_1\right) & R_z &= 2\sum_{\text{cells}} \left(z^C - z_1\right). \end{aligned} \tag{3.67}$$

This system can be solved to find the Lagrange multipliers:

$$\begin{aligned}
\lambda_x &= \frac{1}{D}\left(R_x I_{yy} I_{zz} + R_y I_{xz} I_{yz} + R_z I_{yz} I_{xz} - R_z I_{yy} I_{xz} - R_y I_{xy} I_{zz} - R_x I_{yz}^2\right) \\
\lambda_y &= \frac{1}{D}\left(R_y I_{xx} I_{zz} + R_x I_{yz} I_{xz} + R_z I_{xy} I_{xz} - R_x I_{xy} I_{zz} - R_y I_{xz}^2 - R_z I_{xz} I_{xx}\right) \\
\lambda_z &= \frac{1}{D}\left(R_x I_{xy} I_{yz} + R_y I_{xy} I_{xz} + R_z I_{xx} I_{yy} - R_x I_{yy} I_{xz} - R_y I_{yz} I_{xx} - R_z I_{xy}^2\right)
\end{aligned} \tag{3.68}$$

where the denominator is

$$D = I_{xx} I_{yy} I_{zz} + 2\, I_{xy} I_{yz} I_{xz} - I_{xz}^2 I_{yy} - I_{xy}^2 I_{zz} - I_{yz}^2 I_{xx} \tag{3.69}$$

which can be used in conjunction with equation 3.65 to determine the set of smoothing weights for the node.

The smoothing weights depend only on the mesh geometry. Thus, they do not meaningfully increase the computational burden of this smoothing operator, although they do greatly increase the memory storage required.

3.4.3 Complete dissipation operator

The low-accuracy second difference operator is used as described in section 3.4.1 to calculate the unscaled pressure switch s_i at the nodes. The fourth-difference background smoothing operator consists of two second-difference operators applied consecutively. First, the high-accuracy nonconservative operator of section 3.4.2 is used to create a second difference. Then, an operator based on the conservative low-accuracy operator uses this second difference to create a fourth difference. This operator differs from that of section 3.4.1 by the inclusion of dimensional scaling and the effect of the pressure switch. These details are described in this section.

The second-difference shock smoothing operator is based on the low-accuracy oper-

ator described in section 3.4.1. Two modifications must be made to Equation 3.58, to insure proper dimensionality, and to include the effect of the pressure switch. Except as noted, these modifications also apply to the outer second-difference operator of the fourth difference smoothing.

First, it is necessary to cancel the factor $\Delta t/V$ that appears in the time integration scheme (Equation 3.74), so that the computed changes in the state vector are dimensionally consistent with the state vector itself. The smoothing terms are multiplied by a factor r where, as in Equation 3.76,

$$r = 2 \sum_{\text{faces}} \left(|\vec{u}^F \cdot \vec{S}^F| + a^F S^F \right) \tag{3.70}$$

is related to the spectral radius of the flux Jacobian. Unlike the nodal supercells, the cells have a fixed topology, so that r^C can be expressed directly as

$$r^C = 2 \left(|\vec{u}_1 \cdot \vec{S}_1| + a_1 S_1 + |\vec{u}_2 \cdot \vec{S}_2| + a_2 S_2 + |\vec{u}_3 \cdot \vec{S}_3| + a_3 S_3 + |\vec{u}_4 \cdot \vec{S}_4| + a_4 S_4 \right). \tag{3.71}$$

Also, the second- and fourth-difference terms have to be scaled by use of the pressure switch s_i. These factors cannot simply multiply the complete difference operator at the nodes, as that would not be conservative. The multiplication must be carried out at the cell level of computation, so that a cell's contributions to its four nodes will still sum to zero. The pressure switch is averaged amongst the nodes to obtain values at the cells.

In the rescaled smoothing scheme, the cell C contributes the amount

$$\mathcal{D}^2 Q_1^C = W^C r^C \left(Q^C - Q_1 \right) \tag{3.72}$$

to node 1 when using the conservative low-accuracy second-difference operator, where W^C is a weighting function

$$W^C = \begin{cases} s^C, & \text{for second-difference smoothing term} \\ 1 - s^C, & \text{for fourth-difference smoothing term.} \end{cases} \tag{3.73}$$

In the case of the shock-smoothing term, the quantity Q is the state quantity that is being smoothed, whereas in the case of the background smoothing, Q is the second difference of the state quantity, which was computed using the high-accuracy second-difference operator.

3.5 Temporal discretization

A four-stage modified Runge-Kutta time-stepping scheme is used.

$$\begin{aligned}
U_i^{(0)} &= U_i^n \\
U_i^{(1)} &= U_i^{(0)} + \alpha_1 \frac{\Delta t_i}{V_i} \left(-\lambda R_i^{(0)} + D_i^{(0)} \right) \\
U_i^{(2)} &= U_i^{(0)} + \alpha_2 \frac{\Delta t_i}{V_i} \left(-\lambda R_i^{(1)} + D_i^{(1)} \right) \\
U_i^{(3)} &= U_i^{(0)} + \alpha_3 \frac{\Delta t_i}{V_i} \left(-\lambda R_i^{(2)} + D_i^{(2)} \right) \\
U_i^{(4)} &= U_i^{(0)} + \alpha_4 \frac{\Delta t_i}{V_i} \left(-\lambda R_i^{(3)} + D_i^{(3)} \right) \\
U_i^{n+1} &= U_i^{(4)}
\end{aligned} \tag{3.74}$$

where $\alpha_1 = \frac{1}{4}, \alpha_2 = \frac{1}{3}, \alpha_3 = \frac{1}{2}, \alpha_4 = 1$, Δt is the time step, D_i is the artificial dissipation. $R_i^{(0)}$ is the residual at stage zero, etc. Note that the CFL number, λ, has been separated from the time step, Δt. This is to prevent the dissipation from being scaled by the CFL number, which is desirable to have similar stability characteristics when the CFL number is changed. This also has the effect that the steady solution depends on the CFL number, as well as on the smoothing coefficients ε_2 and ε_4. However, the variation of λ is smaller than the typical variation of the smoothing coefficients.

Residuals are calculated at every stage, and dissipation will only be evaluated as often as is required for stability. In practice, it was found that the fourth difference dissipation could be frozen after the first stage, whereas the second difference dissipation must be evaluated at the second stage as well. This is due to the greater value of the

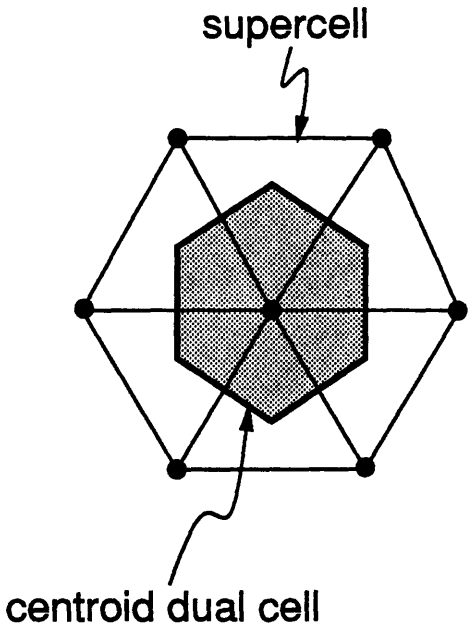

Figure 3.6: Supercell and centroid dual cell of a node

second difference smoothing coefficient, ε_2.

3.5.1 Time step

The time step, Δt, is calculated individually for each node. The calculation is performed at every Runge-Kutta stage. When computing steady-state flows, the local time step is used to accelerate convergence, so that Δt_i is different for each node. This Δt is not the same quantity that is usually called the time step. It differs by the omission of the CFL number, λ, which is incorporated separately into the temporal integration procedure of equation 3.74. The time step for node i is given by

$$\Delta t_i = \frac{V_i}{r_i} \tag{3.75}$$

where V_i is the volume of the supercell of node i, and r_i is given by

$$r_i = 2 \sum_{\text{faces}} \left(|\vec{u}^F \cdot \vec{S}^F| + a^F S^F \right) \tag{3.76}$$

where $\vec{u}^F$ is the average fluid velocity for a face of the supercell, a^F is the average sonic speed for the face and $S^F = |\vec{S}^F|$ is the area of the face. This quantity r_i is calculated based on the cells. The contributions by a cell C to each of its four nodes are

$$\begin{aligned}
r_1^C &= 2\left\{\left|\tfrac{1}{3}(u_2+u_3+u_4)S_{x1} + \tfrac{1}{3}(v_2+v_3+v_4)S_{y1} + \tfrac{1}{3}(w_2+w_3+w_4)S_{z1}\right| \right. \\
&\quad \left. + \tfrac{1}{3}(a_2+a_3+a_4)S_1\right\} \\
r_2^C &= 2\left\{\left|\tfrac{1}{3}(u_1+u_3+u_4)S_{x2} + \tfrac{1}{3}(v_1+v_3+v_4)S_{y2} + \tfrac{1}{3}(w_1+w_3+w_4)S_{z2}\right| \right. \\
&\quad \left. + \tfrac{1}{3}(a_2+a_3+a_4)S_1\right\} \\
r_3^C &= 2\left\{\left|\tfrac{1}{3}(u_1+u_2+u_4)S_{x3} + \tfrac{1}{3}(v_1+v_2+v_4)S_{y3} + \tfrac{1}{3}(w_1+w_2+w_4)S_{z3}\right| \right. \\
&\quad \left. + \tfrac{1}{3}(a_2+a_3+a_4)S_1\right\} \\
r_4^C &= 2\left\{\left|\tfrac{1}{3}(u_1+u_2+u_3)S_{x4} + \tfrac{1}{3}(v_1+v_2+v_3)S_{y4} + \tfrac{1}{3}(w_1+w_2+w_3)S_{z4}\right| \right. \\
&\quad \left. + \tfrac{1}{3}(a_2+a_3+a_4)S_1\right\}.
\end{aligned} \tag{3.77}$$

The quantity r is related to the spectral radius of the flux Jacobian $\partial F_i/\partial U_j$, or the largest absolute value of the eigenvalues of the matrix. The expression for the spectral radius differs from the expression for r in that the sum is over the faces of the centroid dual polygon of node i, rather than the supercell, as shown for the analogous two-dimensional situation in Figure 3.6. If the spectral radius were used in place of r_i in Equation 3.75 then the CFL limit would be the same as for a one-dimensional analysis, as shown by Giles [21]. Since the dual polygon has about one-fourth the volume of the supercell, the spectral radius should be smaller than r_i by about a factor $4^{2/3}$, and the CFL limit will be less strict by the same factor. Since the one-dimensional four-stage Runge-Kutta scheme has a stability limit of $\lambda \leq 2\sqrt{2}$, the stability limit for this scheme is $\lambda \leq 2\sqrt{2} \times 4^{2/3}$, which is approximately 7.127. In practice, this value of λ cannot be attained. The practical CFL limit is roughly 6.

3.5.2 Regional Local Time Steps

When computing steady-state flows, the local time step is used to accelerate convergence. For strict time-accuracy, however, the same time step must be used at each node. This can lead to problems if the local time steps vary widely from node to node. This will occur when the mesh spacing has a wide variation, since the local time step, as calculated by equation 3.75, scales roughly with a local length scale of the mesh. Thus, very fine mesh spacing will create a very strict global time step limitation. This yields a stiff system of equations, with the time step being determined by a restrictive stability criterion, rather than by accuracy considerations.

The use of local time steps in a time accurate calculation will introduce inaccuracies in the solution. The global effect of the inaccuracies can be minimized by restricting the use of local time steps to the most closely spaced regions of the mesh, where the smallest local time steps will occur. The solution in the coarser regions of the mesh is integrated in a strict time accurate fashion, but with a larger time step, so that the calculation can be performed in fewer iterations. The extent of the use of local time steps is quantified by the global time step acceleration factor, f, which is the ratio of the global time step to the minimum local time step. It is also the factor by which the number of iterations needed to integrate a fixed time interval is decreased. A simple analysis of this scheme (see appendix A) indicates that its effects can be modeled as a time delay, δt, in the propagation of characteristic waves through the region of local time steps. This is a model for the effect on the solution in the time accurate region. In addition, any unsteady physical phenomena in the region of local time steps will have inflated time scales. The magnitude of the time delay, compared to the global time step, is roughly

$$\frac{\delta t}{\Delta t_{\text{global}}} \approx \frac{N}{M_\infty}, \tag{3.78}$$

where M_∞ is the free stream Mach number and N is the number of cells the wave traverses in the local time step region. There are two important conditions in order to obtain a meaningful time accurate solution using local time steps. First, the the

important unsteady physical phenomena should take place in the strictly time accurate region. Second, the time delay introduced by the region of local time steps, described above, should be small compared to the physical time scales. Since the physical time scales and the global time step can typically be estimated *a priori*, equation 3.78 can be used to place a limit on the size of the region of local time steps. Two-dimensional calculations of vortex shedding from a plat plate normal to the free stream validate the concept of using regional local time steps. Details of the two-dimensional solutions are presented in appendix B.

Since the primary vortex above a delta wing is roughly conical in shape, incredibly fine mesh spacing is needed to resolve the vortex near the apex of the wing. However, the unsteady effects are far greater in the region of, and downstream of, the vortex breakdown location. Thus, delta wing flows with vortex bursting are ideal candidates for the use of regional local time steps.

3.6 Data Structure

A general tetrahedral mesh with N_P nodes will contain about $6N_P$ cells. There will be $\mathcal{O}(N_P^{2/3})$ boundary nodes, so that the data storage of boundary quantities will in general be negligible.

Data storage is summarized in tables 3.1 and 3.2. Table 3.1 shows data stored at the nodes, and table 3.2 shows data stored at the cells. The total number of quantities is $209N_P$, of which more than 70% is stored at the cells. This demonstrates one of the major penalties of the use of tetrahedral meshes. Recent publications [4, 48, 60] indicate that an edge based data structure could provide a noticeable decrease in memory storage requirements for unstructured tetrahedral mesh methods.

In addition, connectivity information is required specifying the four nodes of each

Quantity	amount
coordinates x, y, z	$3N_P$
supercell volume V and inverse $1/V$	$2N_P$
state quantities U^n and U^{n+1}	$10N_P$
state quantity changes δU^n	$5N_P$
fluxes F, G, H	$15N_P$
time step divided by supercell volume, $\Delta t/V$	N_P
supercell volume divided by time step, $V/\Delta t$	N_P
residuals R	$5N_P$
pressure p	N_P
pressure switch s	N_P
dissipation D	$5N_P$
state quantity second differences, $\mathcal{D}^2U$	$5N_P$
state quantity fourth differences, $\mathcal{D}^4U$	$5N_P$
Subtotal	$59N_P$

Table 3.1: Nodal memory usage for flow solution procedure

Quantity	amount
Volume of cell divided by time step of the cell	N_C
face areas S_x, S_y, S_z	$12N_C$
smoothing weights ϵ_i^C	$4N_C$
Subtotal	$17N_C$
	$= 102N_P$

Table 3.2: Cellular memory usage for flow solution procedure

cell, which is a total of $24N_P$ pointers. The grand total storage is thus $233N_P$ words. This is typical of flow solvers that use unstructured tetrahedral meshes [46]. The adaptive refinement procedure requires additional storage, which is discussed in section 3.7.6.

3.7 Adaptive Refinement Method

In order to compute an accurate flow solution, it is necessary to have adequate mesh spacing so that flow features are finely resolved. With current computational resources available, it is impractical to obtain a solution using a mesh in which the entire three-

dimensional flow field has the resolution required by the finest scales. Thus, it is necessary to produce meshes in which regions of the flow are only finely resolved if the local flow features warrant such resolution. When the most important flow features appear in a known location, such as the presence of a boundary layer along a solid wall, increased mesh resolution can be specified *a priori*. In other situations, it is possible to provide increased mesh resolution in the general area in which flow features are expected. Frequently this is insufficient, and many schemes exist whereby the flow solution itself is examined to specify the location of additional mesh resolution for a subsequent calculation. Such schemes are referred to as adaptive mesh methods.

There are three basic categories of adaptation schemes, and a fourth technique which is similar. Firstly, it is possible to generate a new mesh from the ground up, taking care to place more mesh nodes in regions specified by the adaptation procedure as being insufficiently resolved. This method, called mesh regeneration [62, 75], results in higher quality meshes, since it is not strongly influenced by the mesh used in the previous calculation, and it allows arbitrary amounts of refinement or de-refinement. However, it requires close coupling with the mesh generation procedure, and, with unstructured mesh generation techniques, it is difficult to control the size of the mesh produced. This procedure can also be used to adapt a structured grid, although with important topological constraints.

A second method retains the connectivity of the initial mesh, but moves the nodes to inadequately resolved regions. Mesh redistribution algorithms prevent the size of the mesh from increasing, thus allowing efficient use of computer resources, but can result in meshes with unacceptable cell shapes and stretching. This can be partly alleviated by changing the connectivity of the mesh while retaining the set of nodes. Mesh redistribution can also be used to adapt a structured grid.

It is also possible to add mesh nodes in regions of interest without changing the existing nodes. This is referred to as mesh-point embedding. There are two common procedures to determine the new cells. In one method, adaptation is performed lo-

cally on a cell-by-cell basis, with cells being subdivided as necessary to maintain mesh connectivity with the embedded nodes [33, 66]. The algorithms required to properly subdivide cells are quite complicated, but need only be developed once. This method maintains the quality of the original mesh, except in an interface region between divided and undivided cells. Embedding methods frequently result in very large meshes, and a separate procedure is needed if it is desired to allow de-refinement as well. In order to be efficient, mesh-point embedding methods also require a large amount of auxiliary data that is often not needed by the flow solver.

Another adaptive embedding method assumes that the original mesh was generated by a Delaunay triangulation method [3], which guarantees that the mesh will possess certain mathematical properties. After a new node has been added, all cells in the vicinity are deleted. Then, it is possible to use the Delaunay mesh generation procedure to construct a set of cells that incorporate the new node, and that fill the same volume as the set of cells that were deleted [49].

Mesh-point embedding cannot be used in the context of a structured grid. However, it is possible to embed entire structured sub-meshes [8], or to embed points in an unstructured mesh that uses hexahedral cells [74], or a mixture of cell types [83].

3.7.1 Adaptation Procedure

An outline of the adaptive refinement procedure is as follows: First, an adaptation parameter is calculated at the mesh nodes. Then, all nodes associated with extreme values of the parameter are indicated for adaptation. Some special refinement associated with repeated adaptation stages is then performed. New nodes are then added at the centers of edges of which both endpoints are indicated for adaptation. Then, the tetrahedral cells and the triangular boundary faces are examined, and are refined based upon the status of their nodes. Each of these steps are described in detail below. This procedure requires an immense amount of connectivity information to be efficient.

3.7.2 Adaptation Parameter

The adaptation parameter, which is intended to locate regions of the flow that require refinement, can be based on mathematical or physical reasoning. Using a mathematical approach, one can construct an operator that will infer the errors in a solution, and select regions of greatest error for refinement. A Richardson extrapolation method [9] can be used to compare the solution on two meshes of different resolution to estimate the truncation errors. Such methods require knowledge of the order of the scheme, and thus work best with regular meshes for which the detailed mathematical behavior of the scheme can be derived. Also, it is possible to use a mesh convergence criterion [65] to identify regions in which further refinement will add more structure. However, mesh convergence methods have not been found to be adequate in three dimensions [51].

A physically based adaptation parameter can be a flow property, or a derivative or a difference of a flow property. In such a case, the flow property is referred to as the *adaptation quantity* and the operator applied to it is the *adaptation measure* [41]. If the flow property itself is the adaptation parameter, then the adaptation measure is the identity operator.

The adaptation parameter should reflect the nature of the expected flow features. In the case of shock dominated flows, an adaptation parameter that reflects compressibility should be used. In a study of two-dimensional transonic flows, Dannenhoffer [13] found that total pressure, or its undivided first or second difference, accurately locates shocks and shock wakes, whereas other flow features such as expansion fans and stagnation zones are best detected by an undivided difference of density, pressure or velocity magnitude.

In the case of vortex dominated flows, there are three quantities that are typically used for adaptation. These are the total pressure loss, Δp_0, the entropy s, and the normalized helicity H_n. The helicity is a kinematic quantity, defined as the scalar product of velocity and vorticity, while the normalized helicity is the scalar product

of the unit vectors in the directions of the velocity and the vorticity, which is also the cosine of the angle between these two vectors. The total presure loss and entropy are popular since they are uniform in steady, irrotational, inviscid flow. Normalized helicity has been used because of the property that it takes on a value of unity along the core of any vortex, and has the potential to equitably detect multiple vortices of different strengths [41]. However, it approaches an indeterminate limit of $H_n \rightarrow \pm 1$ in irrotational regions.

The entropy and the total pressure are related to each other and to the vorticity via Crocco's relation. Although both have been used successfully as adaptation parameters in three dimensions [10, 51], entropy is a superior physical indicator in unsteady flow, as it is a thermodynamic state quantity and thus is independent of reference frame.

If multiple stages of adaptation are to be performed, case must be taken in the choice of a physically based adaptation parameter. If a physical quantity, or its derivative is used, then the extreme values, at which adaptation will be performed, will always be in the same region of the flow. However, as the mesh is refined in these areas, the local errors will decrease, to the point that refinement might be more useful in other regions of the flow, where local errors are undiminished. In a study of two-dimensional transonic flow, Warren *et al.* [86] found that multiply-adapted simulations can converge to the wrong solution if a mesh-independent adaptation parameter is used. Their recommendation is to use as an adaptation parameter a mesh-independent physical quantity that has been multiplied by a local length scale related to the mesh spacing.

3.7.3 Refinement of Edges

The adaptation process is primarily node-based, in that the identification of the region in which refinement is desired is indicated by selecting the nodes in that region. The first step in the adaptation process is to identify the edges both of whose endpoints

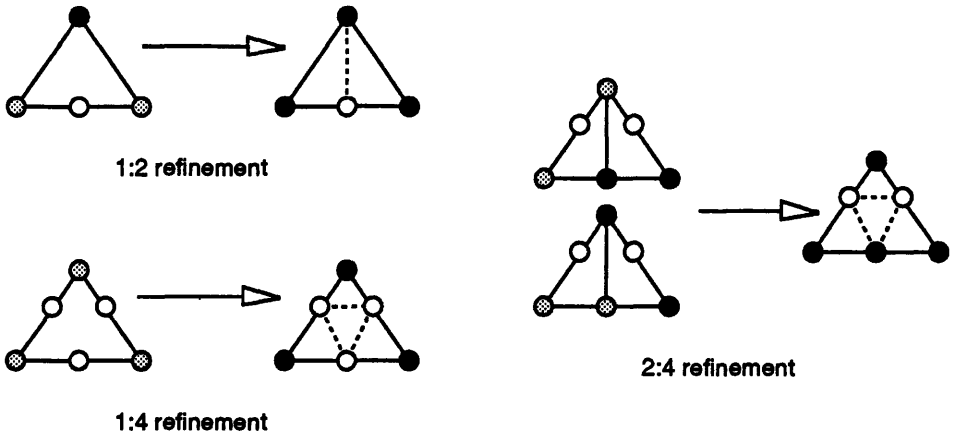

Figure 3.7: Refinement of a triangle

are indicated for adaptation, and to refine these edges by creating a new node at the midpoint of the edge and dividing the edge in two. The indices of the new node and the new edge are associated with the original edge, to be used to identify the nodes and edges of triangles and tetrahedra during the refinement of boundary faces and cells.

3.7.4 Refinement of Boundary Faces

The refinement of the triangular boundary faces is very similar to the refinement of triangular cells in two dimensions. There are two principal ways that a triangle can be refined, and an additional way that is used only in special cases involved with multiple stages of adaptation. The three types of refinement are depicted in figure 3.7. In this figure, the grey shaded nodes are the nodes of the triangle for which adaptation is indicated, the dark shaded nodes are the nodes for which adaptation is not indicated, and the unshaded nodes are the new nodes that are created by the adaptation process. Likewise, the solid lines are mesh edges that exist prior to refinement, and the dashed lines are edges that are created within the triangle during the refinement process. The

two general refinement types will be described first.

The choice of refinement type is based on the status of the adaptation indicator at the three nodes of the triangle. If all three nodes are indicated for adaptation, then the triangle is divided into four sub-triangles, one in the center and one at each corner. The nodes and edges of the new triangle are identified by reference to the edges of the original triangle. This is referred to as one to four, or 1:4 refinement, and is shown in the lower left of figure 3.7. In the case that only two nodes of a triangle are indicated for adaptation, the triangle is divided into two sub-triangles, and is marked for special treatment if there is to be any subsequent stages of adaptation. This is referred to as 1:2 refinement, and is shown in the upper left of figure 3.7. If only one node is indicated for adaptation, no refinement is performed on that triangle.

Triangles that have been refined 1:2 should not be treated in the normal manner in a subsequent stage of adaptation. If the three nodes at the base of the set of triangles are indicated for adaptation, the normal procedure would direct that both subtriangles be refined 1:2, producing four very skinny triangles. Such triangles degrade the accuracy and stability of the flow solution scheme, and thus should be avoided. What is done in the case of refinement of a pair of triangles is to reconstruct the original triangle and do divide it into four subtriangles in the 1:4 manner. This special type of refinement is referred to as 2:4 refinement, and is shown at on right in figure 3.7. It is possible that after 2:4 refinement that one of the base edges of the set of triangles will still need to be refined. For example, in the lower triangle in figure 3.7, two nodes at the base of the set of triangles are indicated for adaptation. These two nodes will remain indicated after 2:4 refinement is complete, with the result that the lower left triangle in the set of four triangles will be refined in the 1:2 manner, after all the special cases have been resolved.

It is also possible to base adaptation on an indicator associated with the edges of the mesh. In such a system, a triangle undergoes a type of refinement based upon the number of its edges for which adaptation is indicated. A triangle of which three edges

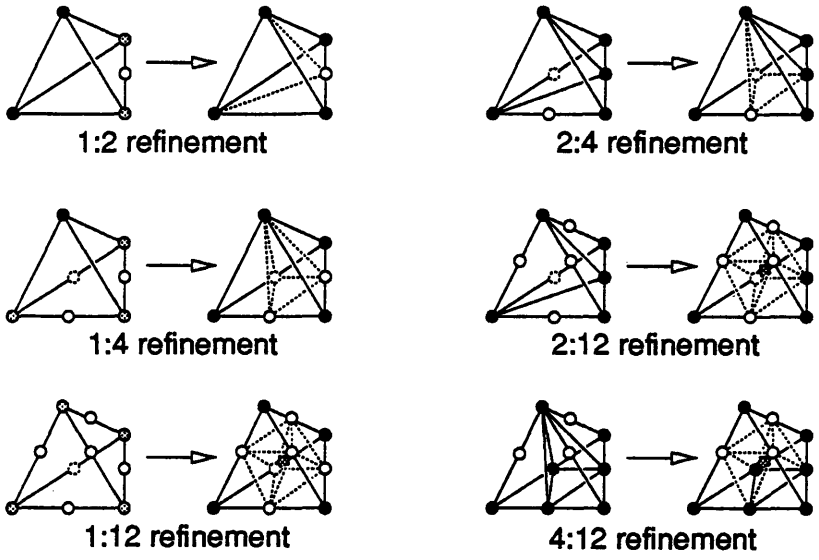

Figure 3.8: Refinement of a tetrahedron

are indicated for adaptation is refined is divided into four triangles, as if its three nodes were indicated for adaptation in this scheme. A triangle of which one edge is indicated for adaptation is refined in the 1:2 manner, as if two of its nodes were indicated for adaptation. However, if two edges are indicated for adaptation, the triangle must either be refined in a special way, or must be promoted to 1:4 status. In the latter case, the edge which previously was not indicated for adaptation must be refined, and the neighboring triangle that shares the this edge must be reconsidered as to what type of refinement it must undergo. In addition, the treatment of special cases is horrendously intricate. It is to avoid these two complications that the choice of node-based adaptation was made.

3.7.5 Refinement of Cells

The refinement of the tetrahedral cells is similar in principle to that of the triangular boundary faces, but is more complex. There are three types of general and three types of special refinement. These are shown in figure 3.8. The ordinary refinement situation

is very much like that which is applied to the triangles, except that the case of full refinement produces twelve subtetrahedra, and a new node is created at the center of the original cell. It is also possible to divide the cell into eight cells, but the 1:12 refinement is symmetric with respect to the nodes.

The two types of partial refinement involve division into either four or two subcells. These cases strongly resemble the the two types of ordinary refinement in the two-dimensional situation, with the addition of the fourth node which is not involved in refinement. The ordinary refinement cases are shown on the left of figure 3.8. The three cases of special refinement are also similar in principle to that which is applied to the triangles, and are shown on the right of figure 3.8.

An important difference between the refinement of triangles and that of tetrahedra is in relation to new edges that are created inside the elements during refinement. These edges are shown as dashed lines in figures 3.7 and 3.8. In the refinement of a triangle, the new edges that separate the subtriangles lie entirely within the original triangle. In the refinement of a tetrahedron, some of the new edges lie on the faces of tetrahedron, while others are entirely within the original tetrahedron. The edges that are on the faces are shared with the subcells that result when a neighboring tetrahedron undergoes refinement. Therefore, special care must be taken that these edges can be correctly associated with both sets of cells. This necessitates the existence of a set of pointers that identify a cell's neighbors.

3.7.6 Connectivity Requirements

The adaptive refinement procedure requires a large amount of connectivity information that is not relevant to the flow solver. As mentioned in section 3.6, a general tetrahedral mesh with N_P nodes will have about $N_C = 6N_P$ cells. In addition, it will have about $N_E = 7N_P$ edges. The adaptation procedure requires the nodes, edges, and neighboring cells of each cell, and the nodes of each edge. In addition, the algorithm

pointer	per object	objects	total
cell to node	4	$6N_P$	$24N_P$
cell to cell	4	$6N_P$	$24N_P$
cell to edge	6	$6N_P$	$36N_P$
edge to node	2	$7N_P$	$14N_P$
pointer subtotal			$98N_P$
other node storage	5	N_P	$5N_P$
other cell storage	3	$6N_P$	$18N_P$
other edge storage	2	$7N_P$	$14N_P$
total			$135N_P$

Table 3.3: Memory usage for adaptive refinement procedure

keeps track of the new node and new edge formed when an edge is bisected. There is also a list of three pointers per cell which are used to handle unusual cell refinement. Also, the adaptation parameter and adaptation indicator are stored at each node, as well as the node coordinates. In total, the adaptation procedure requires $135N_P$ words of storage.

Chapter 4

Results and Discussion

> So far as the theory agrees with reality, it is not exact; and so far as it is exact, it does not agree with reality.
>
> Albert Einstein

In this chapter, steady and unsteady flow solutions are presented and discussed. Comparison is made with the experimental data in the form of Jarrah's normal force measurements [32], and Hummel's measurements of pitching moment and vortex breakdown location [29]. Ten stationary wing flow solutions span the range of angle of attack from zero to 52 degrees. In this range, the flow varies from a completely intact vortex to vortex breakdown almost at the apex of the wing. A series of pitching wing calculations were performed, involving the sinusoidal variation of angle of attack from 32 degrees to 37 degrees, and back down to the original value. During the pitching motion, the position of breakdown remains above the wing, varying by about one third of root chord. An explanation will also be advanced for the jagged appearance of the contour plots presented in this chapter.

4.1 Data Interpolation on a Mesh of Tetrahedra

This section addresses the jagged appearance of the contour plots presented in section 4.3.2. In the context of this thesis, this discussion pertains only to the interpolation of a solution in post-processing, and does not make any implications towards

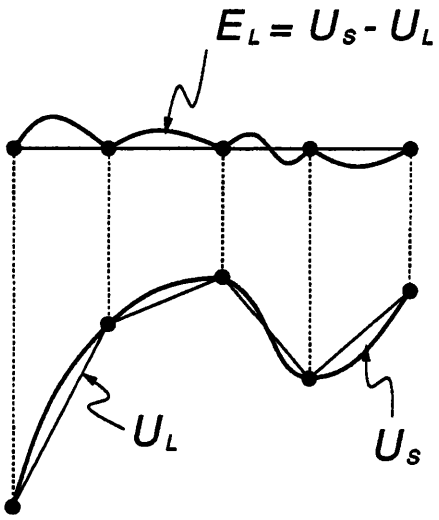

Figure 4.1: Smooth and linear interpolation in one dimension, and linear interpolation error.

the accuracy of the solutions on the basis of unaesthetic contour plots. Because of the interpolation issue, care must be taken in analysis of interpolated data. This is seen in section 4.3.2.1, in the discussion of the total pressure coefficient at the center of the vortex. There is also no effect on global quantities such as the coefficients of normal force and pitching moment.

The finite element method specifies an interpolation procedure that sets the value of a quantity at any point in the solution domain in terms of a fixed number of data points. In this thesis, data is linearly interpolated between the four corners of the tetrahedron that the point is within. As mentioned in section 3.2.2, the interpolated flow field thus produced is not an exact solution to the Euler equations everywhere. The gradient of this interpolation function is uniform within each tetrahedron; thus, this interpolation method produces a function that is not differentiable at the boundaries between tetrahedra.

One can hypothesize another approximate solution to the Euler equations, which is "smooth," or continuously differentiable everywhere and is coincident with the numerical solution at the mesh nodes. This solution is called U_S. The smooth function is not a

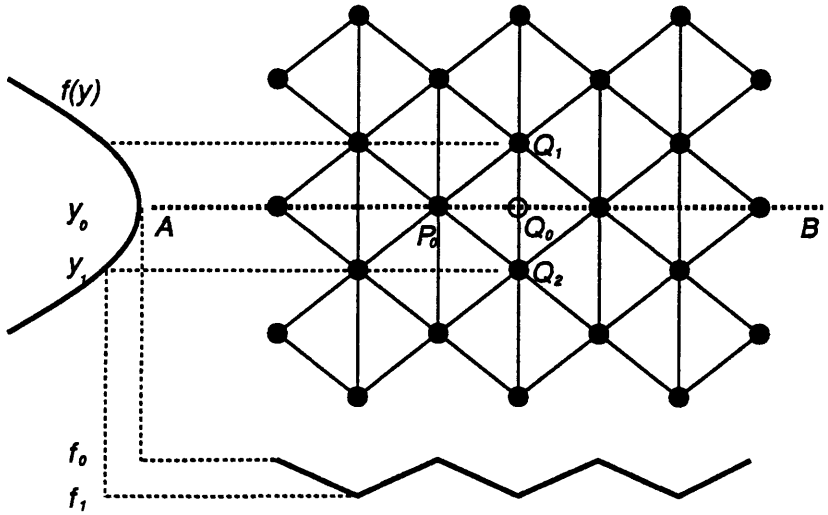

Figure 4.2: Jagged interpolation of a smooth function in two dimensions.

better solution than the linearly interpolated function, so no implications about accuracy are made. In addition, the linearly interpolated numerical solution, U_L, is taken to be the first term in a Taylor expansion of the smooth solution. The difference between the numerical solution and the smooth solution represents the numerical solution's departure from smoothness. This error function, E_L, vanishes at the mesh nodes, and elsewhere increases with distance from mesh nodes and with the second derivative of the smooth solution. Figure 4.1 represents this situation in one dimension.

The significance of this error function can be demonstrated in two dimensions with reference to figure 4.2. Consider a function $f(x,y) = f(y) \approx f_0 - ay^2$, with high curvature and variation only in the vertical direction, as shown towards the left. This function is represented at the nodes of the triangular mesh shown, and is to be interpolated onto the horizontal line segment $\overline{AB}$, at which the slope vanishes. The line segment alternately intersects the mesh at nodes, such as at point P_0, and at the midpoints of edges, such as at point Q_0. At the point P_0, the function has its maximum value of f_0. At the point Q_0, the function is interpolated between the two nodes at Q_1 and Q_2, at which the function has the value f_1, which is lower than f_0 by the amount ay_1^2. The interpolation along the line $\overline{AB}$ alternates between points such as P_0 and points such as Q_0,

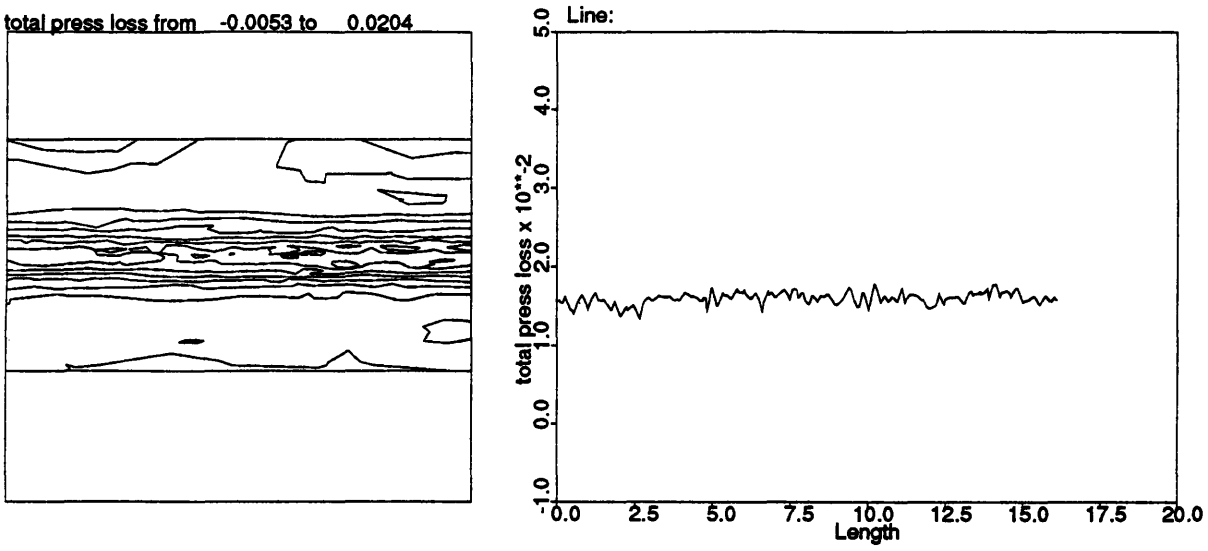

Figure 4.3: Total pressure loss in a Lamb vortex: interpolation of the analytic solution.

with the result that the interpolated function varies between the values f_0 and f_1. The magnitude of the variation depends directly on the curvature of the function f normal to the line $\overline{AB}$, and with the square of the mesh spacing. This is a consequence of the misalignment between the characteristic directions of the mesh and of the function.

This behavior is almost a certainty when using a three-dimensional tetrahedral mesh, as such meshes tend to be irregular, having no characteristic direction. As an example, figure 4.3 shows the interpolation of the analytic solution of the total pressure loss in a Lamb vortex. On the left is a contour plot of the interpolation of the three-dimensional data onto a plane through the vortex core. If the interpolation were perfect, the contour lines would be precisely horizontal. On the right is the interpolation of the planar data onto the line segment through the vortex core. At the core, the curvature of the total pressure loss is very high, and the slope vanishes, as in the two-dimensional example of figure 4.2.

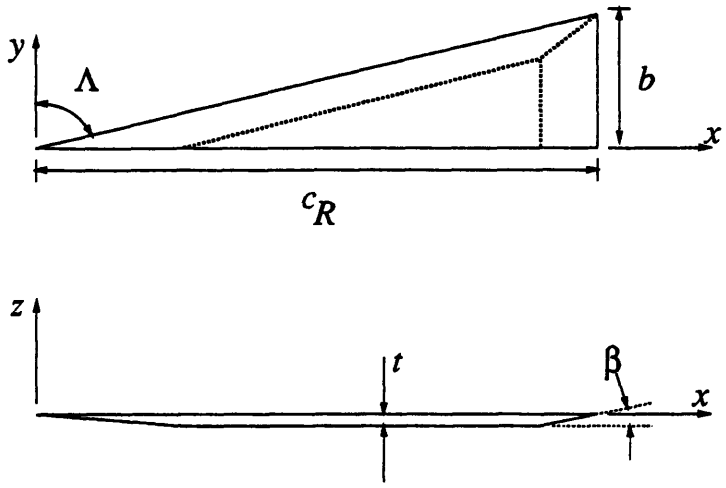

Figure 4.4: Delta wing geometry.

4.2 Delta Wing Geometry

The geometry of the delta wing used in this thesis is shown in figure 4.4. Since the angle of yaw is zero, the flow is expected to be symmetric, so the calculation is performed using only the right-hand side of the wing, with a symmetry condition at the center plane. The figure shows the wing root chord, c_R, wing span, b, sweepback angle, Λ, thickness, t, and bevel angle, β, and the coordinate system, which has its origin at the apex of the wing. The sweepback angle is 75 degrees, giving the wing and aspect ratio of 1.07. The ratio of thickness to chord, $\tau = t/c_R$, has a value of 0.016, and the bevel angle is 10 degrees. The bevel angle has the same value at the leading and trailing edges. These values were chosen to match the geometry used by Ekaterinas and Schiff [17] in their calculations. This differs from the wind tunnel model used by Jarrah [32], which has an aspect ratio of unity, and thus a sweepback angle of 76 degrees. In addition, Jarrah's wing is not beveled at the trailing edge, but the modeling of a blunt trailing edge when using an inviscid fluid model is both difficult and unnecessary.

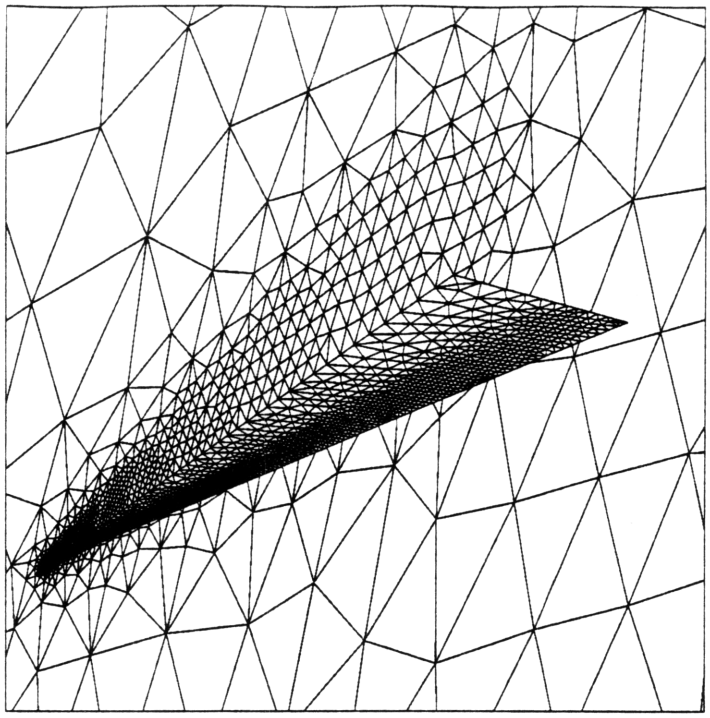

Figure 4.5: Surface triangulation of delta wing for coarse mesh.

4.3 Stationary Wing Solutions

Stationary wing solutions were performed at ten values of angle of attack, in the range of zero to 52 degrees. The angles of attack are concentrated in the high part of the range, in which vortex breakdown occurs. The free stream Mach number is $M_\infty = 0.3$ for all cases. This was chosen to match solutions obtained by Ekaterinas and Schiff [17] at angles of attack of 20.5 degrees and at 32 degrees. The coarse mesh used for all cases has 15462 nodes. All three-dimensional visualization was done using Visual3, an interactive package developed by Haimes [24]. The surface triangulation for the coarse mesh appears in figure 4.5. The apex of the wing is at the lower left, and the trailing edge is towards the upper right. Mesh node clustering is apparent at the leading edge and towards the apex of the wing. Only the left half of the wing is modeled, and the triangulation on the symmetry plane is also visible. One level of adaptive refinement was performed for all of the cases, except for the case at zero degrees angle of attack. Fluid entropy was the adaptation parameter, with the criterion that 30% of the mesh nodes be selected for adaptation. Figure 4.6 shows the effect of adaptation on the mesh density. On the left is a slice through the coarse mesh at a plane normal to the wing, located at 70% of root chord. On the right is the same slice through an adaptively

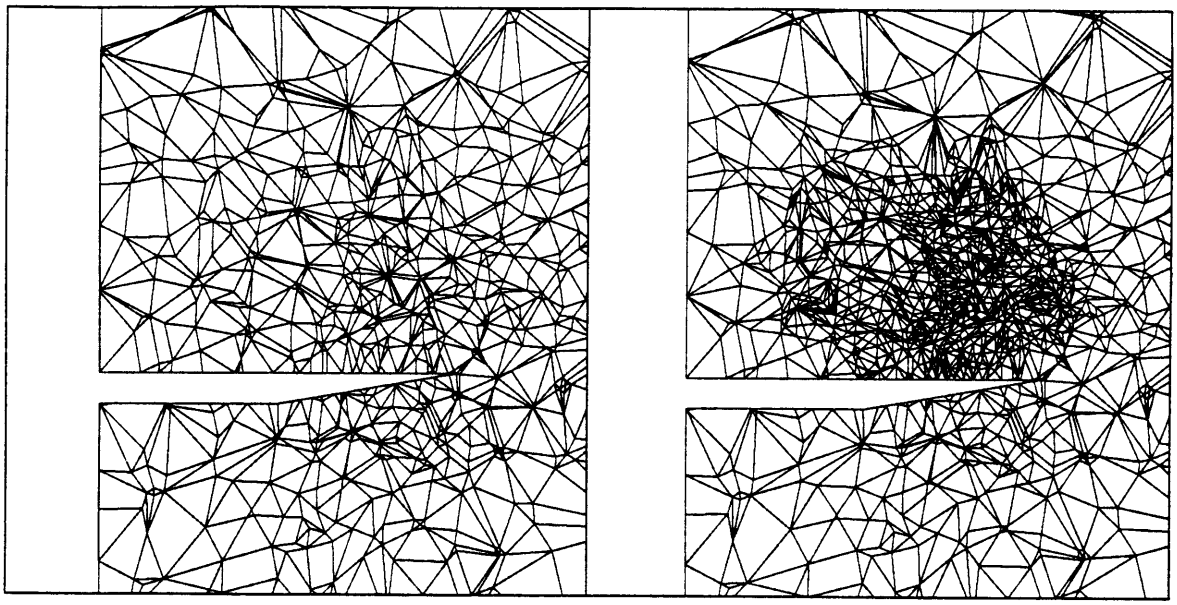

Figure 4.6: Slice through coarse and adapted meshes at 70% of root chord. Coarse mesh in on the left, adapted mesh is on the right.

	coarse mesh				adapted mesh				
α	C_N	C_L	C_D	C_M	nodes	C_N	C_L	C_D	C_M
0.0°	−0.076	−0.076	0.	0.0474					
10.0°	0.284	0.280	0.0493	−0.0142	77630	0.305	0.300	0.0530	−0.0137
	0.302	0.297	0.0524						
20.5°	0.773	0.724	0.271	−0.0649	83286	0.860	0.806	0.301	−0.0786
	0.912	0.854	0.319			0.863	0.808	0.302	
26.0°	1.132	1.018	0.496	−0.1163	81090	1.020	0.9172	0.447	−0.1061
	1.147	1.031	0.503						
30.0°	1.268	1.098	0.634		81055	1.367	1.184	0.684	−0.1265
	1.291	1.118	0.645			1.392	1.206	0.696	
32.0°	1.349	1.144	0.715	−0.1131	80194	1.493	1.266	0.791	−0.1056
						1.554	1.318	0.823	
35.0°	1.454	1.186	0.841	−0.1305	81448	1.351	1.107	0.775	−0.1003
						1.499	1.228	0.860	
38.0°	1.527	1.203	0.940	−0.1627	80652	1.321	1.041	0.813	−0.0837
	1.591	1.254	0.976			1.499	1.181	0.923	
42.0°	1.612	1.198	1.331	−0.1958	79975	1.490	1.107	0.997	−0.1577
	1.675	1.245	1.382			1.538	1.143	1.029	
52.0°	1.764	1.086	1.390	−0.2346	78369	1.207	0.730	0.951	−0.2693
	1.811	1.115	1.427			1.264	0.778	0.996	

Table 4.1: Summary of stationary wing cases.

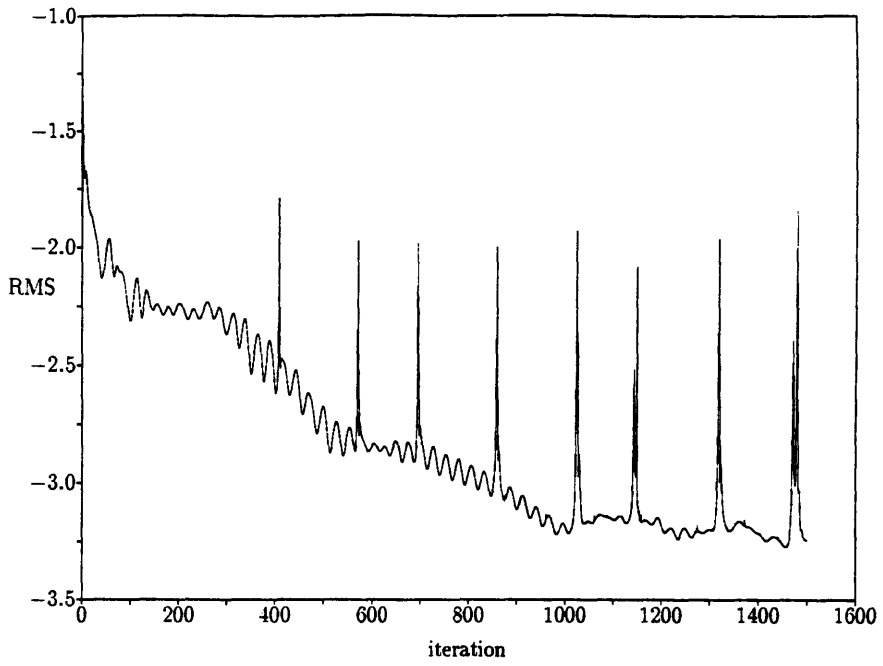

Figure 4.7: Iteration history of root mean square of state vector for $\alpha = 42°$ case.

refined mesh, for the flow around a wing at 20.5° angle of attack, which will be discussed in section 4.3.2.1. The higher mesh node density in the region of the vortex above the wing is clearly evident.

4.3.1 Analysis of Global Features of Solutions

A summary of the cases is presented in table 4.1, in which the angle of attack, number of nodes in the adapted mesh, and the aerodynamic force coefficients for each case are shown. When two values of normal force, lift and drag are presented for a single case, the solution has not attained steady state. For the cases involving vortex breakdown this is due to the inherent unsteadiness of the flow downstream of breakdown which makes a steady solution unreachable. This unsteadiness is due to the rotation of the helical vortex core, and to the periodic fluctuation of the position of breakdown. This situation is exhibited in figures 4.7 and 4.8, which show the iteration histories of the root mean square of the change in the state vector, and of the coefficient of normal force, for the case at an angle of attack of 42 degrees. The RMS quickly drops to a minimum that is much larger than machine precision, which indicates that the coarse

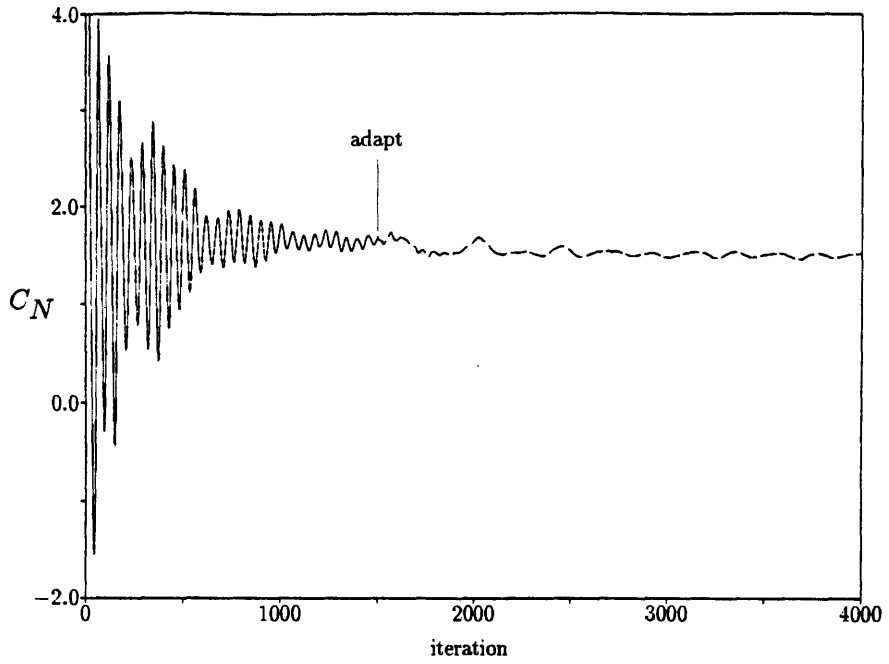

Figure 4.8: Iteration history of coefficient of normal force for $\alpha = 42°$ case.

mesh solution is not steady, and the coefficient of normal force settles into a cycle which shows no sign of diminishing. The values in table 4.1 are the minimum and maximum of the final period of oscillation.

In this thesis, the unsteadiness in the stationary wing flows will be referred to as "natural" unsteadiness, meaning that it is present in the absence of any unsteady forcing function in the governing equations. The term "natural" should *not* be interpreted to imply that the unsteadiness is of a physical, as opposed to numerical, origin. When such an implication is intended, the term "physical" shall be used. Further, the details of the unsteadiness, particularly the frequency, will be less accurate due to the use of local time steps in temporal integration (see section 3.5.1). The study of the correct time behavior of the unsteadiness will require the computation of a time accurate solution. Further details of the unsteadiness will be discussed later in this section.

Stationary wing normal force curves are presented for coarse mesh computations in figure 4.9, and for adapted mesh computations in figure 4.10. Both figures include Jarrah's wind tunnel data [32] for comparison. It is clear that the coefficient of normal force is adequately predicted using the coarse mesh at low angles of attack, in which the

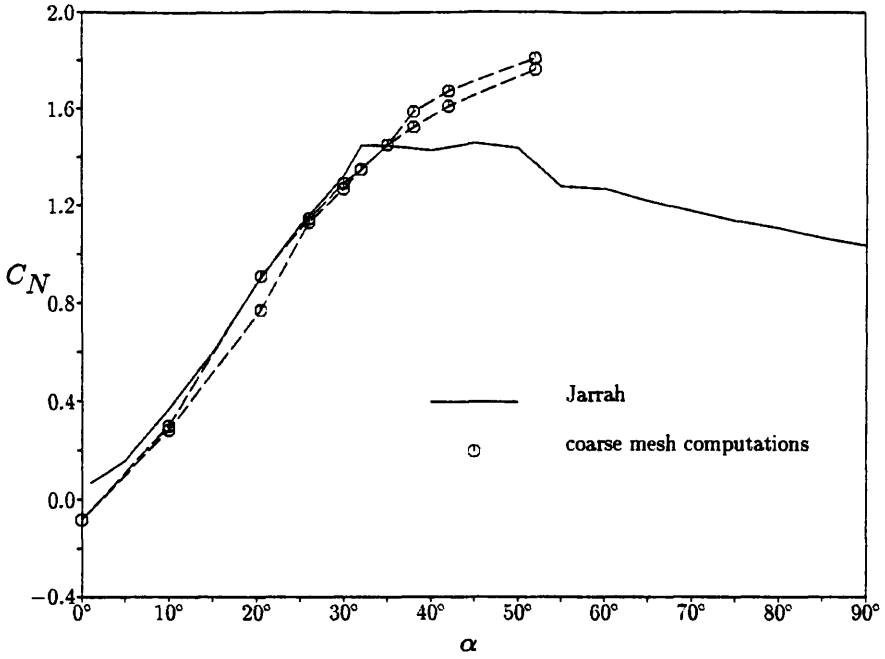

Figure 4.9: Stationary wing normal force coefficient versus angle of attack, without adaptation. Solid line is experimental data of Jarrah [32]. Symbols are computations.

vortex is intact over the entire wing. However, the coarse mesh is unable to capture the details of breakdown, at higher angles of attack, well enough to predict the occurrence of maximum lift. Figure 4.10 shows the improvement in the stationary wing normal force curve due to the use of adaptation. At all angles of attack, except for 26 degrees and 52 degrees, the computed coefficient of normal force is in excellent agreement with the wind tunnel data. The reason for the poor match at 26 and 52 degrees angle of attack will be explained in the discussion of the location of breakdown.

Stationary wing pitching moment curves appear in figures 4.11. Adapted and coarse mesh computations are represented. A nose-up moment is defined to be a positive value, and the axis about which the moments are taken is at 50 percent of the wing root chord, and the values are referenced against the moment coefficient at zero angle of attack. There was uncertainty as to the details of how Jarrah defined the pitching moment, so the numerical values are compared with data measured by Hummel and Srinivasan [29]. The agreement of the computational predictions with data is not as good as is that of the normal force data. For the range of angle of attack for which Hummel and Srinivasan presented data, the numerical values of the pitching moment coefficient are consistently 25 percent higher than the experimental values. As large as

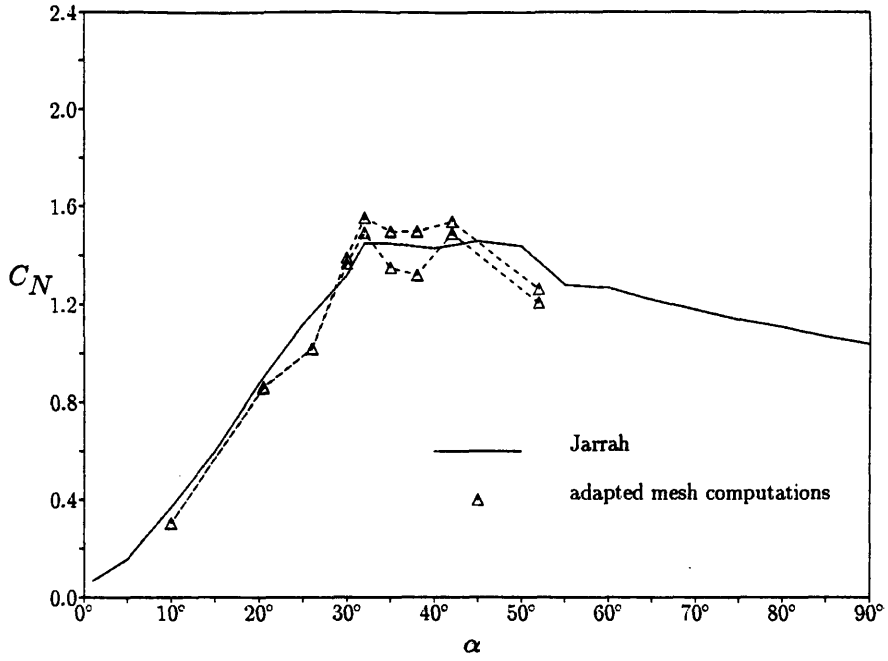

Figure 4.10: Stationary wing normal force coefficient versus angle of attack, with adaptation. Solid line is experimental data of Jarrah [32]. Symbols are computations.

this difference seems, it can be accounted for by a chordwise error in the location of the moment reference axis of one percent of root chord. In the case of Hummel and Srinivasan's experiments, this distance is less than a centimeter. Additional calculations were performed to investigate the history of the pitching moment coefficient during the calculation. An example is seen in figure 4.12, which shows the history of the pitching moment coefficient for the flow past the wing at 32 degrees angle of attack, as computed on a coarse mesh. Fluctuations of ten to fifteen percent of the mean value are observed, which may account for some of the difference between the numerical and the experimental values, but should not result in a consistent trend. The pitching moment is also very sensitive to details of the flow at the trailing edge, since the span of the wing and the moment arm are both large there. The behavior of the numerical values at very high angles of attack is consistent with the trends observed by Hummel and Srinivasan for wings of higher aspect ratio, for which vortex breakdown occurs at a lower angle of attack.

The variation of vortex breakdown location with angle of attack is shown in figure 4.13. Experimental data gathered by Hummel and Srinivasan are also shown in this figure, for comparison. The apex of the wing is at the top of the figure, and the trail-

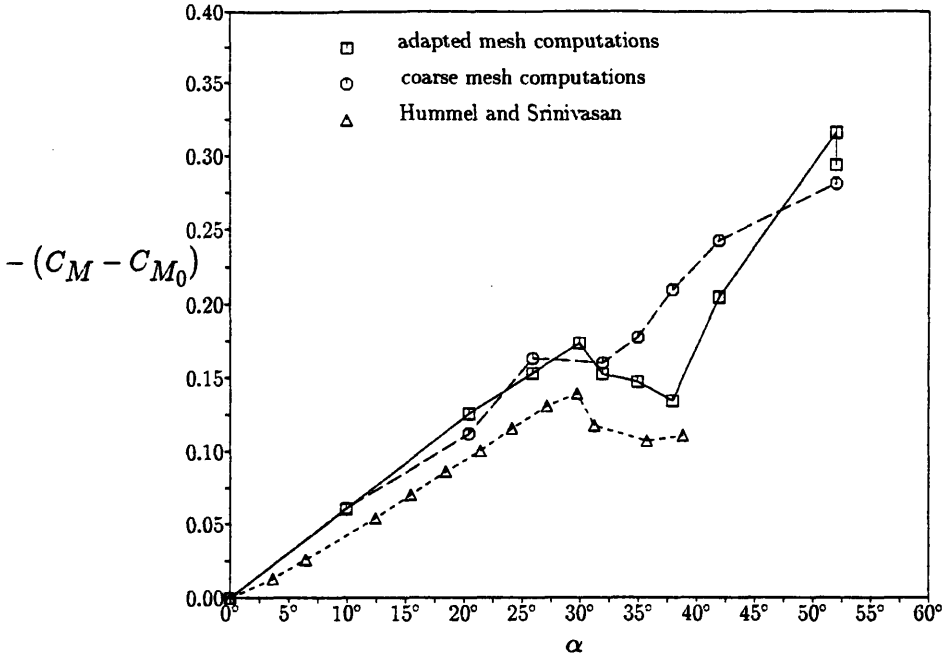

Figure 4.11: Stationary wing pitching moment coefficient versus angle of attack. Solid line is adapted mesh computations, dashed line is coarse mesh computations, dotted line is experimental data of Hummel and Srinivasan [29].

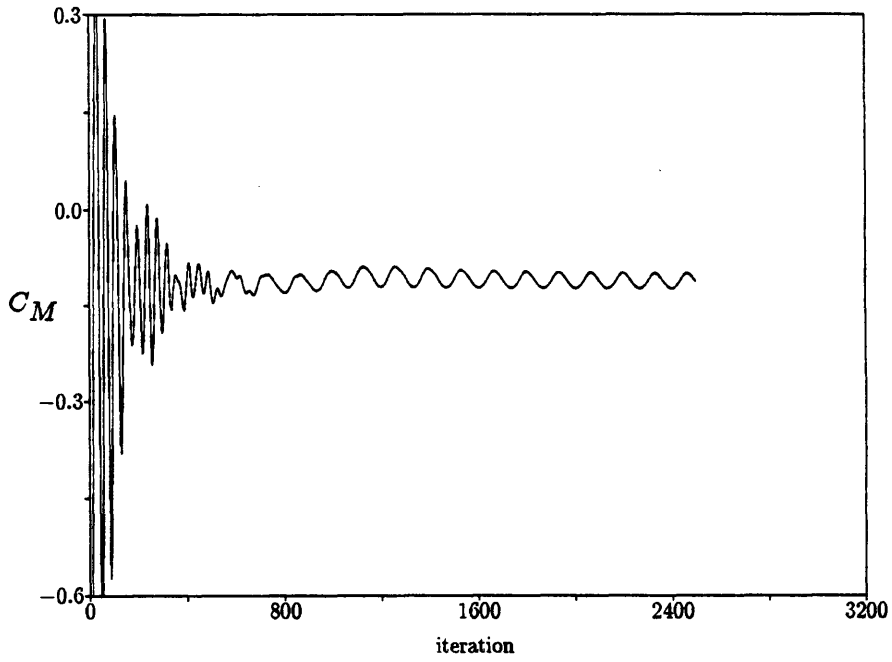

Figure 4.12: Iteration history of coefficient of pitching moment for $\alpha = 32°$ case.

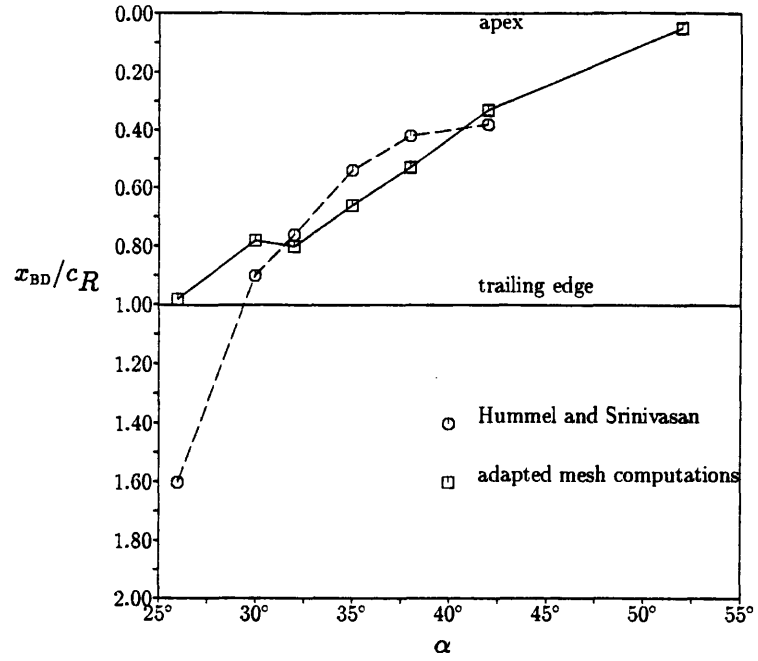

Figure 4.13: Vortex breakdown location versus angle of attack. Solid line is adapted mesh computations, dotted line is experimental data of Hummel and Srinivasan [29].

ing edge is in the middle. The computed breakdown location is determined as follows. Using interactive visualization software, the core of the intact vortex is located, and the component of velocity in the direction of the vortex axis is computed. Since one of the characteristic features of vortex breakdown is the stagnation of the flow, followed by a region of reverse flow, breakdown is said to occur in the numerical solution at the location at which the axial velocity first becomes zero.

Figure 4.13 shows reasonable agreement between the computational and experimental measurements of breakdown location, with the exception of the data at 26 degrees angle of attack. At this angle of attack, the experimental data indicates that breakdown occurs in the wake, far downstream of the wing. In the numerical solution, however, breakdown occurs slightly forward of the trailing edge of the wing. An explanation for this mismatch involves the resolution of the mesh in the wake. The computational meshes were generated with a higher resolution above the wing than in the wake, in order to decrease the mesh size to economize on memory storage. Since the normal force coefficient data in figures 4.9 and 4.10 show that the features of vortex breakdown are not accurately computed with the resolution of the coarse mesh, it is possible that similar inaccuracy will occur if breakdown attempts to occur in the less well resolved

portions of the mesh, namely the wake. It is as if the inadequate resolution in the wake does not allow breakdown to occur, so breakdown is pushed forward to the finer regions of the mesh. In addition, the streamwise gradients of circulation and pressure are smaller in the wake than over the wing. Both of these gradients are important in the physical process of vortex breakdown [14], and their variation over the wing may help define the position of breakdown more precisely. An additional solution was performed on a different mesh to investigate the effect of mesh resolution in the wake on the breakdown position. The solution showed that finer resolution did allow breakdown to occur in the wake, although far forward of the experimentally measured location. The breakdown position moved very slowly rearwards, and it is estimated that 5000 additional iterations would be needed for the breakdown position to reach the experimental position at the propagation speed seen in the calculations.

The predictive errors at 52 degrees angle of attack can also be explained by the location of vortex breakdown. The numerical solution predicts that breakdown occurs very far upstream, almost at the nose of the wing. Upstream of breakdown, the mesh spacing is too coarse to satisfactorily resolve the intact vortex, so that this flow cannot expect to be as accurate as those at lower angles of attack in which the intact vortex is well represented.

The other cases, in which breakdown occurs over the wing, show fairly good agreement with the breakdown locations measured by Hummel and Srinivasan. There are three possible explanations for the differences between the numerical and experimental breakdown locations. First, the difference may be due to a different criterion used to define breakdown location. Figure 4.14 shows schematically the detail of the region of vortex breakdown. The flow enters from the left, with the vortex core shaded as if it is marked with smoke or dye, as is typically done in flow visualization experiments. The region of reversed flow is to the right, and the fluid in the core is diverted around the bubble. The locations x_1 and x_2 locate two characteristic features of vortex breakdown. The rapid expansion of the vortex core, which is easily identifiable in the wind tunnel by smoke or dye visualization, occurs at x_1. The onset of reverse flow, which is easily

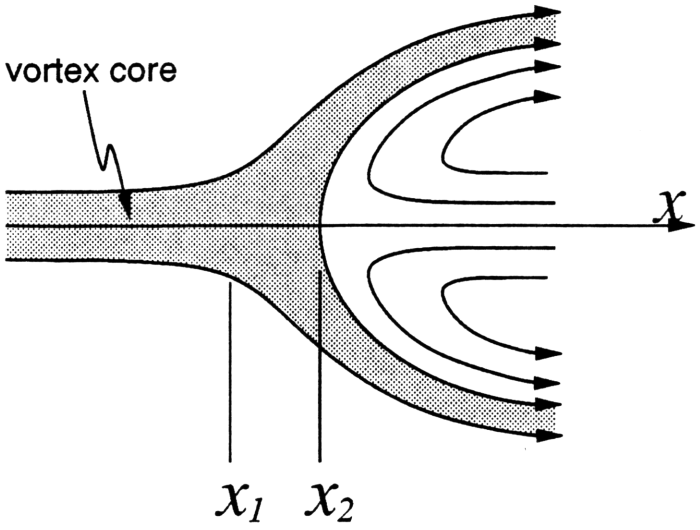

Figure 4.14: Detail of the region of vortex breakdown, showing two criteria for breakdown location.

identifiable numerically by examination of the axial velocity, occurs at the stagnation point at x_2. Thus, it is likely that the numerical determination of the vortex breakdown location will be slightly aft of the experimental determination.

A second explanation for the difference is that there can be an uncertainty in the experimentally determined vortex breakdown location, if the breakdown region is large or poorly defined. This problem is discussed in more detail by Thompson, Batill, and Nelson [81]. However, it is impossible to evaluate the importance of this problem without access to very detailed flow visualization data from which experimental researchers determined vortex breakdown location.

Although there is a trend of the numerically predicted vortex breakdown location being slightly aft of the locations measured by Hummel and Srinivasan, the trend is not strong enough for the disagreement between experimental and numerical data to be completely explained only by the difference in measurement of vortex breakdown location. The trend is also more pronounced at higher angles of attack, at which the breakdown location is closer to the apex, whereas at lower angles of attack, at which the breakdown location is closer to the trailing edge, there is a weak tendency for the

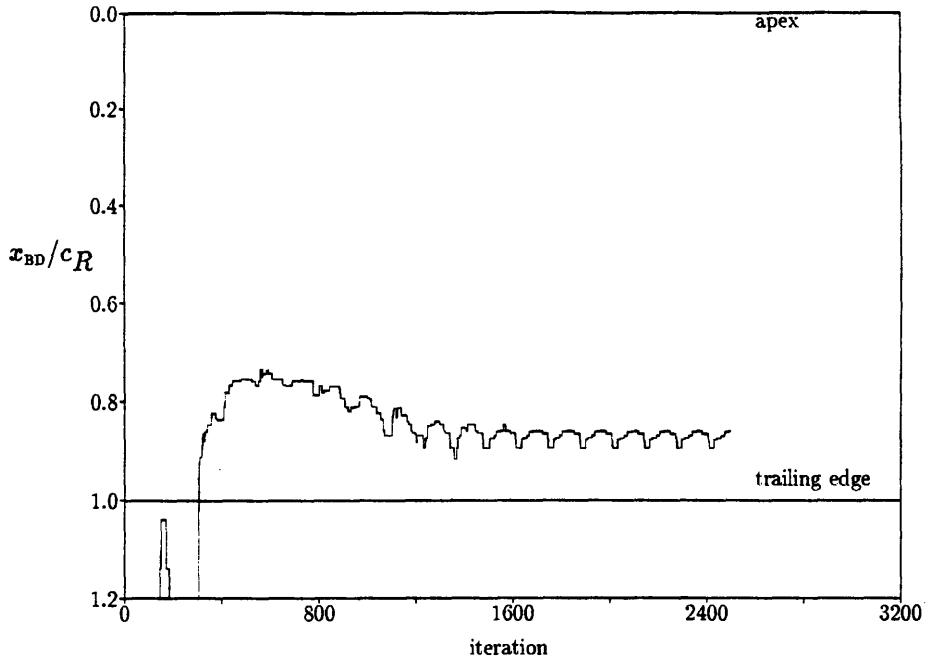

Figure 4.15: Iteration history of vortex breakdown position for $\alpha = 32°$ case.

numerically predicted breakdown location to be forward of the experimentally measure breakdown location. The effect is that the rate at which breakdown moves forward with increasing angle of attack is lower in the numerical simulation than in the experiment. This difference in rate can also be observed in the computations of Agrawal, Barnett and Robinson [1]. In addition, the differences between the coarse mesh solutions and the adapted mesh solutions indicate that the adapted mesh solutions are not mesh converged. Thus, errors due to inadequate mesh resolution could also be present.

A third source of the difference in vortex breakdown location is that the vortex breakdown location fluctuates, due to the inherent unsteadiness of the flow. The chordwise "meandering" of vortex breakdown has also been observed in wind tunnel experiments [69]. Figure 4.15 shows the iteration history of the vortex breakdown position for the wing at an angle of attack of 32 degrees, using a coarse mesh. A periodic fluctuation is present, having the same frequency as the variation in normal force coefficient and pitching moment coefficient, and an amplitude of about 3 percent of wing root chord. Wind tunnel measurements of breakdown location are likely to represent a time-average of the unsteady breakdown location, whereas the numerically determined breakdown location will be the instantaneous breakdown location at the iteration at

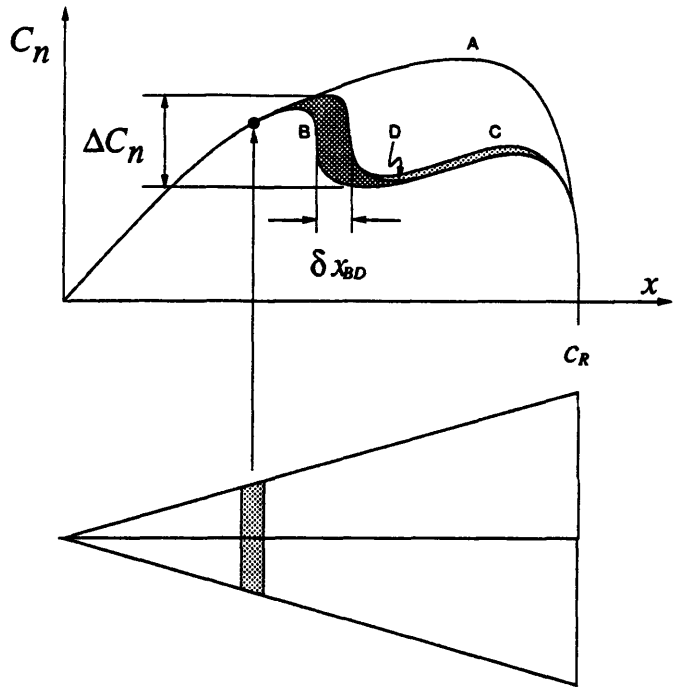

Figure 4.16: Change of normal force to to motion of vortex breakdown.

which post-processing is performed.

The fluctuation of the vortex breakdown position is only one source of unsteadiness. Downstream of breakdown, the helical vortex core rotates about the axis of the intact vortex, at a rate believed to vary with chordwise position [71]. The relative importance of the two sources of unsteadiness can be estimated by use of a relation between the amplitude of the fluctuations of the breakdown position and the fluctuations of the normal force on the wing. First, consider the quantity

$$C_n(x) = \frac{1}{b} \int_{-s(x)}^{s(x)} c_p \, dy \tag{4.1}$$

which represents the contribution to the normal force at a selected chordwise location. The local semi-span of the wing is $s(x)$. The total normal force coefficient for the wing is then

$$C_N = \frac{2}{c_R} \int_0^{c_R} C_n(x) \, dx. \tag{4.2}$$

Figure 4.16 schematically shows possible chordwise variations of $C_n(x)$. Four curves are shown, to represent four flow situations. The total normal force for each situation is proportional to the area under the appropriate C_n curve.

Curve A represents that variation in the absence of vortex bursting. The behavior is roughly linear near the apex, then the rate of increase declines due to the adverse pressure gradient above the wing, and then drops to zero due to the unloading of the wing at the trailing edge. The other curves represent the variation of $C_n(x)$ in the presence of vortex breakdown, at the same angle of attack. Consider curve B. Far upstream of breakdown, the behavior is the same as if the vortex were intact. At the location of breakdown, the pressure above the wing suddenly increases due to the disappearance of the concentrated vortex, resulting in a decrease ΔC_n in the contribution to lift. Then, the contribution to lift increases gently, due to the increasing span of the wing. Curve C represents the behavior in a situation in which breakdown occurs a small distance δx_{BD} downstream of where it occurs in curve B. It is assumed that the chordwise lift will drop by the same amount ΔC_n as in curve B. The difference in normal force, δC_N, due to the change in breakdown location is proportional to the area between curves B and C, shaded gray in figure 4.16 . Curve D represents a flow in which the vortex breaks down at the same location as in curve C, but the behavior of $C_n(x)$ downstream of breakdown is the same as in curve B. The difference in normal force between curves B and D is proportional to the area shaded dark gray, which should be larger than the light gray area due to the low slope of the curves C and D downstream of breakdown.

The dark gray area is further approximated as a rectangle, of width δx_{BD} and height ΔC_n, so that the change in the normal force associated with a change in breakdown location is roughly

$$\delta C_N \approx 2\, \Delta C_n \frac{\delta x_{\mathrm{BD}}}{c_R}. \tag{4.3}$$

The actual fluctuation of the normal force coefficient is determined from figure 4.10 to be about 0.1. It is more difficult to determine ΔC_n. Based upon the behavior of C_n at 38° angle of attack, as shown in figure 4.17, one can estimate ΔC_n to be as large as 0.5, while figure 4.15 shows a fluctuation in breakdown position of about 3 percent of root chord. This reveals that the fluctuation of the breakdown position is associated with a fluctuation of the normal force coefficient of 0.03, which is much smaller that that which is seen.

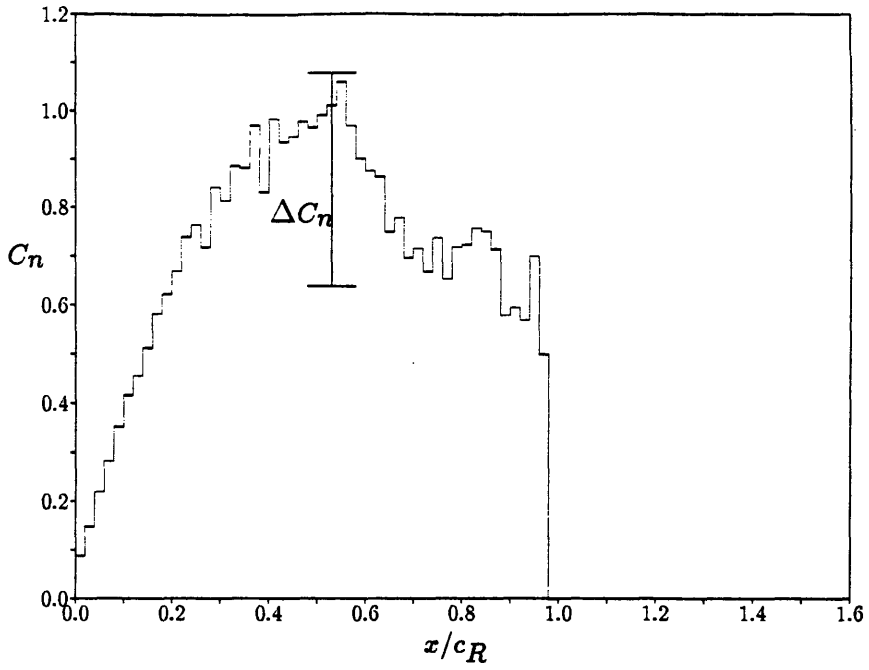

Figure 4.17: Variation of local lift with axial position, at $\alpha = 38°$.

An estimation of the frequency of the fluctuations can be used to assess the importance of the rotation of the helical vortex core. It is important to note that the use of local time steps prevents the solutions from being time accurate, so that the following analysis may not have any relevance to the physical phenomenon of vortex breakdown. Nevertheless, it will help in understanding the numerical simulation.

A reduced frequency can be estimated for the fluctuations of the type seen in figures 4.12 and 4.15. It is necessary to determine an average time step throughout the region downstream of breakdown. Because of the time step averaging procedure, the reduced frequency is fairly inaccurate. This yields an estimated reduced frequency in the range $k = 0.8 - 1.3$. In addition, it is posible to estimate a reduced frequency specifically associated with the rotation of the helical vortex core. This is done by examining the chordwise distance, or pitch, X, between sucessive turns of the spiral. The frequency of the fluctuation is related to the pitch and to the downstream convection speed, U, as $\Omega = U/X$. If the convection speed is taken to be the speed of the free stream, then the reduced frequency associated with the spiral vortex can be estimated to be in the range $k = 1.2 - 2$. This is close enough to the reduced frequency estimated from the iteration histories to suggest that the unsteadiness is primarily associated with motion

of the spiral vortex downstream of breakdown.

4.3.2 Analysis of Individual Cases

Three solutions will be discussed in detail. All cases are at a free stream Mach number of 0.3. A solution at an angle of attack of 20.5 degrees features an intact vortex, and is compared with a solution obtained by Ekaterinas and Schiff at the same conditions. A solution at an angle of attack of 32 degrees features vortex breakdown over the aft part of the wing, and is compared with another solution obtained by Ekaterinas and Schiff. The third solution is at an angle of attack of 42 degrees, at which breakdown occurs over the forward part of the wing.

4.3.2.1 Intact vortex at 20.5 degrees angle of attack.

The first case to be described in detail is at 20.5 degrees angle of attack, a condition at which the vortex remains intact throughout the flow. A comparison is made with the flow computed by Ekaterinas and Schiff [17], who used a Navier-Stokes flow solver with a structured grid of approximately 100,000 grid points that are not in the boundary layer. Due to their modeling of viscous terms, Ekaterinas and Schiff's solution captures the behavior of the secondary vortex, which is caused by boundary layer separation on the lee side of the wing, underneath the primary vortex. The secondary vortex is a feature that does not appear in any flows calculated using the solver described in this thesis.

Figure 4.18 shows contours of pressure on the upper surface of the wing. The region of low pressure in the area of the wing underneath the vortex core is clearly visible. The pressure is lowest towards the apex, and gradually increases towards the free stream pressure downstream, as the core moves further from the surface of the wing. This adverse pressure gradient is responsible for vortex breakdown, in the cases in which it

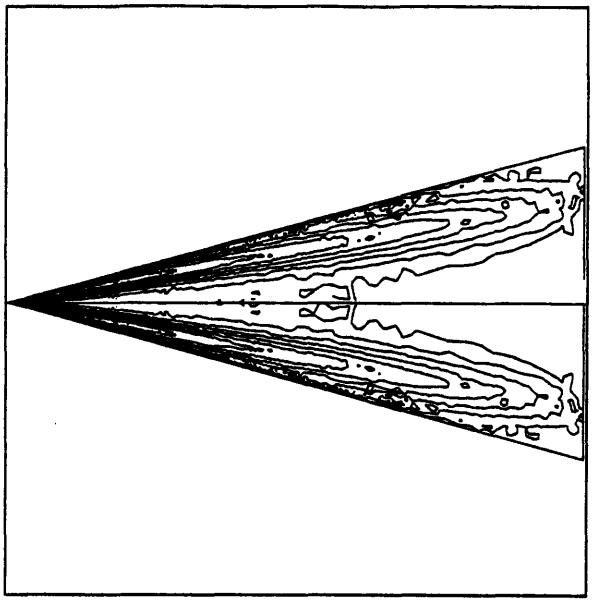

Figure 4.18: Pressure on the upper surface of the wing, at $\alpha = 20.5°$, on adapted mesh. Contour increment is 0.05, outermost contour value is 0.70.

occurs.

Figure 4.19 shows contours of density in the plane normal to the wing at 90% of root chord. The coarse mesh solution is on the left, and the adapted mesh solution is on the right. The coarse mesh solution is very jagged, due to the interpolation issue discussed in section 4.1. These plots can be compared with the density as computed by Ekaterinas and Schiff, which is shown in figure 4.20. The coarse mesh solution does not compare well with Ekaterinas and Schiff's solution, although the position of the vortex core is adequately predicted. In the coarse mesh solution, the core is located at 0.67 of local semi-span outboard of the centerline, and 0.33 of semi-span above the wing, which compares to values of 0.65 and 0.32 as predicted by Ekaterinas and Schiff. The adapted solution compares more favorably with Ekaterinas and Schiff's solution, and predicts the center of the vortex to be at 0.69 and 0.33. The differences between the three vortex center locations are on the order of the local mesh spacing in the vortex core, and therefore are not highly significant. For comparison, Goodsell, who solved the Euler equations using a structured grid [22], predicted the vortex location to be 0.73 of semi-span from the centerline and 0.32 of semi-span above the wing, and Verhaagen and Kruisbrink [85] measured the vortex center to be at 0.68 of semi-span from the

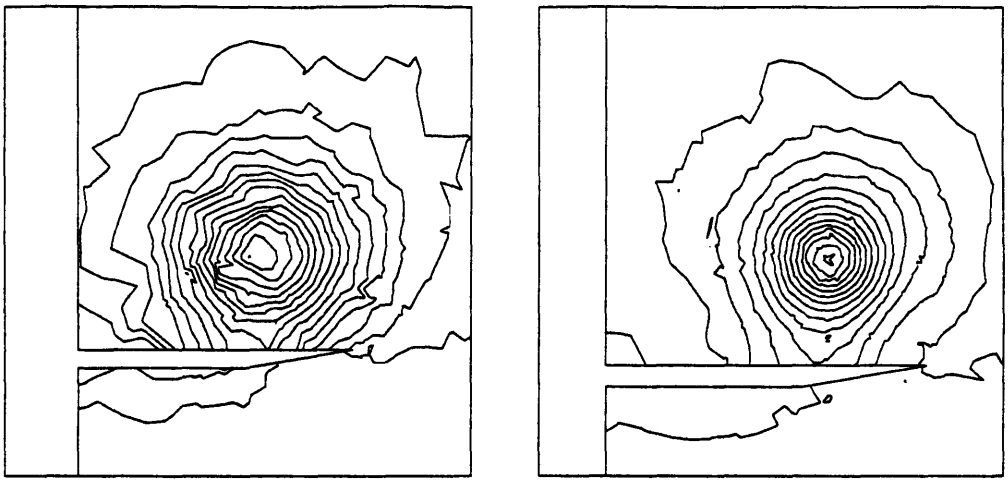

Figure 4.19: Computed density variation at $x/c_R = 0.90$, for $\alpha = 20.5°$. Left: coarse mesh, right: adapted mesh. Contour increment is 0.005, innermost contour values are 0.930 (coarse) and 0.855 (adapted).

centerline and 0.36 of semi-span above the wing.

The density at the center of the vortex varies widely, having a value of 0.926 in the coarse mesh solution, a value of 0.859 in the adapted mesh solution, and a value of 0.902 in Ekaterinas and Schiff's solution. This is due to the effect of viscosity on the structure of the subcore. As the viscosity of the fluid decreases, the size of the subcore decreases. The maximum swirl velocity, which occurs at the edge of the subcore, remains at about the same value, which is on the order of the free stream velocity. This results in a strong centrifugal pressure gradient in the subcore, which will force fluid outwards and drive the conditions at the axis towards vacuum. This is the cause of the extremely low pressure typically measured at the vortex axis, and also of the high axial velocity, which maintains mass flow in the presence of low densities. Typical values are a minimum pressure coefficient of $c_p = -10$ and an axial velocity ratio of $u/q_\infty = 3$ [84]. This issue is discussed in detail by Meyer and Powell [52], in their analysis of similarity solutions for the flow in the vortex core. Since the flows computed for this thesis use an inviscid model, the effect of viscosity is felt only through the artificial dissipation. The dissipation operator is constructed in such a way that its magnitude decreases with

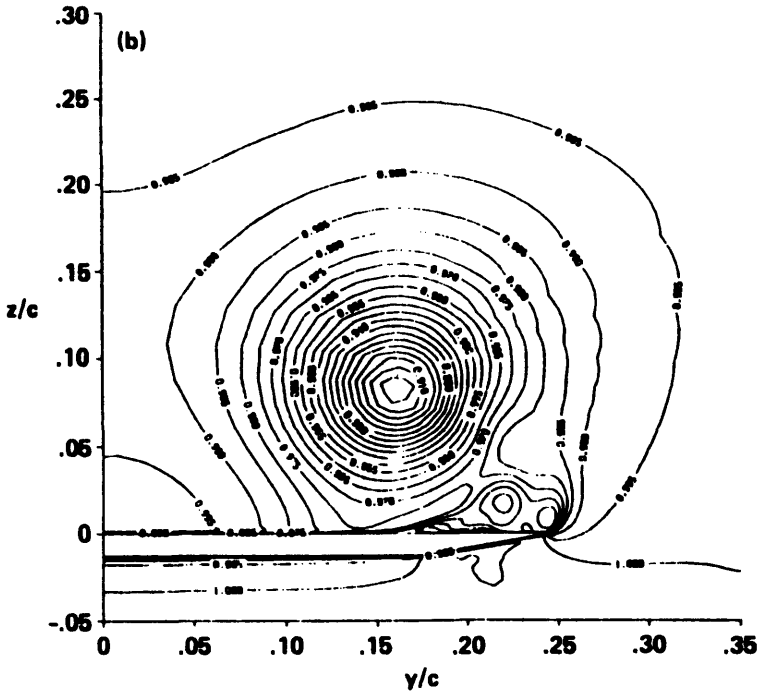

Figure 4.20: Density variation at $x/c_R = 0.90$, for $\alpha = 20.5°$, from Ekaterinas and Schiff [17].

decreasing mesh spacing, so that the adapted mesh solution appears less viscous than the coarse mesh solution, resulting in a more slender subcore and a greater tendency towards vacuum at the axis.

The structure of the vortex is more readily seen by examining the entropy, or the total pressure loss. Figure 4.21 shows the entropy in a plane normal to the wing at 70% of the root chord, for the coarse mesh solution. The feeding sheet is not well resolved, and the vortex itself infringes upon the wing surface, which indicates that the vortex is not well resolved. This solution has about five to ten cells across the vortex core. The adaptation criterion was determined with the help of this plot. A level of entropy was chosen that would select the entire vortex for adaptation. This results in 30% of the nodes of the mesh being selected for adaptation. The fraction of the cells that will be refined is similar. Since refinement of a cell produces eleven new cells, this will result in an approximate quadrupling of the mesh size.

Figure 4.22 shows the improvement in the resolution of the vortex in the adapted solution. The vortex core is smaller in size, and does not touch the wing surface anywhere. Since the core is smaller, the number of cells across the vortex core is not doubled, even

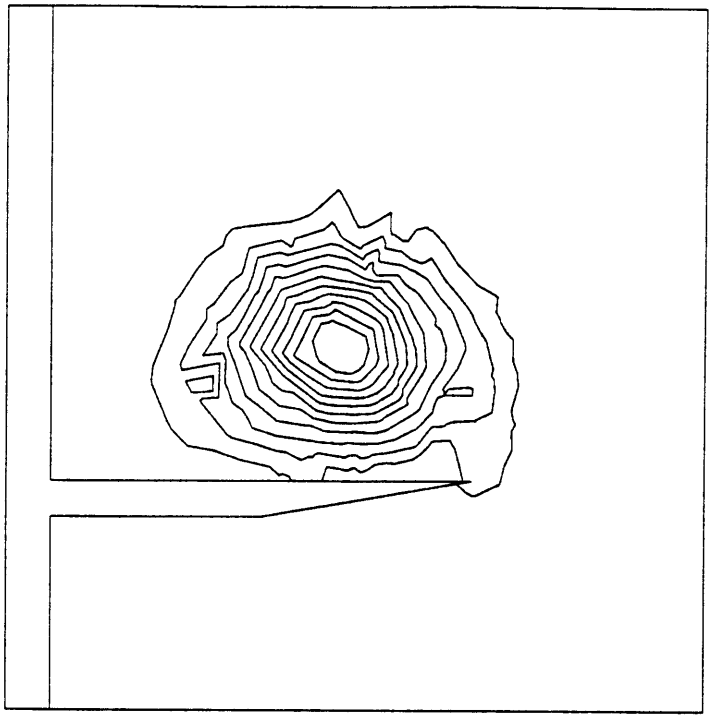

Figure 4.21: Computed entropy variation on coarse mesh at $x/c_R = 0.70$, for $\alpha = 20.5°$. Contour increment is 0.002, innermost contour value is 0.022.

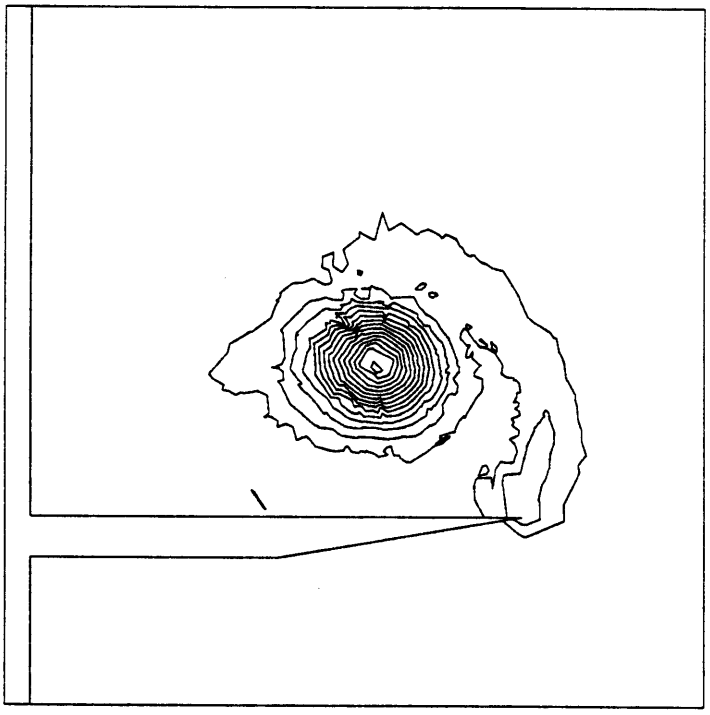

Figure 4.22: Computed entropy variation on adapted mesh at $x/c_R = 0.70$, for $\alpha = 20.5°$. Contour increment is 0.002, innermost contour value is 0.030.

though the mesh spacing is halved. In addition, the feeding sheet is well resolved. However, the resolution is insufficient to resolve the viscous sheath, which separates the inviscid irrotational outer flow from the essentially invisvid rotational flow in the outer vortex core [42].

Few researchers present entropy, so comparison with other solutions are made in terms of total pressure, which is related to entropy through the second law of thermodynamics. The total pressure is commonly expressed as the total pressure loss, defined as

$$\Delta p_0 = 1 - \frac{p_0}{p_{0\infty}}, \tag{4.4}$$

or by the total pressure coefficient, defined as

$$c_{p_0} = \frac{p_0 - p_\infty}{\frac{1}{2}\rho_\infty q_\infty^2}. \tag{4.5}$$

For low Mach number flow, the two quantities are related by

$$\Delta p_0 = \tfrac{1}{2}\gamma M_\infty^2 (1 - c_{p_0}) + \mathcal{O}(M_\infty^4). \tag{4.6}$$

The total pressure coefficient is roughly independent of Mach number at low Mach number [22], so valid comparisons can be made with calculations and experiments performed at other Mach numbers. Since total pressure is constant along particle paths in the absence of viscous losses, it can be measured at any chordwise location at the axis. Figure 4.23 demonstrates that the total pressure coefficient does not vary strongly along the vortex axis in the adapted mesh solution. It also shows a noticeable interpolation error, as discussed in section 4.1. In order to obtain a more accurate value of the total pressure coefficient, one should choose a high value from figure 4.23, which results in a value of -0.84. Applying a similar procedure to the coarse mesh solution yields a minimum total pressure coefficient of -0.49. These values can be compared with Goodsell's value of -0.60, and with Verhaagen and Kruisbrink's equivalent value of -2.8. Goodsell's result is typical of other solutions obtained using the Euler equations. The disparity between the computed value and the measured value of the total pressure co-

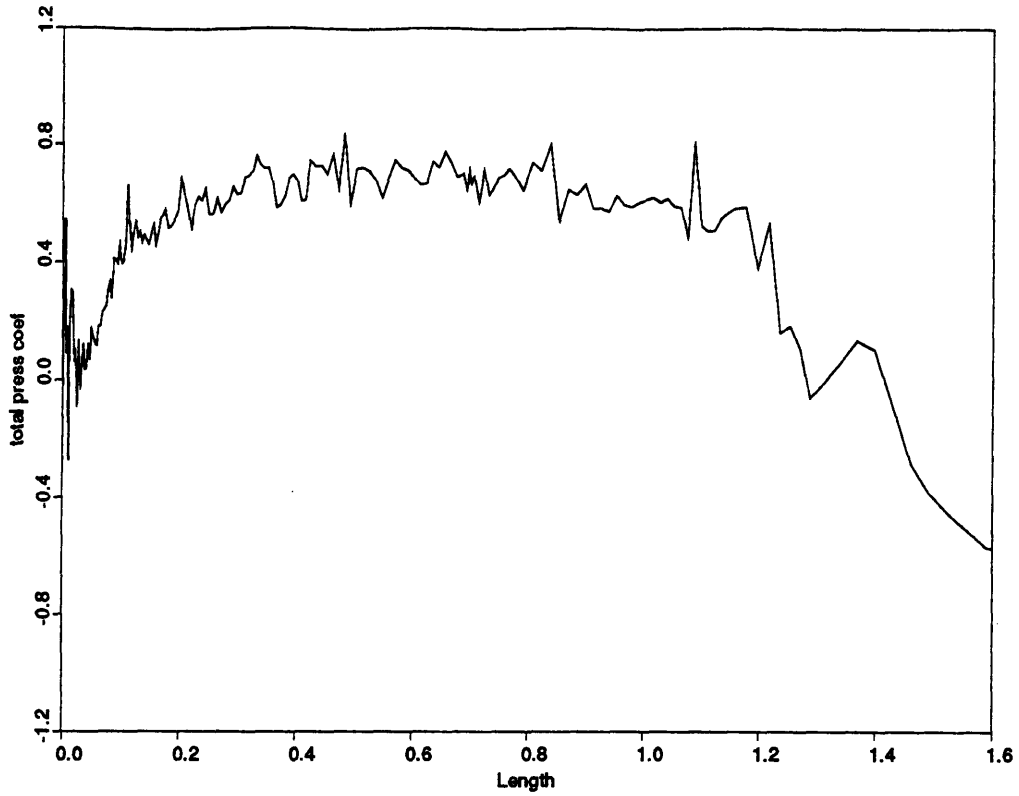

Figure 4.23: Computed total pressure coefficient variation along the vortex axis on adapted mesh, for $\alpha = 20.5°$.

efficient at the vortex axis is likely due to the lack of viscous effects, as was also observed in the comparison of the density at the vortex axis. The fluid in the subcore is the most rotational, which is associated with high entropy and large total pressure losses.

4.3.2.2 Vortex breakdown at 32 degrees angle of attack.

The second case is at an angle of attack of 32 degrees, at which vortex breakdown occurs far back on the wing. The parameters of this case were also chosen so that a comparison can be made with the solution obtained by Ekaterinas and Schiff. Based upon the experience of the previous case, at $\alpha = 20.5°$, the adaptation threshold was chosen so that 30% of the mesh nodes are selected for adaptation.

Figure 4.24 shows the pressure on the upper surface on the wing. The region of low pressure underneath the vortex is visible upstream of breakdown, whereas downstream of breakdown the data is somewhat irregular. Since breakdown is very far aft, this

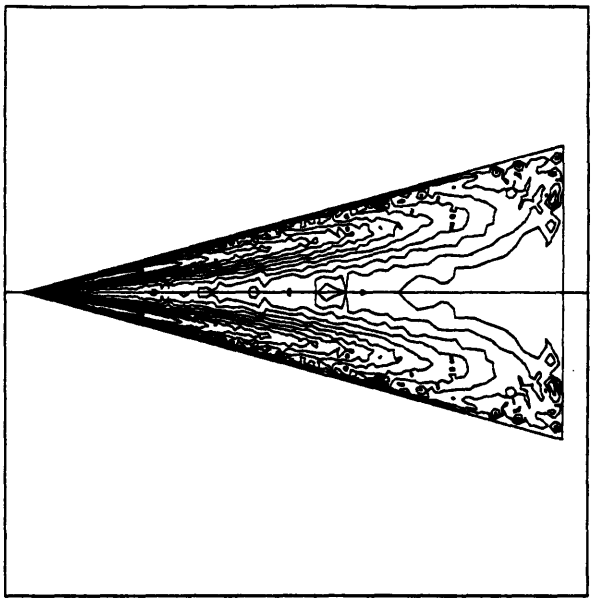

Figure 4.24: Pressure on the upper surface of the wing, at $\alpha = 32°$, on adapted mesh. Vortex breakdown occurs at 0.80 of root chord. Contour increment is 0.05, outermost contour value is 0.70.

region is difficult to see.

Figure 4.25 shows the axial velocity, in a plane normal to the wing at 90% of root chord, as computed on the adapted mesh. This can be compared with the axial velocity as computed by Ekaterinas and Schiff, which is shown in figure 4.26. In both figures, positive values are shown as solid lines, and negative values are shown as dashed lines.

Both figures 4.25 and 4.26 show a small region of reversed flow at the center of the vortex, which indicates the presence of vortex breakdown. The more symmetric appearance of the reversed flow region in Ekaterinas and Schiff's solution may be due to the more regular form of the grid, but it is also possible that this is a result of differences between the two solutions. Ekaterinas and Schiff characterize the vortex breakdown in their solution as the bubble type of breakdown, an assertion which they support with visualization of particle traces in the region of breakdown, and with the lack of unsteadiness in the solution.

The solutions computed in this thesis have a different character. There is significant

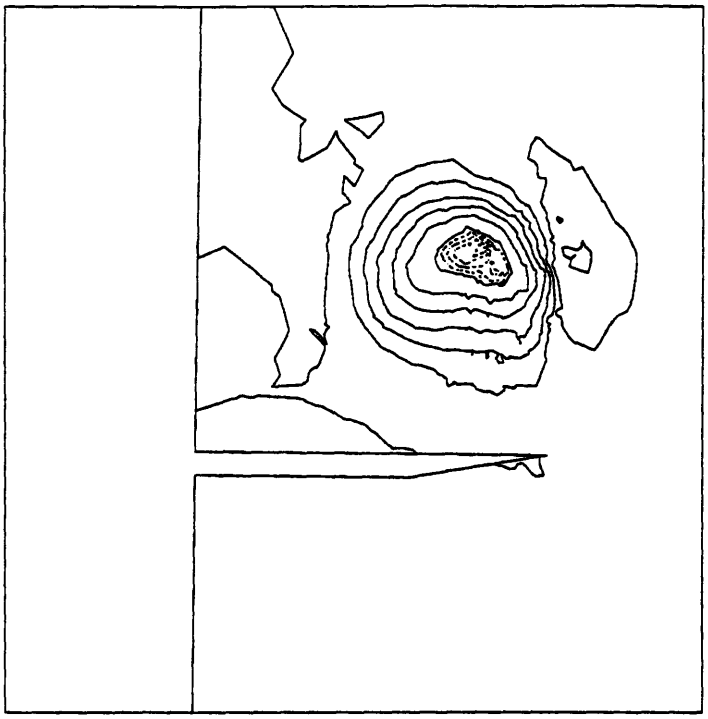

Figure 4.25: Computed axial velocity variation on adapted mesh at $x/c_R = 0.90$, for $\alpha = 32°$. Solid lines are positive values, contour increment is 0.05. Dashed lines are negative values, contour increment is 0.01.

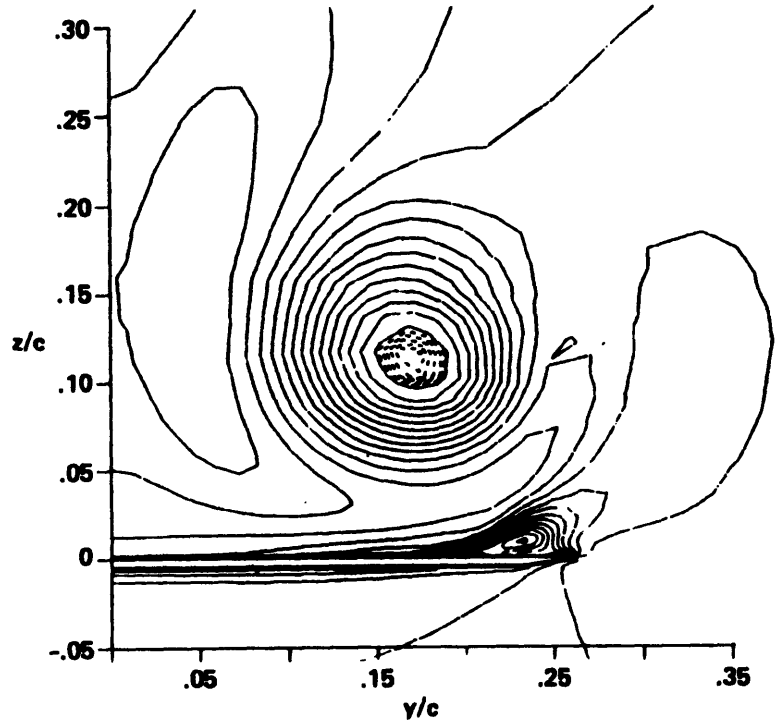

Figure 4.26: Axial velocity variation at $x/c_R = 0.90$, for $\alpha = 32°$, from Ekaterinas and Schiff [17].

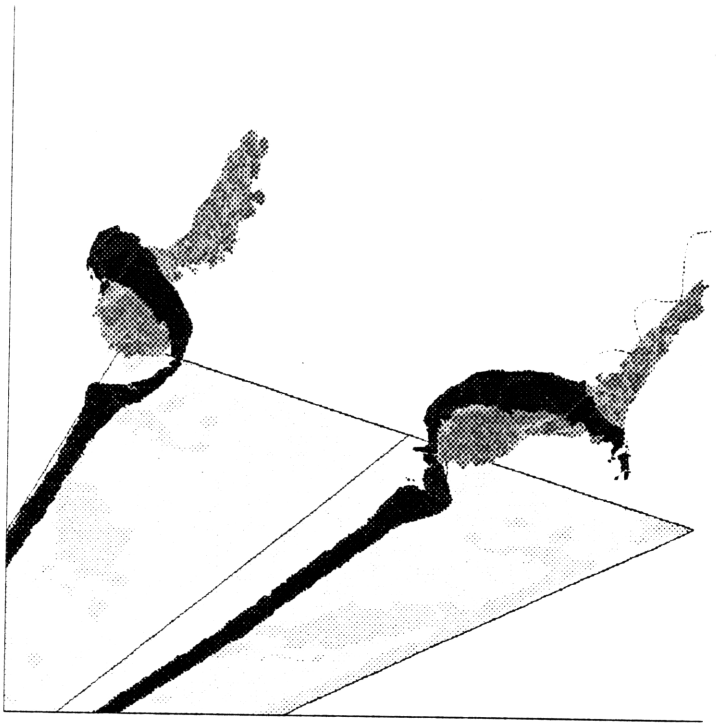

Figure 4.27: Vortex breakdown region, showing the vortex core and the region of reversed flow, for $\alpha = 32°$, on adapted mesh.

unsteadiness in this solution, which also appears in all other solutions in this thesis in which vortex breakdown is present. This unsteadiness is an indication that the breakdown is of the spiral type, in which the helical vortex core downstream of breakdown rotates about the vortex axis. Visualization confirms the presence of the spiral structure. Figure 4.27 shows a perspective view of the breakdown region. The vortex core is darkly shaded, the region of reversed flow is shown in gray. The vortex core is defined as the region of high fluid entropy. In the steady vortex upstream of breakdown, the entropy distribution is roughly cylindrical, and, since entropy is convected with the flow in the absence of viscous losses, a surface of constant entropy approximates a stream surface, until diffusion diminishes the entropy further downstream of breakdown. The vortex core clearly follows a spiral path around the region of reversed flow, with the opposite sense of rotation from the flow in the vortex. The relationship between the vortex core trajectory and the region of reversed flow is expected from a kinematic point of view, as the velocity associated with a helical vortex filament with the sense of rotation seen here will have an upstream component in the interior of the helix. Particle paths launched from within the vortex core upstream of breakdown also tend to follow the

helical form observed in the entropy variation.

It has been observed in swirling pipe flow experiments [72] that under certain conditions vortex breakdown can manifest in either the spiral or the bubble form, whereas under other conditions only one of the two forms occurs. A possible explanation for the difference in type of breakdown encountered in the two numerical solutions is that the flow conditions used are among those at which both types of breakdown are possible. In such situations where a unique solution does not exist, the choice of solution form can determined by the characteristics of the two solvers. The structured grid used by Ekaterinas and Schiff has lines of grid points that lie on rays emanating from the wing apex. Such a grid structure might more readily support an axisymmetric form of breakdown than it would the asymmetric spiral form. Since the spiral type of breakdown is more commonly observed in delta wing flows than the bubble type, possibly due to an instability of the axisymmetric bubble form [39], it is likely that the solutions obtained in this thesis are more realistic.

Figure 4.27 also illustrates several criteria for the vortex breakdown location, which were mentioned in section 4.3.1. Two possible criteria, both of which can be measured experimentally, are the location at which the vortex core begins to expand, and the location at which the core begins to follow a spiral path. The former is 10% of chord forward of the onset of reversed flow, and the latter is 5% of chord forward of the onset of reversed flow. The location of the onset of reversed flow is used throughout this thesis to indicate the location of vortex breakdown. As seen in figure 4.13, the numerically predicted location of breakdown is typically five to ten percent downstream of the experimentally measured location, which suggests that the choice of criterion for breakdown location is the major source of difference between the numerical predictions and the experimental measurements of breakdown location.

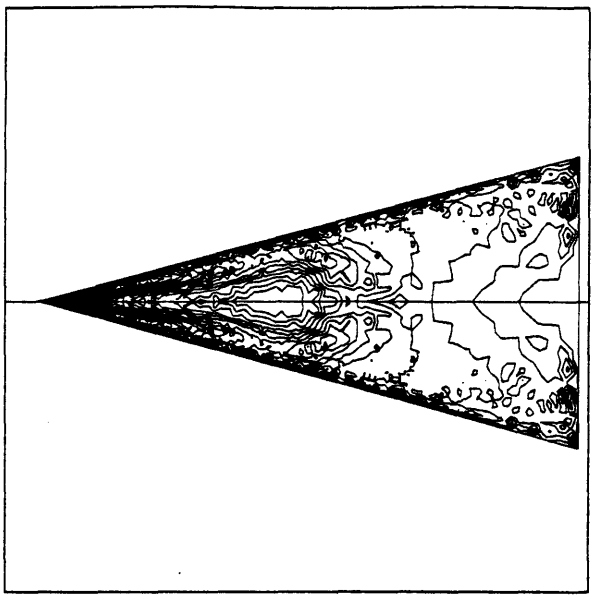

Figure 4.28: Pressure on the upper surface of the wing, at $\alpha = 42°$, on adapted mesh. Vortex breakdown occurs at 0.33 of root chord. Contour increment is 0.05, outermost contour value is 0.70.

4.3.2.3 Vortex breakdown at 42 degrees angle of attack.

The third case is at an angle of attack of 42 degrees. There is no existing data available for comparison. This case is included because of an interesting and unusual flow feature that appears. In this flow, the vortex undergoes a bubble type breakdown at 33% of the wing root chord, and then reforms as a coherent vortex, only to suffer a spiral type of breakdown further downstream.

Figure 4.28 shows the pressure on the upper surface of the wing. In contrast to figure 4.24, this figure clearly shows the effect of vortex breakdown, since breakdown occurs much further forward at this higher angle of attack. The region of intense low pressure is only visible near the apex, and abruptly ends beneath the breakdown region. A weaker area of low pressure is visible further downstream, where the reformed vortex swoops inward and towards the wing surface.

Figure 4.29 shows a perspective view of the region near breakdown. The wing upper surface is visible in the background, and the flow is from right to left. The vortex core

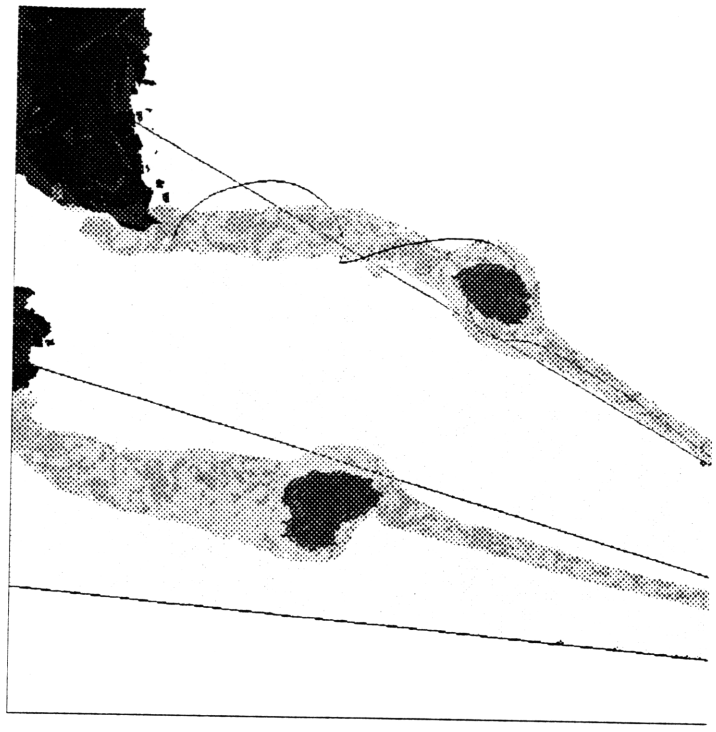

Figure 4.29: Vortex breakdown region, showing the vortex core and the region of reversed flow, for $\alpha = 42°$, on adapted mesh.

is represented by a surface of constant entropy, which is medium gray in shade, and has the slender cylindrical form of an intact vortex upstream of breakdown. The onset of breakdown is visible as a rapid widening of the core, followed by a small region of reversed flow, which is shown in a dark shade. The bubble extends only 4% of root chord downstream before expiring, being followed by a thicker but coherent vortex that attains 70% of the freestream axial velocity before it spirals out of the plane and begins to dissipate. Since the axial velocity at the center of the reformed vortex stays below the velocity of the free stream, the vortex is of the wake-like type, as opposed to the jet-like type, with high axial velocity, that appears upstream of breakdown. The helical vortex spirals around a large region of reversed flow which begins at 55% of root chord and is visible as the dark region to the far left.

Figure 4.30 shows the axial velocity in a plane, normal to the wing, that contains the vortex axis. The longitudinal cross section of the wing is visible beneath the vortex. The flow is from left to right, and dark areas represent high speed flow, while light areas represent low speed flow. The high axial velocity at the center of the vortex upstream

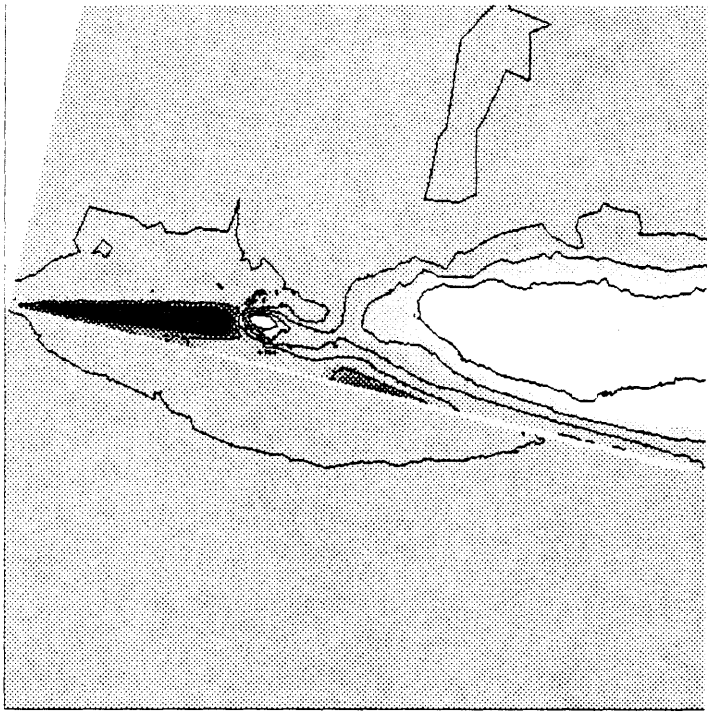

Figure 4.30: Computed variation of axial velocity through the vortex core, for $\alpha = 42°$, on adapted mesh. Contour increment is 0.1, innermost contour value is 0.

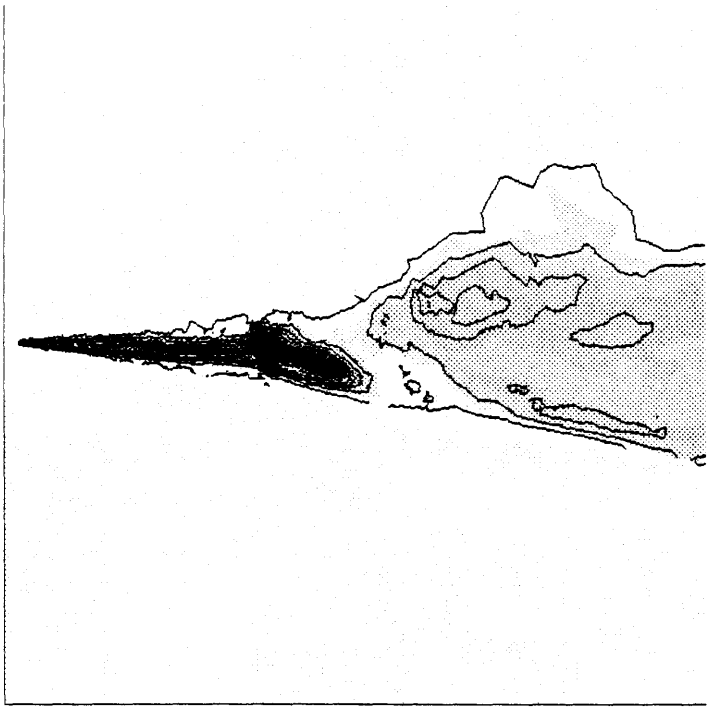

Figure 4.31: Computed variation of entropy through the vortex core, for $\alpha = 42°$, on adapted mesh. Contour increment is 0.01, outermost contour value is 0.01.

Figure 4.32: Flow visualization of the bubble type of vortex breakdown in swirling pipe flow, showing downstream reformation of the vortex core, from Sarpkaya [72].

of breakdown is visible towards the left. The vortex undergoes a rapid deceleration, immediately downstream of which the small region of reversed flow is visible. The larger region of reversed flow is to the right, and can be seen to extend past the trailing edge of the wing. Figure 4.31 shows the entropy in the same plane through the vortex axis. The dark areas represent regions of high entropy, and the light areas represent regions of low entropy. The fluid in the bubble has high entropy throughout, indicating that it originated in the vortex core upstream. The reformed core downstream of the bubble is visible for 10% of root chord before it leaves the plane. The much diffused helical vortex can be glimpsed downstream towards the top where it passes through the plane.

The reformation of the vortex downstream of breakdown, as seen in this solution, is not typically observed in the breakdown of delta wing leading edge vortices. However, it has been noted in both experiments and calculations of vortex breakdown in swirling pipe flows [72, 47], which can be seen in figure 4.32, which shows the bubble type breakdown in a swirling pipe flow experiment by Sarpkaya. While the vortex remains

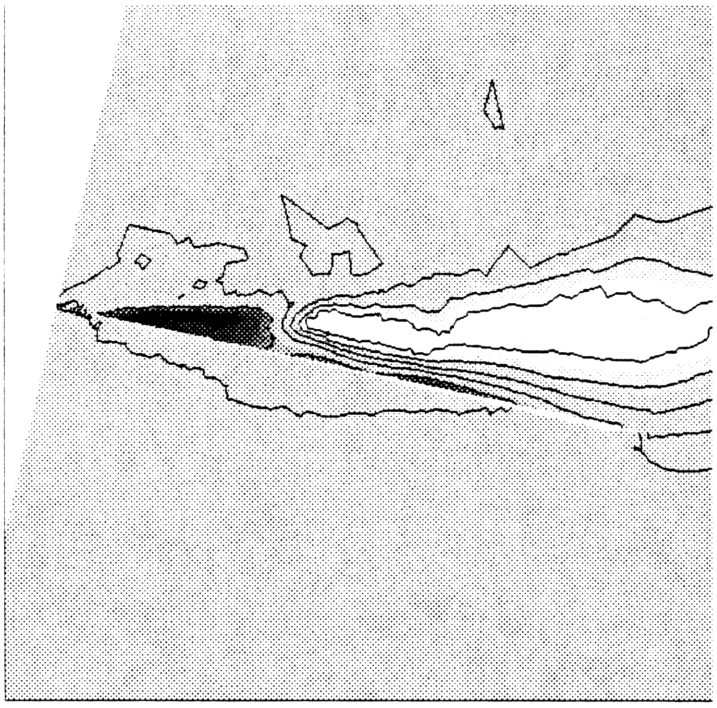

Figure 4.33: Computed variation of axial velocity through the vortex core, for $\alpha = 42°$, on coarse mesh. Contour increment is 0.1, innermost contour value is 0.

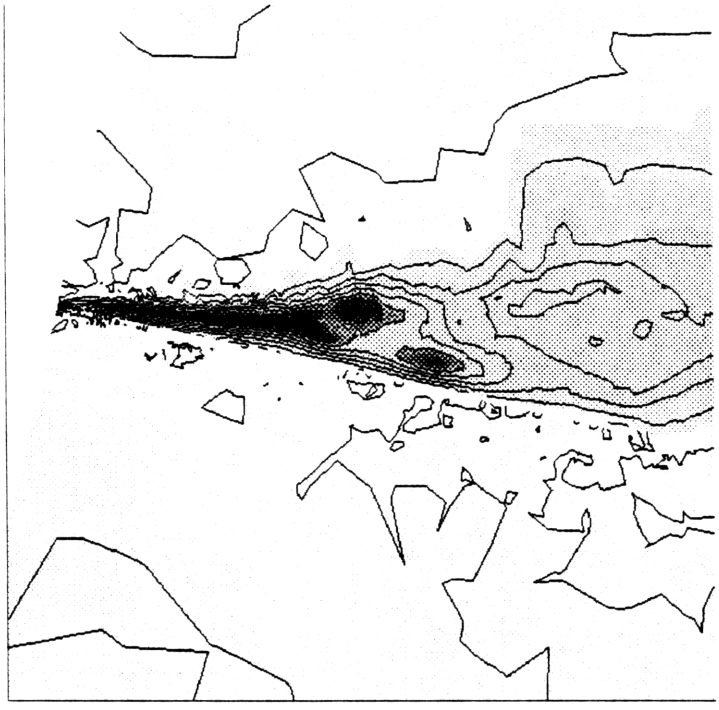

Figure 4.34: Computed variation of entropy through the vortex core, for $\alpha = 42°$, on coarse mesh. Contour increment is 0.01, outermost contour value is 0.01.

intact for about one bubble length downstream of the bubble before degenerating, it is not clear whether any helical structure is visible in the remains of the vortex. It is also unclear how accurate is the numerical solution presented here, as the coarse mesh solution shows no indication of the bubble type of breakdown. Figures 4.33 and 4.34 show the axial velocity and the entropy for the coarse mesh, in a plane through the vortex axis and normal to the wing, which can be compared with figures 4.30 and 4.31, which shows the adapted solution. Figure 4.33 shows that the region of reversed flow does not form a small bubble, and figure 4.34 shows that the vortex assumes the helical form immediately upon breakdown. The breakdown location on the coarse mesh is at 40% of root chord, which is almost a 10% difference from the breakdown location predicted on the adapted mesh. The difference between the coarse mesh solution and the adapted mesh solution suggests that the adapted mesh solution might not be mesh converged, and further differences could appear with additional refinement.

4.4 Pitching Wing Solution

Four time accurate simulations of the flow over a pitching wing were performed for a sinusoidal variation of five degrees of angle of attack, from 32 degrees to 37 degrees, and back to the original angle. As in Jarrah's experiments, the motion is not periodic; only a single sinusoid is performed. In this range of angle of attack, the position of vortex breakdown varies from about 60% to 90% of root chord. The free stream Mach number was 0.3, and the wing geometry is the same as described in section 4.2. The nondimensional pitch rate for all calculations was $K = 0.02$, so that the reduced frequency of the pitching motion was $k = 0.46$. The nondimensional pitch rate is in the range in which Jarrah performed his experiments, but the reduced frequency is not. The difference in reduced frequency in the present calculations and in Jarrah's experiments is due to the different range of angle of attack (see equation 2.31). In Jarrah's experiments, the angle of attack of the sinusoid motion ranged from zero to 30, 60 or 90 degrees. It is not clear *a priori* which of the two nondimensional parameters of the unsteady motion better

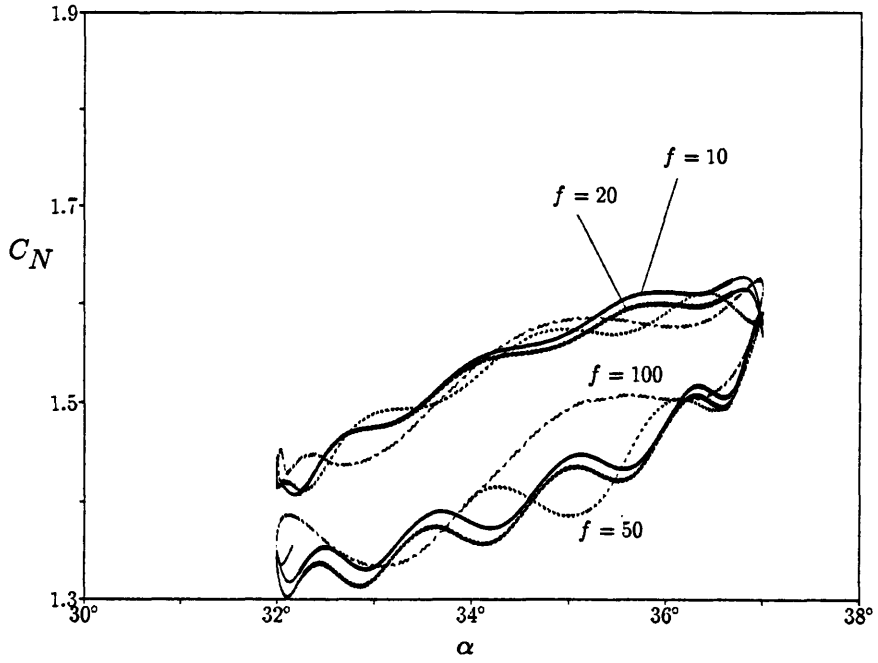

Figure 4.35: Variation of wing normal force versus angle of attack during pitching motion, showing effect of local time steps.

characterizes this flow. It must also be cautioned that these four solutions represent the same physical conditions, differing only in the extent to which local time steps were used. In addition, they were computed on a coarse mesh. Thus, care should be taken in generalizing the behavior seen.

The four solutions differ by the extent of the region in which local time steps are used during temporal integration (see section 3.5.2). The extent of local time steps is quantified by the acceleration factor, f, of the global time step. The quantity f is also the factor by which the computational time required to obtain the solution is reduced. *A priori* investigation of the initial flow field indicated that a value of f around 10 would still allow a meaningful solution. The factor f was given the values of 100, 50, 20 and 10, to determine the accuracy of the *a priori* estimate.

Figures 4.35 and 4.36 show the effect of varying the time step amplification factor. Figure 4.35 shows the normal force on the wing versus angle of attack during the pitching motion. Hysteresis is clearly evident in all of the solutions. The natural unsteadiness of the flow is superposed upon the unsteadiness due to the pitching motion, resulting in a high frequency variation. As discussed in section 4.3.1, the natural unsteadiness is due to

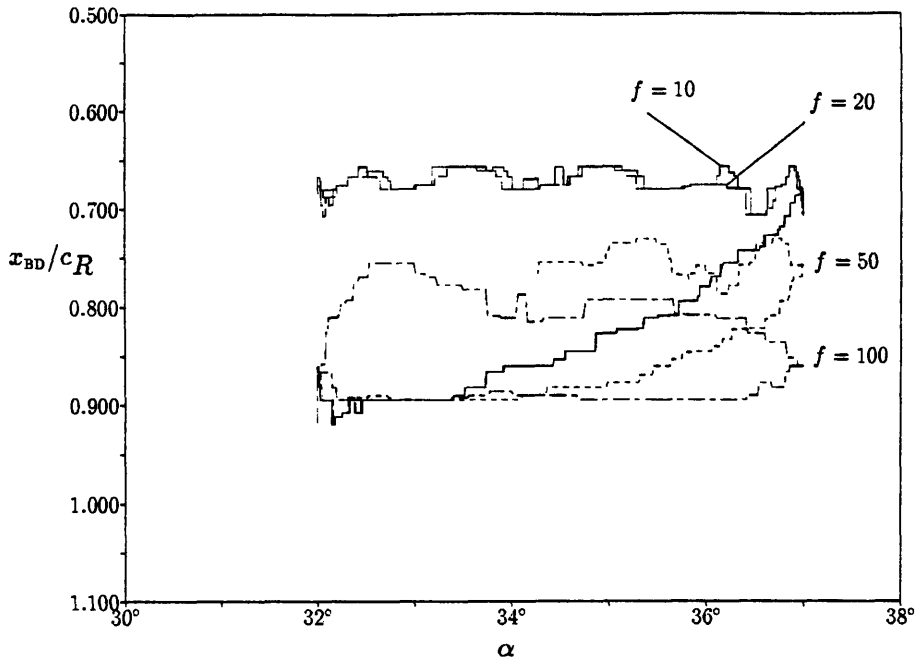

Figure 4.36: Variation of vortex breakdown position versus angle of attack during pitching motion, showing effect of local time steps.

the rotation of the helical vortex core downstream of breakdown, and by the fluctuation of the breakdown position. The magnitude of the time step amplification factor in the various solutions can be correlated with the wavelength of the natural fluctuation. The longer wavelength fluctuations correspond to a greater distortion of the time step in the region near vortex breakdown. The close agreement between the behavior with $f = 20$ and with $f = 10$ indicates that the region of local time steps does not encompass the breakdown region. This suggests that the solution with $f = 10$ is a good approximation to the strictly time accurate solution. It is important to note that at $f = 50$ both the nonfluctuating variation due to the pitching motion, and the amplitude of the natural fluctuation, appear to be well predicted, even though the frequency of the fluctuation is inaccurate.

Figure 4.36 shows the position of vortex breakdown versus wing angle of attack during the pitching motion. The effect of the use of local time steps is much more visible than in figure 4.35. All solutions show a lag in the upstream progression of the position of vortex breakdown during the upward pitching half of the motion, and a relatively static position of breakdown during the downward pitching half of the motion. In the solutions for which $f = 100$ and $f = 50$, the inclusion of the vortex breakdown in the

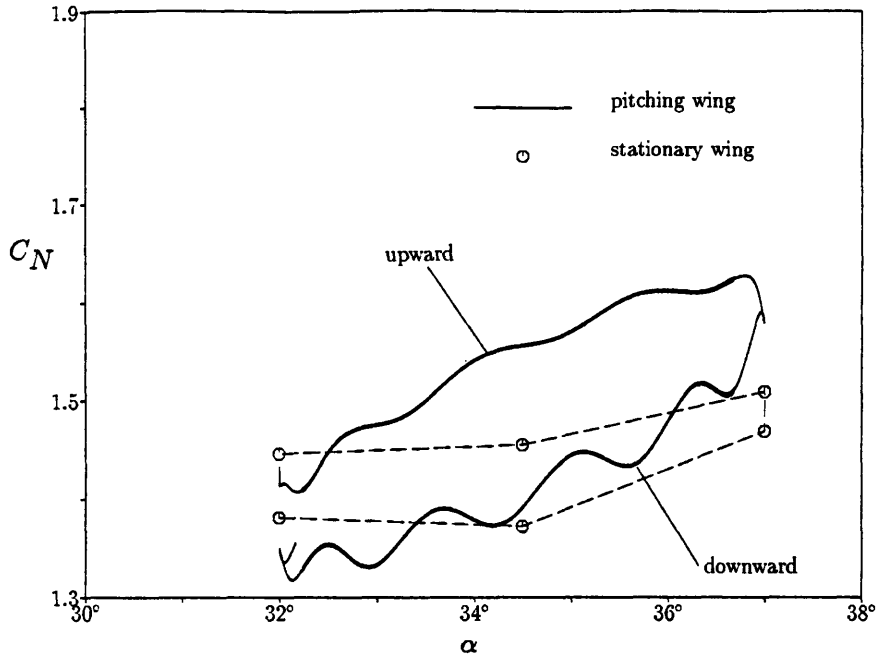

Figure 4.37: Variation of wing normal force versus angle of attack during pitching motion, compared with stationary wing computations.

region of local time steps clearly produces incorrect behavior in the solution. The speed at which the breakdown position moves upstream during the upward pitching half of the motion is decreased, with the result that the location of breakdown during the downward half of the motion is too far aft. The behavior of breakdown at $f = 20$ and $f = 10$ are very close, indicating that the solution with $f = 10$ is a good approximation to a strictly time accurate solution. The great sensitivity of breakdown position to a wide variety of factors has also been noted by other researchers [71].

In figures 4.37 and 4.38, the variations using an amplification factor of $f = 10$ are compared with values for a stationary wing for the same range of angle of attack. The multiple values of the stationary wing data indicate the rangle of natural fluctuations of the normal force, as was discussed in section 4.3.1. Figure 4.37 shows that the hysteresis provides for a higher normal force than is possible with a stationary wing. The maximum normal force, which occurs near the maximum angle of attack, is about 15% higher than the normal force on a stationary wing. This range of angle of attack is approximately where the stationary wing generates the largest normal force.

The fluctuations of the normal force due to natural unsteadiness have a different

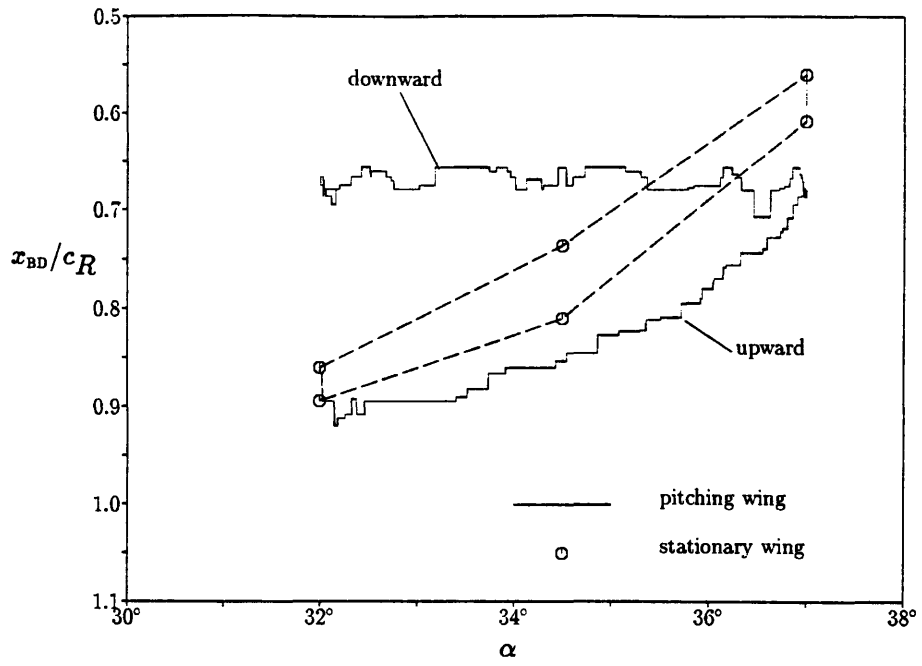

Figure 4.38: Variation of vortex breakdown position versus angle of attack during pitching motion, compared with stationary wing computations.

appearance depending on the direction of the pitching motion. During the upward pitching motion, the amplitude and the frequency of the fluctuations are reduced. The frequency change is probably due a phenomenon similar to the Doppler effect, as the position of vortex breakdown is moving upstream, while the disturbances that cause the fluctuations propagate downstream from the breakdown position. The amplitude change follows from the frequency change and the conservation of wave action [44, §4.6]. No natural fluctuations were reported in any experimental measurements of a pitching delta wing. This is likely due to the high reduced frequency of the pitching motion in the present calculation. At the lower reduced frequencies of the experiments, the natural fluctuation would appear to be faster, relative to the pitching motion, and could easily be interpreted as or overwhelmed by noise. In addition, any ensemble averaging of several sets of pitching wing measurements will tend to wipe out the fluctuations. The fluctuations during the downward pitching motion have nearly the same amplitude as those observed in the stationary wing flows. This is not surprising, in light of the behavior of the breakdown position during the downward motion.

Figure 4.38 shows a significant lag in the position of vortex breakdown during the pitching motion, relative to its position in the flow over a stationary wing. The natural

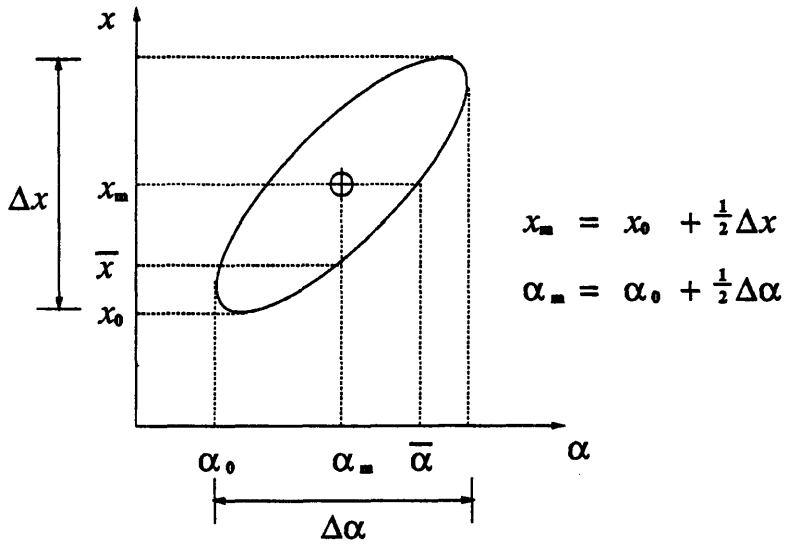

Figure 4.39: Determination of phase delay of two signals that vary with the same frequency.

fluctuations in breakdown position may be present, but at too small an amplitude to be visible. The phase lag can be measured, by modeling the motion of the breakdown position as a sinusoid. Recall that the angle of attack varies as

$$\alpha(t) = \alpha_0 + \tfrac{1}{2}\Delta\alpha\,(1 - \cos\phi)\,, \tag{4.7}$$

in which $\phi = kM_\infty t$ is the phase. The breakdown position can be expressed as

$$x_{\mathrm{BD}}(t) = x_0 + \tfrac{1}{2}\Delta x\,(1 - \cos(\phi + \delta))\,, \tag{4.8}$$

in which δ is the phase lag relative to the angle of attack. The phase lag can be determined by measuring the breakdown position when the angle of attack is at its mean value, or vice versa (see figure 4.39). At a phase of $\phi = \pi/2$, the angle of attack takes its mean value $\alpha_{\mathrm{m}} = \alpha_0 + \frac{1}{2}\Delta\alpha$, while the breakdown position has the value

$$\bar{x} = x_0 + \tfrac{1}{2}\Delta x\,(1 + \sin\delta)\,. \tag{4.9}$$

Likewise, when $\phi + \delta = \pi/2$, the breakdown location has its mean value, x_{m}, and the

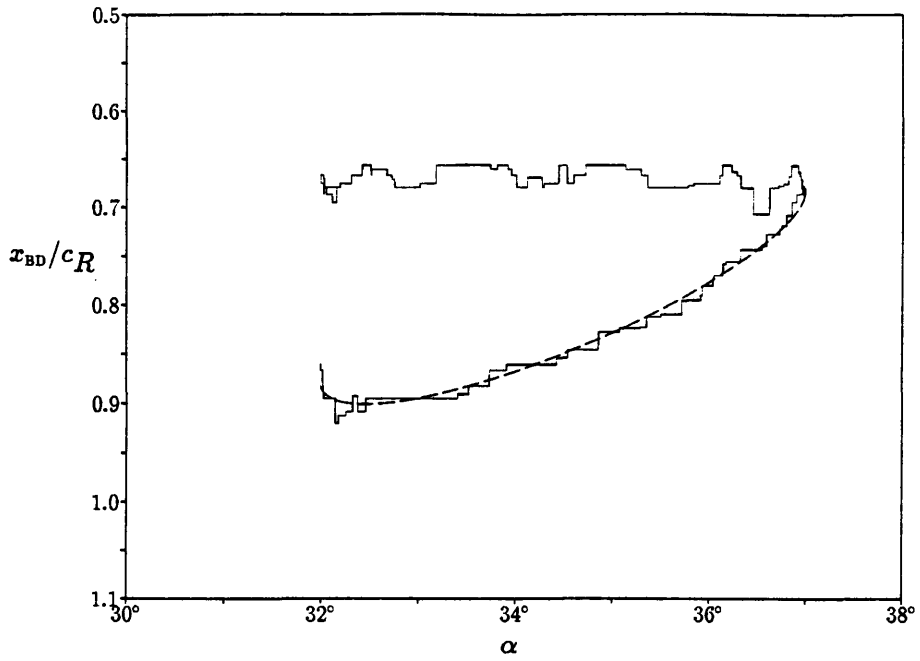

Figure 4.40: Variation of vortex breakdown position versus angle of attack during pitching motion, compared with upward pitching half of ideal phase lagged sinusoidal motion.

angle of attack is

$$\bar{\alpha} = \alpha_0 + \tfrac{1}{2}\Delta\alpha\,(1 - \sin\delta)\,. \tag{4.10}$$

The phase lag is thus found as

$$\sin\delta = \frac{\bar{x} - x_{\rm m}}{\frac{1}{2}\Delta x} \tag{4.11}$$

$$= -\frac{\bar{\alpha} - \alpha_{\rm m}}{\frac{1}{2}\Delta\alpha} \tag{4.12}$$

Analysis of the data shown in figure 4.38 reveals the phase lag δ to be 35 degrees. Equations 4.11 and 4.12 yield nearly the same value for the phase delay. Figure 4.40 shows the upward pitching part of this sinusoidal motion superimposed upon the variation of breakdown position seen in the simulation. The agreement is surprisingly good.

Using the sinusoidal approximation, the speed at which the breakdown position moves can be found. From equation 4.8, the speed of motion of the breakdown position is

$$v_{\rm BD}(t) = \tfrac{1}{2}kM_\infty\Delta x\sin(\phi + \delta) \tag{4.13}$$

which has a maximum value of

$$v_{BD} = \frac{1}{2} k M_\infty \Delta x. \tag{4.14}$$

For the solutions obtained here, this speed is 0.046 of the free stream speed. It has been speculated that the cause of the lag in breakdown position is due to the fact that the breakdown position can only move slowly. A value of one tenth of the free stream speed has been mentioned [31], so the present results yield the same order of magnitude of the observed propagation speed.

The behavior of the breakdown position during the downward pitching motion is very surprising. Instead of showing the same type of phase lagged behavior evident during the upward pitching motion, the location of vortex breakdown remains roughly constant, at its furthest forward position. This explains why the amplitude of the normal force fluctuations during the downward pitching motion is the same as that in the flow over a stationary wing. Fluctuation is also present in the breakdown position, which again has roughly the same amplitude seen in the flow over a stationary wing. The failure of the breakdown to move aft during the downward pitching motion may be a mesh effect, since the mesh spacing increases towards the rear of the wing, and it has been observed that insufficiently fine mesh resolution tends to inhibit the correct modeling of vortex breakdown. Experiments have found the motion of the breakdown position during upward and downward pitching motion to be fairly similar [81]. This is an important area for further study.

Chapter 5

Conclusion

> But where shall wisdom be found? and where is the place of understanding? Man knoweth not the price thereof; ... for the price of wisdom is above rubies.
>
> Job 28:12–13,18

In this thesis, an adaptive solution procedure for the simulation of inviscid, compressible flow fields has been described, and solutions of flow about sharp leading edge delta wing computed with this solver have been presented. Flow solutions were obtained for both stationary and pitching wings. Chapter two presented the Euler equations, which govern inviscid, compressible flow, and described suitable physical boundary conditions. Chapter three described the numerical solution procedure, the distinguishing features of which are the use of adaptive refinement by mesh point embedding on an unstructured mesh of tetrahedral cells, and an artificial dissipation operator with a higher order of accuracy. In chapter four, stationary and pitching wing flow solutions were presented and discussed, which included comparisons with experimental data and with other numerical simulations.

The new contributions in this thesis are as follows. In the development of numerical algorithms, a new method for the acceleration of time accurate computations was devised, implemented and validated. The method involves the use of local time steps in regions where numerical stability places a strict limit on the size of the time step. This method was found to allow an order of magnitude reduction in the computational time required to complete the pitching wing simulation presented in this thesis. This

method is applicable to the solution of flows in which the most important unsteadiness does not occur in the region of strictest time step stability limits.

This thesis also represents the first demonstrated use of unstructured adaptive mesh techniques to simulate the behavior of vortex breakdown, either in the flow over a delta wing or in other flows. The use of adaptation was demonstrated to produce good agreement with existing data for delta wing flows. The flow solutions in this thesis exhibit the spiral form of vortex breakdown, which is commonly observed in experimental studies of delta wing flows, whereas many previous researchers obtained solutions showing the bubble type of breakdown, which is less common. This thesis also numerically demonstrates the validity of the Euler equations in capturing the important flow feature of vortex breakdown, in the flow around a sharp edged delta wing. This supports research that posits that vortex breakdown is primarily an inviscid phenomenon [14]. The pitching wing simulation in this thesis exhibits both hysteresis in normal force, and a lag in the motion of the position of vortex breakdown. These are key features of this type of flow that have been observed in the wind tunnel, so that the present work validates the use of the Euler equations to simulate pitching delta wing flows with vortex breakdown for research or design purposes.

A summary of this thesis is presented below, and is followed by recommendations for further work.

5.1 Summary

The solver uses the Galerkin finite element method with linear shape functions, on an unstructured mesh of tetrahedra. The lumped mass matrix allows the use of explicit temporal integration. The method of Holmes and Connell is used to create an artificial dissipation operator with a higher order of accuracy. The solver is capable of adaptive refinement via mesh point embedding to increase the resolution in regions of interesting

flow features. Entropy is used as the adaptation indicator for vortical flows, since it is invariant under a change of reference frame. Local time steps are used to reduce the computational time required. For time accurate calculations, the use of local time steps is restricted to a small region of the solution domain, to minimize the inaccuracy introduced.

The solver was used to simulate the flow over a stationary sharp edged delta wing over a wide range of angles of attack, which included regimes both with and without vortex breakdown. The Mach number of all cases was 0.3, and the leading edge sweepback angle was 75 degrees. One level of adaptation was performed for all cases. The computations performed with adaptation showed excellent agreement with normal force data measured by Jarrah, and good agreement with pitching moment and vortex breakdown location measured by Hummel and Srinivasan. The use of adaptation was necessary to get reasonable agreement with the normal force and pitching moment data. The differences in the prediction of vortex breakdown location may be due to the use of different criteria to define the location of breakdown, which resulted in the numerically predicted breakdown location to be five to ten percent of root chord aft of the experimentally measured location. All solutions exhibited periodic fluctuations of normal force, pitching moment, and vortex breakdown position.

The details of the flow fields at three angles of attack were compared with experimental data and with numerical solutions obtained by other researchers. At an angle of attack of 20.5 degrees, the leading edge vortex is intact over the entire wing. With the use of adaptation, the details of the vortex were well resolved. This solution was compared with a structured grid Navier-Stokes solution obtained by Ekaterinas and Schiff. The adapted solution agreed well with Ekaterinas and Schiff's calculation, although the fluid at the core of the vortex was more rarefied in the Euler calculation, which is expected due to the lack of viscous effects. Also, the secondary vortex did not appear in the Euler solution, since it is an effect of boundary layer separation. The strength of the vortex, as measured by total pressure coefficient at the center, was comparable to that obtained by Goodsell using a structured grid Euler solver. Neither calculation matched

the total pressure coefficient measured by Verhaagen and van Ransbeeck, which is to be expected due to the lack of viscosity in the models. The location of the vortex core was consistent in the three calculations and in the experiment, showing that the structure of the primary vortex is not strongly influenced by the characteristics of the secondary vortex.

At an angle of attack of 32 degrees, vortex breakdown occurs over the rearward part of the wing. This solution was compared with a calculation obtained by Ekaterinas and Schiff. Although both solutions predict vortex breakdown at approximately the same chordwise location, the nature of the breakdown differs between the two solutions. Whereas Ekaterinas and Schiff described the breakdown in their solution as the axisymmetric bubble type of breakdown, with negligible intrinsic unsteadiness, the solution obtained for this thesis was clearly of the asymmetric spiral type of breakdown, and underwent substantial fluctuations, as indicated by the behavior of the normal force on the wing. The bubble type of breakdown is rarely observed in experiments involving delta wings, and has been characterized as unstable by some researchers. Quantitative measurements also typically show periodic unsteadiness associated with vortex breakdown in delta wing flows. A possible explanation for the difference in the nature of breakdown in the two solutions is that the structured grid used by Ekaterinas and Schiff intrinsically favors the axisymmetric configuration, whereas the unstructured mesh used in this thesis does not.

At an angle of attack of 42 degrees, vortex breakdown occurs over the forward part of the wing. There is no previous work at this angle of attack in sufficient detail to provide a meaningful comparison of results. When adaptation is performed for this case, an interesting flow feature is exposed. The vortex appears to break down in the axisymmetric bubble mode and then reform, only to break down again, in the asymmetric spiral form. Similar behavior has been observed in experiments of vortex breakdown in confined swirling flows. The fact that this double breakdown structure appeared only in the adapted solution is a strong indication that the solutions presented in this thesis are not mesh converged.

Time accurate calculations were performed for a wing undergoing sinusoidal motion in angle of attack from 32 degrees to 37 degrees, and back to the original value. The nondimensional pitch rate was 0.02, and the reduced frequency was 0.46. Variation of the extent of the use of local time steps validated the result of *a priori* investigation of the initial flow field to select a region of local time steps that would allow satisfactory accuracy. Hysteresis was observed in the behavior of normal force, allowing a fifteen percent greater force to be generated that that associated with a stationary wing at the maximum angle of attack. During the upward pitching motion, the position of vortex breakdown showed a phase lag with respect to the changing angle of attack. However, during the downward pitching motion, the position of breakdown remained relatively fixed at its farthest forward location. This behavior has not been observed in experiments. It is not known whether this represents a new physical behavior of vortex breakdown propagation or whether it is a numerical artifact.

The contour and line plots of the solutions displayed in this thesis were typically jagged and irregular in appearance. This was demonstrated not to be a reflection upon the accuracy of the solutions, but to be an effect of the process of interpolation of data stored on an irregular unstructured mesh onto a viewing plane or line.

5.2 Recommendations for Further Work

1. The analysis of the unsteady flow fields that involve vortex breakdown also indicated a need for more comprehensive methods to analyze unsteady flow fields. Post processing techniques are adequate for the analysis of steady flow fields, but a full unsteady flow field, consisting of data at every iteration, would put a severe burden upon the resources that are currently available for memory storage. Steady flow tools can be used to analyze a single iteration of an unsteady flow, but the fluctuations in the flow could be at an extreme point of the unsteady behavior, and thus would not represent the typical features of the flow. In analysis and in experiments, unsteady flow behavior is frequently represented as the sum of

a mean flow field and a fluctuating perturbation. Forming such a time-averaged representation of an unsteady numerical simulation would allow a researcher to study the typical characteristics of the flow using post-processing tools for steady flow. Care must be taken to determine whether the flow can be linearized about the time mean. The motion of vortex breakdown may be too nonlinear to allow the flow to represented as the sum of a mean flow and a small perturbation.

2. The analysis of the flow at 42 degrees angle of attack revealed a significant flow structure that appeared only in the adapted solution. This indicates that this solution is not mesh converged, and suggests that none of the other solutions presented in this thesis are mesh converged, either. In order to obtain mesh converged solutions of delta wing vortex flows using adaptive refinement, a tremendous amount of memory storage will be required. The computations in this thesis, with one level of adaptation, required 25 million words of storage on the Cray X/MP supercomputer, and consumed up to 15 hours of processing time. Performing a second level of adaptation using the method developed in this thesis would roughly quadruple the memory and CPU usage, resulting in a need for 100 million words of storage, and would require 60 hours of processor time. This is above the range of resources routinely available to the typical researcher at the present time. Due to this limitation, the best approach to investigate mesh convergence of delta wing flows may involve the use of structured or unstructured hexahedral cell meshes, which typically require less memory storage per mesh node than do methods which use a tetrahedral cell mesh structure. The quest for mesh convergence is unlikely to be meaningful in the context of unsteady flow with vortex breakdown, as the nature of the unsteadiness downstream of breakdown is expected to be disorganized. Only steady flows, or unsteady flows with a great degree of regularity, are suitable for mesh convergence studies.

3. The flow solutions presented in this thesis required a large amount of computational processing time to calculate. This is primarily due to the restrictive time steps imposed by the explicit temporal integration procedure. Although the use of local time steps in restricted regions of the flow allowed the acceleration of time

accurate computations by a factor of ten, more can be done. There is a wide range of implicit temporal integration procedures that allow a less restrictive time step to be used, and thus allow solutions to be obtained with the use of less computational effort. A particularly promising method is a point implicit procedure that has a resemblance to Gauss-Seidel integration. This procedure has been seen to decrease by a factor of five the computational time required to obtain a steady solution. The use of the point implicit temporal integration is inappropriate in conjunction with the central difference type of spatial discretization used in this thesis. Thareja *et al.* [79] and Batina [6] have used the point implicit temporal integration with an upwind spatial difference. Upwind spatial differencing also has the potential to further decrease the computational time needed, by eliminating the need for explicitly added artificial dissipation, the computation of which takes up a large fraction of processor time. In addition, upwind schemes are also capable of greater resolution of flow features than central difference schemes, an ability which also should be explored in more detail in the context of delta wing vortex flows and vortex breakdown.

4. The motion of the position of vortex breakdown during the pitching motion exhibited the peculiar behavior of remaining relatively fixed at its most forward location during the downward pitching part of the motion. Since this behavior has not been observed in experiments, it might be an artifact of the numerical procedure, possibly related to the variation of the mesh resolution. In order to resolve this issue, a simulation of the pitching motion should be performed with a finer mesh. Due to the amount of computational resources this will require, such a calculation will require a more efficient algorithm, as discussed above. In addition, motion with a variety of nondimensional pitch rate and range of angle of attack should be performed, to assess the the influence of the parameters on the motion of vortex breakdown.

Appendix A

Acceleration of Time Accurate Computation

The temporal integration of the Euler equations can be symbolically expressed as the system of equations

$$U_i^{n+1} - U_i^n = \delta U_i = \frac{\Delta t_i}{V_i} R_i \tag{A.1}$$

which spans the set of mesh nodes by the index i, in which U_i is the state vector of conserved quantities at a node, Δt_i and V_i are the time step and a volume associated with a node, and R_i is a generalized residual. The time step Δt_i is limited by a stability constraint at each node,

$$\Delta t_i \leq \Delta t_{\mathbf{max},i}, \tag{A.2}$$

where the maximum stable time step can be expressed as

$$\Delta t_{\mathbf{max},i} = \lambda_{\mathbf{max}} \frac{V_i}{S_i \left(a_i + q_i \right)} \tag{A.3}$$

where λ is the CFL number, S_i is an area, a_i is the sonic speed, and q_i is the flow speed. For strict time accuracy, the time step is a global quantity, so Δt_i must be the same at every mesh node. Stability must be maintained at every node, so that the global time step must be no greater than the minimum, over the set of mesh nodes, of the maximum stable time step at the node,

$$\Delta t_i = \Delta t_{\mathbf{global}} = \min_i \Delta t_{\mathbf{max},i}. \tag{A.4}$$

This can lead to problems if the mesh spacing varies widely. The velocity terms in equation A.3 are insensitive to mesh spacing, so that the maximum stable time step

scales with mesh spacing as

$$\Delta t_{\max,i} \sim \frac{\Delta x_i^3}{\Delta x_i^2} \sim \Delta x_i. \tag{A.5}$$

Thus, very close mesh spacing will create a very strict global time step limitation. This yields a stiff system of equations, with the time step being determined by a restrictive stability criterion, rather than by accuracy considerations.

In the time asymptotic calculation of steady flow, it is unnecessary to accurately model the time derivative, since in the converged solution it will vanish. Commonly, the restriction of a globally uniform time step is relaxed, so that the time step at a node is determined by the local stability limit. The method of local time steps allows convergence to steady state to be reached in fewer iterations.

The use of local time steps in a time accurate calculation will introduce inaccuracy. The global effect of the inaccuracy can be minimized by restricting the use of local time steps to the most closely spaced regions of the mesh, where the small local time steps will occur. This allows the flow in the coarser regions of the mesh to be integrated in a strict time accurate fashion. The extent of the use of local time steps is quantified by the global time step acceleration factor, f, which is the ratio of the global time step to the minimum local time step. It is also the factor by which the number of iterations needed to integrate a fixed time interval is diminished. The time step at each node is now given by

$$\Delta t_i = \min\left(\Delta t_{\text{global}}, \Delta t_{\max,i}\right), \tag{A.6}$$

and the *time step ratio* η_i is defined to be

$$\eta_i = \frac{\Delta t_{\text{global}}}{\Delta t_i}. \tag{A.7}$$

The time step ratio has a value of unity at the nodes that are integrated time accurately, and goes to a maximum of f at the node that has the strictest time step stability limit.

The effect of the inaccuracy due to the use of local time steps on the solution in the

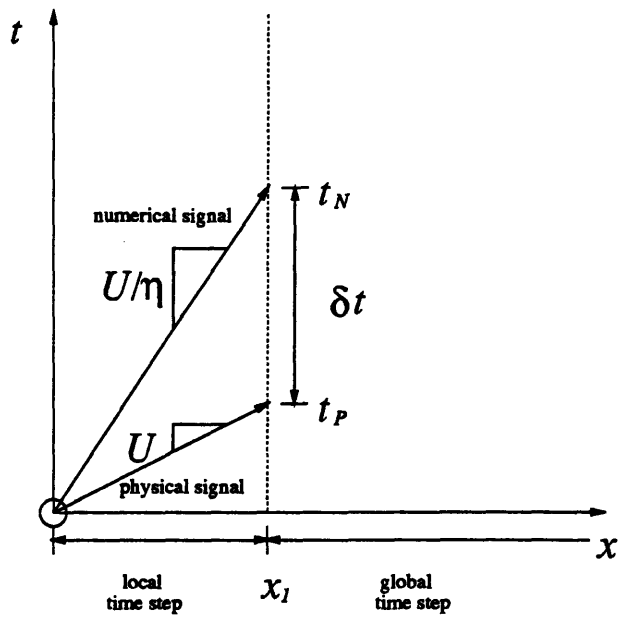

Figure A.1: Propagation of physical and numerical waves in a region of local time steps.

time accurate region can be seen by considering the propagation of a small amplitude characteristic wave through a region of local time steps. Physically, the wave travels at a speed U_P, which for the Euler equations can have the values q, $q+a$ or $q-a$, depending upon to which characteristic family the wave belongs. Due to the use of a nonphysical time step value, wave propagation will be slowed in the local time step region. Consider the propagation of a wave during a single timestep, at a physical velocity U_P. The wave will travel a distance $\delta x_P = U_P \Delta t_{\text{global}}$. In the region of local time steps, the numerical simulation of the wave will travel a shorter distance, $\delta x_N = U_P \Delta t_i$, due to the lesser time step. Since the local and global time steps are related by equation A.7, the equivalent numerical wave propagation speed can be expressed as

$$U_N = \frac{\delta x_N}{\Delta t_{\text{global}}} = \frac{U_P \Delta t_i}{\Delta t_{\text{global}}} = \frac{U_P}{\eta_i}. \tag{A.8}$$

The propagation of the physical and numerically simulated waves is shown in a space-time diagram in figure A.1. The physical wave traverses the region of local time steps in a time

$$t_P = \int_0^{x_1} \frac{dx}{U_P} \tag{A.9}$$

while the numerical wave arrives later, at time

$$t_N = \int_0^{x_1} \frac{dx}{U_N} \tag{A.10}$$

$$= \int_0^{x_1} \frac{dx}{U_P/\eta}. \tag{A.11}$$

Note that η varies in space. The effect of the use of local time steps can be thought of a time delay determined by

$$\delta t = t_N - t_P, \tag{A.12}$$

which, upon substiution of equations A.9 and A.11, can be written as

$$\delta t = \int_0^{x_1} \left(\frac{1}{U_P} - \frac{1}{U_P/\eta} \right) dx \tag{A.13}$$

$$= \int_0^{x_1} \left(\frac{\eta - 1}{U} \right) dx \tag{A.14}$$

$$= (\bar{\eta} - 1) \frac{x_1}{U}, \tag{A.15}$$

where $\bar{\eta}$ is the average value of the time step ratio in the region of local time steps. Using the definition of η in equation A.7, the time delay is

$$\delta t = \left[\overline{\left(\frac{\Delta t_{\text{global}}}{\Delta t_i} \right)} - 1 \right] \frac{x_1}{U} \tag{A.16}$$

which can be related to the global time step by

$$\frac{\delta t}{\Delta t_{\text{global}}} = \left[\overline{\left(\frac{1}{\Delta t_i} \right)} - \frac{1}{\Delta t_{\text{global}}} \right] \frac{x_1}{U}. \tag{A.17}$$

If the local time step is much smaller than the global time step, then the second term can be neglected. The local time step can be approximated using equations A.3 and A.5 to form

$$\Delta t_i \approx \frac{\delta x_i}{a_i} \tag{A.18}$$

so that

$$\frac{\delta t}{\Delta t_{\text{global}}} \approx \frac{\overline{a}}{\overline{\Delta x}} \frac{x_1}{U} \tag{A.19}$$

$$\approx \frac{1}{M_\infty} \frac{x_1}{\overline{\overline{\Delta x}}} \tag{A.20}$$

$$\approx \frac{N}{M_\infty} \tag{A.21}$$

where

$$N = \frac{x_1}{\overline{\overline{\Delta x}}} \tag{A.22}$$

is approximately the length of the region of local time steps, in mesh cells. The freestream Mach number, M_∞, is not varied by large factors, so the relationship between the time delay and the global time step is determined primarily by the size, in mesh cells, in the region of local time steps.

Appendix B

Two-Dimensional Validation of the Method of Regional Local Time Steps

Section 3.5.2 describes the method of regional local time steps, which allows the acceleration of time accurate computations. This method was validated by performing a simulation of the unsteady flow past a flat plate normal to the incoming flow. The unsteadiness is due to the shedding of vorticity from the sharp edges of the plate, which forms a set of distinct vortices. A schematic drawing of the vortex street is seen in figure B.1. This flow was chosen because of the similarity between vorticity generation in it and at the sharp leading edge of a delta wing. Similarly, very fine mesh resolution is needed at the sharp edge. This can be seen in figure B.2, which shows the mesh of triangles used for this problem. The mesh contains 5552 nodes and 10871 triangles. The mesh spacing in the vicinity of the edge of the plate is one percent of the length of the plate. Figure B.3 shows contours of the pressure in a strictly time accurate simulation of

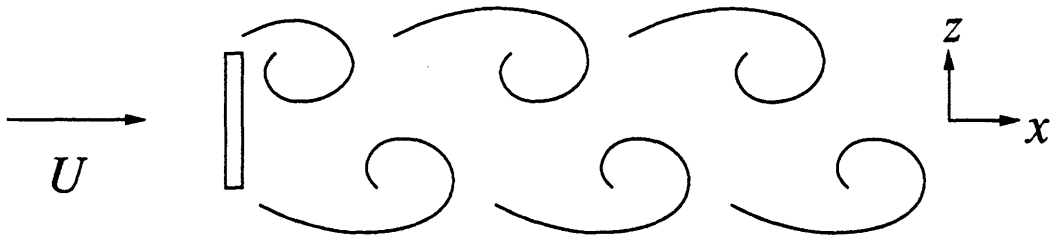

Figure B.1: Vortex shedding behind a flat plate normal to the incoming flow.

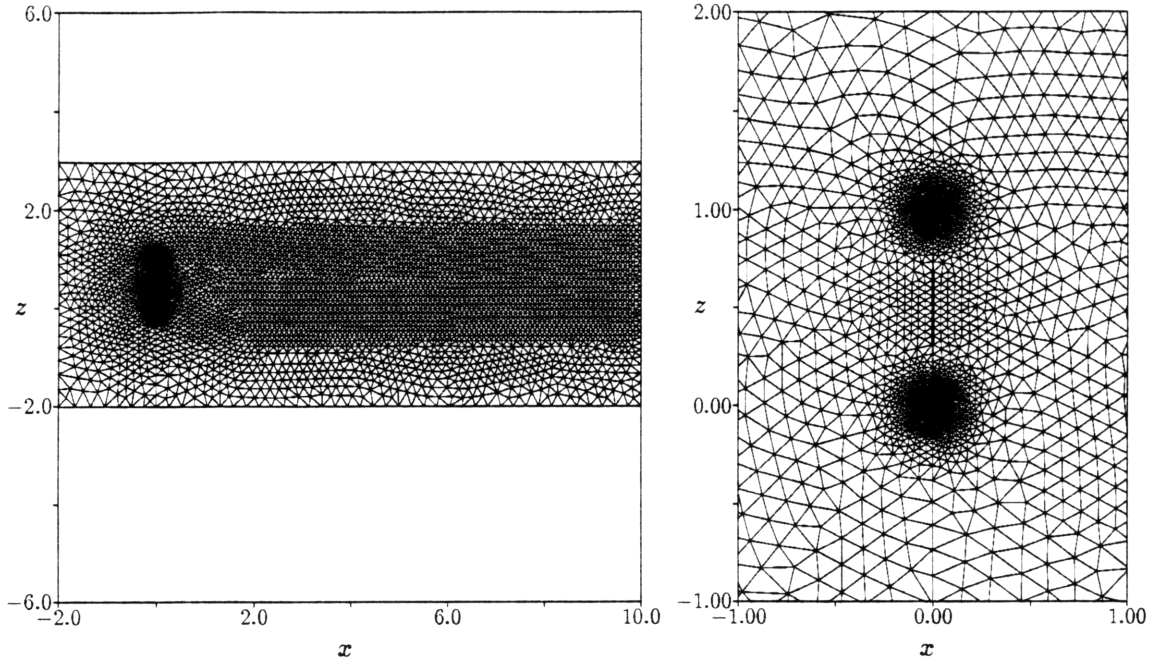

Figure B.2: Triangular mesh around the flat plate, with a closeup of the region near the plate.

this flow. Five distinct vortices can be seen, one of which is in the process of formation. Figure B.4 shows the variation of pressure coefficient on the surface of the plate. The most upstream vortex is associated with a strong suction peak.

Two calculations were performed using regional local time steps. The extent of the use of local time steps is quantified by the global time step acceleration factor, f, which is the ratio of the global time step to the minimum local time step. It is also the factor by which the number of iterations needed to integrate a fixed time interval is diminished. The values of f in the two calculations were 5 and 10. Figure B.5 shows the region of local time steps for the $f = 5$ case. Local time steps are confined to the region around the edges of the plate. When f is raised to 10, the region of local time steps includes the entire surface of the plate, and extends about one third of the width of the plate downstream, at the plate midpoint. This includes the region in which the vortices form. Figure B.6 shows the temporal variation of the drag coefficient on the plate, during two periods of vortex formation. The $f = 10$ case is clearly inaccurate, while the $f = 5$ case shows the correct behavior, with a slight phase shift due to earlier transient behavior. These calculations demonstrate that reasonable time accuracy can be obtained using local time steps, provided that the region of local time steps does not include the areas

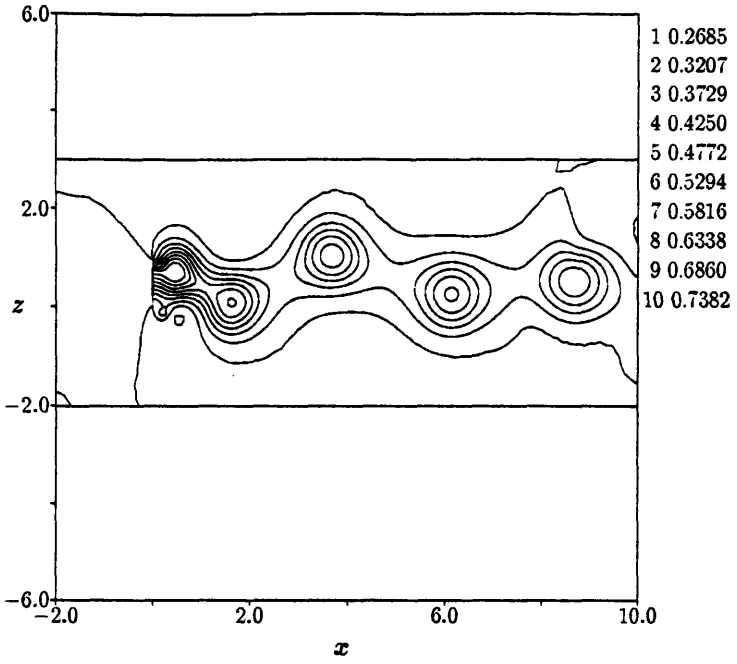

Figure B.3: Contours of pressure in the flow past the flat plate.

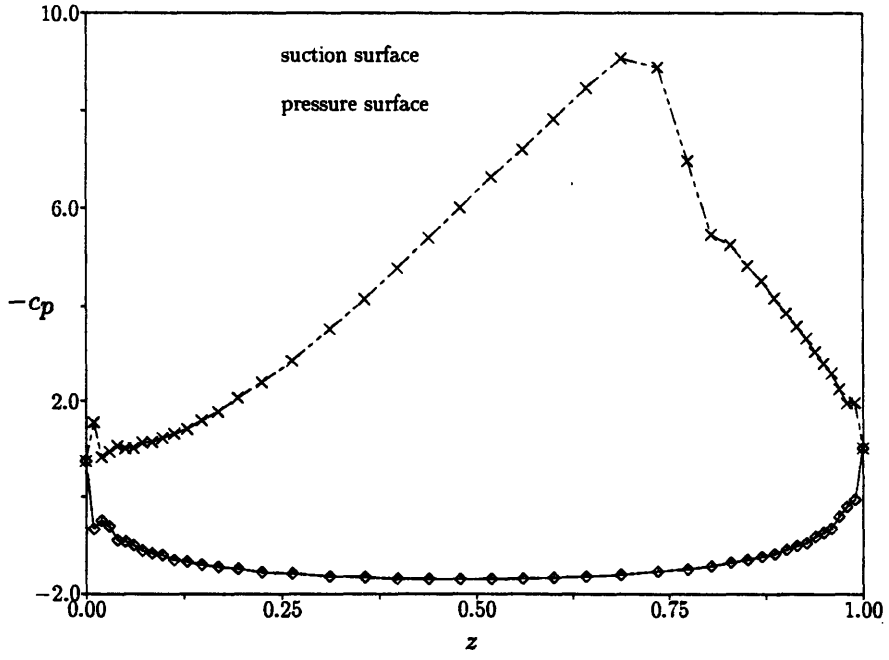

Figure B.4: Coefficient of pressure on the surface of the plate.

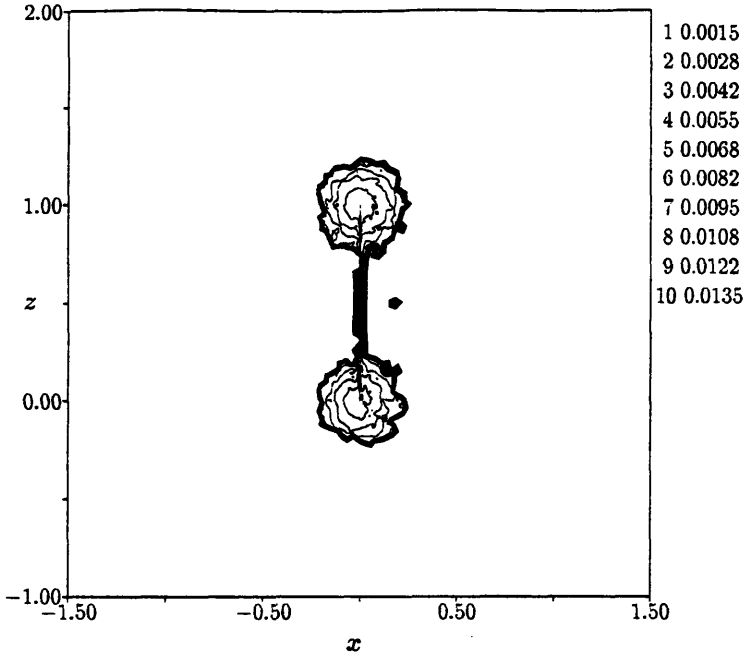

Figure B.5: Contours of time step in the region of local time steps, for a time step acceleration factor of 5.

of greatest unsteadiness.

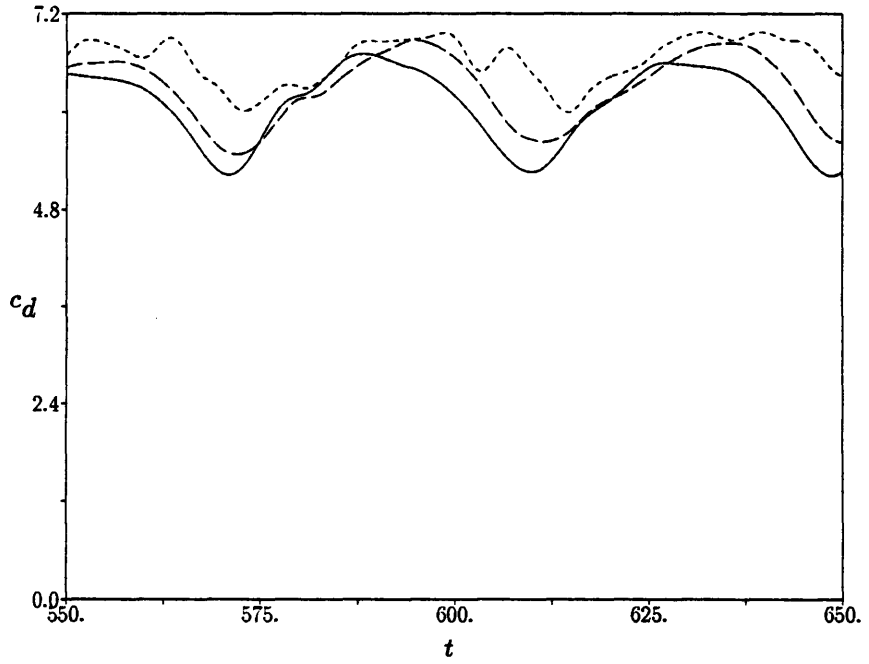

Figure B.6: Time history of drag coefficient on the flat plate at different values of the global time step acceleration factor. Solid line is strictly time accurate ($f = 1$); Dashed line is $f = 5$; Dotted line is $f = 10$.

Bibliography

[1] S. Agrwawal, R. M. Barnett, and B. A. Johnson. "Investigation of Vortex Breakdown on a Delta Wing Using Euler and Navier-Stokes Equations." In *Vortex Flow Aerodynamics*, AGARD-CP-494, Scheveningen, The Netherlands, October 1990.

[2] F. R. Bailey and J. L. Steger. "Relaxation Techniques for Three-Dimensional Transonic Flow About Wings." AIAA Paper 72-189, January 1972.

[3] T. J. Baker. "Three Dimensional Mesh Generation by Triangulation of Arbitrary Point Sets." AIAA Paper 87-1124, 1987.

[4] T. J. Barth. "Numerical Aspects of Computiong Viscous High Reynolds Number Flows Using Unstructured Meshes." AIAA Paper 91-0721, 1991.

[5] J. T. Batina. "CFD Methods Development Considerations for Unsteady Aerodynamic Analysis.". 1992. Presented at the Workshop on Computational Aeronautics.

[6] J. T. Batina. "A Fast Implicit Upwind Solution Algorithm for Three-Dimensional Unstructured Dynamic Meshes." AIAA Paper 92-0447, January 1992.

[7] J. T. Batina. "Unsteady Aerodynamics Methods for Transonic Aeroelastic Analysis.". April 1989. Presented at the European Forum on Aeroelasticity and Structural Dynamics 1989.

[8] J. Bell, M. Berger, J. Saltzman, and M. Welcome. *Three Dimensional Adaptive Mesh Refinement for Hyperbolic Conservation Laws.* Technical Report UCRL-JC-108794, Lawrence Livermore National Laboratory, December 1991. Submitted to SIAM Journal of Scientific Statistical Computing.

[9] M. J. Berger and J. Oliger. "Adaptive Mesh Refinement for Hyperbolic Partial Differential Equations." *Journal of Computational Physics*, 43:484–512, 1984.

[10] M. Borsi, L. Formaggia, E. Hettena, S. Santillan, V. Selmin, and S. Tarditi. "Vortical Flow Simulation by Using Structured and Unstructured Grids." In *Vortex Flow Aerodynamics*, AGARD-CP-494, Scheveningen, The Netherlands, October 1990.

[11] N. M. Chaderjian. "Navier-Stokes Prediction of Large-Amplitude Delta-Wing Roll Oscillations Characterizing Wing Rock." AIAA Paper 92-4428, August 1992.

[12] R. D. Cook, D. S. Malkus, and M. E. Plesha. *Concepts and Applications of Finite Element Analysis.* John Wiley & Sons, 1989. Third Edition.

[13] J. F. Dannenhoffer III. *Grid Adaptation for Two-Dimensional Transonic Flow.* ScD thesis, M.I.T., August 1987.

[14] D. L. Darmofal. *The Role of Vorticity Dynamics in Vortex Breakdown. Preliminary Results.* Technical Report TR-92-3, MIT Computational Fluid Dynamics Laboratory, October 1992.

[15] J. E. Deese, R. K. Agarwal, and J. G. Johnson. "Calculation of Vortex Flowfields Around Forebodies and Delta Wings." AIAA Paper 91-0176, January 1991.

[16] P. B. Earnshaw. *An Experimental Investigation of the Structure of a Leading-Edge Vortex.* R & M 3281, Aeronautical Research Council, March 1961.

[17] J. A. Ekaterinas and L. B. Schiff. "Vortical Flows Over Delta Wings and Numerical Prediction of Vortex Breakdown." AIAA Paper 90-0102, January 1990.

[18] M. Escudier. "Vortex Breakdown: Observations and Explanations." *Prog. Aerospace Sci.*, 25:189–229, 1988.

[19] P. T. Fink and J. Taylor. *Some Early Experiments on Vortex Separation.* R & M 3489, Aeronautical Research Council, 1967.

[20] K. Fujii and P. Kutler. "Numerical Simulation of the Leading-Edge Separation Vortex for a Wing and Strake-Wing Configuration." AIAA Paper 83-1908, July 1983.

[21] M. B. Giles. *Energy Stability Analysis of Multi-Step Methods on Unstructured Meshes.* Technical Report TR-87-1, MIT Computational Fluid Dynamics Laboratory, March 1987.

[22] A. M. Goodsell. *3-D Euler Calculations of Vortex Flows Over Delta Wings.* Master's thesis, M.I.T., July 1987.

[23] W. S. Grabowski and S. A. Berger. "Solutions of the Navier-Stokes Equations for Vortex Breakdown." *Journal of Fluid Mechanics*, 75:525–544, 1976.

[24] R. Haimes and M. Giles. "VISUAL3: Interactive Unsteady Unstructured 3D Visualization." AIAA Paper 91-0794, January 1991.

[25] M. G. Hall. "Vortex Breakdown." *Annual Review of Fluid Mechanics*, 4:195–217, 1972.

[26] P.-M. Hartwich, C.-H. Hsu, J. M. Luckring, and C. H. Liu. "Numerical Study of the Vortex Burst Phenomenon for Delta Wings." AIAA Paper 88-0505, January 1988.

[27] D. G. Holmes and S. D. Connell. "Solution of the 2D Navier-Stokes Equations on Unstructured Adaptive Grids." AIAA Paper 89-1932, June 1989.

[28] D. Hummel. "On the Vortex Formation Over a Slender Wing at Large Angle of Incidence." In *High Angle of Attack Aerodynamics*, AGARD-CP-247, Paper 15, Sandefjord, Norway, October 1978.

[29] D. Hummel and P. S. Srinivasan. "Vortex Breakdown Effects on the Low-Speed Aerodynamic Characteristics of Slender Delta Wings in Symmetrical Flow." *Royal Aeronautical Society Journal*, 71:319–322, April 1967.

[30] A. Jameson and T. J. Baker. "Solution of the Euler Equations for Complex Configurations." AIAA Paper 83-1929-CP, in *AIAA Computational Fluid Dynamics Conference* proceedings, 1983.

[31] M. A. Jarrah. "Low-Speed Wind-Tunnel Investigation of Flow About Delta Wings, Oscillating in Pitch to Very High Angle of Attack." AIAA Paper 89-0295, January 1989.

[32] M. A. Jarrah. *Unsteady Aerodynamics of Delta Wings Performing Maneuvers to High Angle of Attack.* PhD thesis, Stanford University, December 1988.

[33] Y. Kallinderis, V. Parthasarathy, and J. Wu. "A New Euler Scheme and Adaptive Refinement/Coarsening Algorithm for Tetrahedra Grids." AIAA Paper 92-0446, January 1992.

[34] O. A. Kandil and H. A. Chuang. "Computation of Vortex-Dominated Flow for a Delta Wing Undergoing Pitching Oscillation." *AIAA Journal*, 28(9):1589–1595, September 1990.

[35] O. A. Kandil and H. A. Chuang. "Unsteady Vortex-Dominated Flows Around Maneuvering Wings Over a Wide Range of Mach Numbers." AIAA Paper 88-0217, January 1988.

[36] O. Kjelgaard and W. L. Sellers. *Detailed Flowfield Measurements Over a 75° Swept Delta Wing for Code Validations.* AGARD Symposium on Validation of CFD, Lisbon, Portugal, May 1988.

[37] S. O. Kjelgaard and W. L. Sellers III. "The Flowfield Over a 75 Degree Swept Delta Wing at 20.5 Degrees Angle of Attack." AIAA Paper 86-1775, June 1986.

[38] E. B. Klunker. *Contribution to Methods for Calculating the Flow About Thin Lifting Wings at Transonic Speeds — Analytic Expressions for the Far Field.* NASA Technical Note TN D-6530, November 1971.

[39] N. C. Lambourne and D. W. Bryer. *The Bursting of Leading-Edge Vortices — Some Observations and Discussions of the Phenomenon.* R & M 3282, Aeronautical Research Council, 1961.

[40] M. T. Landahl and S. E. Widnall. "Vortex Control." In *Aircraft Wake Turbulence and its Detection*, Plenum Press, 1971.

[41] A. M. Landsberg. *Adaptation for Vortex Flows using a 3-D Finite Element Solver.* Master's thesis, M.I.T., November 1990.

[42] N. K. W. Lee. *Evolution and Structure of Leading Edge Vortices over Slender Wings.* PhD thesis, M.I.T., March 1991.

[43] S. Leibovich. "Vortex Stability and Breakdown: Survey and Extension." *AIAA Journal*, 22(9):1192–1206, 1983.

[44] M. J. Lighthill. *Waves in Fluids.* Cambridge University Press, 1978.

[45] D. R. Lindquist. *A Comparison of Numerical Schemes on Triangular and Quadrilateral Meshes.* Master's thesis, M.I.T., May 1988.

[46] R. Löhner. "Finite Elements in CFD: What Lies Ahead.". September 1986. Invited Paper for the World Congress on Computational Mechanics.

[47] J. M. Lopez. "Axisymmetric Vortex Breakdown. Part 1. Confined Swirling Flow." *Journal of Fluid Mechanics*, 221:533–552, 1990.

[48] D. J. Mavriplis. "Three Dimensional Unstructured Multigrid for the Euler Equations." AIAA Paper 91-1549, 1991.

[49] D. J. Mavriplis and A. Jameson. "Multigrid Solution of the Euler Equations on Unstructured and Adaptive Meshes." In S. F. McCormick, editor, *ICASE Report 87-53, Proceedings of the Third Copper Mountain Conference on Multigrid Methods, Lecture Notes in Pure and Applied Mathematics*, pp. 413–430, Marcel Dekker, Inc., April 1987.

[50] S. N. McMillin, E. M. Murman, and J. L. Thomas. "Navier-Stokes and Euler Solutions for the Leeside Flow Over Supersonic Delta Wings." AIAA Paper 87-2270-CP, 1987.

[51] J. E. Melton, S. D. Thomas, and G. Cappucio. "Unstructured Euler Flow Solutions Using Hexahedral Cell Refinement." AIAA Paper 91-0637, January 1991.

[52] E. W. Meyer and K. G. Powell. "Similarity Solutions for Viscous Vortex Cores." *Journal of Fluid Mechanics*, 238:487–507, 1992.

[53] D. S. Miller and R. M. Wood. *Lee-Side Flow Over Delta Wings at Supersonic Speeds.* NASA Technical Paper TP 2430, June 1985.

[54] B. Müller and A. Rizzi. "Navier-Stokes Computations of Transonic Vortices Over a Round Leading Edge Delta Wing." AIAA Paper 87-1227, 1987.

[55] E. M. Murman and A. Rizzi. "Applications of Euler Equations to Sharp Edge Delta Wings with Leading Edge Vortices." In *Applications of Computational Fluid Dynamics in Aeronautics*, AGARD-CP-412, 1986.

[56] L. T. Nguyen, L. Yip, and J. R. Chambers. "Self-Induced Wing Rock of Slender Delta Wings." AIAA Paper 81-1983, August 1981.

[57] F. M. Payne, T. T. Ng, R. C. Nelson, and L. B. Schiff. "Visualization and Flow Surveys of the Leading Edge Vortex Structure on Delta Wing Planforms." AIAA Paper 86-0330, January 1986.

[58] D. H. Peckham and S. A. Atkinson. *Preliminary Results of Low Speed Wind Tunnel Tests on a Gothic Wing of Aspect Ratio 1.0.* CP-508, Aeronautical Research Council, 1957.

[59] J. Peraire, K. Morgan, and J. Peiró. "Unstructured Finite Element Mesh Generation and Adaptive Procedures for CFD." In *Application of Mesh Generation to Complex 3-D Geometries*, AGARD-CP-464, Loen, Norway, May 1989.

[60] J. Peraire, J. Peiró, and K. Morgan. "A 3D Finite Element Multigrid Solver for the Euler Equations." AIAA Paper 92-0449, January 1992.

[61] J. Peraire, J. Peiró, and K. Morgan. *LISA User Manual (Draft).* November 1991.

[62] J. Peraire, M. Vahdati, K. Morgan, and O. C. Zienkiewicz. "Adaptive Remeshing for Compressible Flow Equations." *Journal of Computational Physics*, 72:449–466, 1987.

[63] E. C. Polhamus. "Prediction of Vortex-Lift Characteristics Based on a Leading-Edge Suction Analogy." AIAA Paper 69-113, October 1963.

[64] K. G. Powell. *Vortical Solutions of the Conical Euler Equations.* PhD thesis, M.I.T., July 1987. Also published as *Notes on Numerical Fluid Mechanics, Vol. 28*, by Friedr. Vieweg & Sohn Verlagsgesellschaft mbH, Braunschweig, FRG, 1990.

[65] K. G. Powell, M. A. Beer, and G. W. Law. "An Adaptive Embedded Mesh Procedure for Leading-Edge Vortex Flows." AIAA Paper 89-0080, January 1989.

[66] R. D. Rausch, J. T. Batina, and H. T. Y. Yang. "Spatial Adaptation Procedures on Unstructured Meshes for Accurate Unsteady Aerodynamic Flow Computation." AIAA Paper 91-1106, April 1991.

[67] A. Rizzi and C. J. Purcell. "On the Computation of Transonic Leading-Edge Vortices Using the Euler Equations." *Journal of Fluid Mechanics*, 181:163–195, August 1987.

[68] A. W. Rizzi and L.-E. Eriksson. "Computation of Flow Around Wings Based on the Euler Equations." *Journal of Fluid Mechanics*, 148:45–71, November 1984.

[69] F. W. Roos. Personal communication.

[70] F. W. Roos and J. T. Kegelman. "An Experimental Investigation of Sweep-Angle Influence on Delta-Wing Flows." AIAA Paper 90-0383, January 1990.

[71] F. W. Roos and J. T. Kegelman. "Recent Explorations of Leading-Edge-Vortex Flowfields.". In NASA CP-3149. Presented at NASA High-Angle-of-Attack Conference, 30 October – 1 November 1990.

[72] T. Sarpkaya. "On Stationary and Travelling Vortex Breakdowns." *Journal of Fluid Mechanics*, 45:545–559, 1971.

[73] A. Saxer. *A Numerical Analysis of 3-D Inviscid Stator/Rotor Interactions Using Non-Reflecting Boundary Conditions.* PhD thesis, M.IT., June 1992.

[74] R. A. Shapiro. *An Adaptive Finite Element Solution Algorithm for the Euler Equations.* PhD thesis, M.I.T., May 1988.

[75] D. C. Slack, R. W. Walters, and R. Löhner. "An Interactive Adaptive Remeshing Algorithm for the Two-Dimentsional Euler Equations." AIAA Paper 90-0331, January 1990.

[76] A. Stanbrook and L. C. Squire. "Possible Types of Flow at Swept Leading Edges." *Aeronautical Quarterly*, 15(1):72–82, February 1964.

[77] G. Strang. *Introduction to Applied Mathematics.* Wellesley-Cambridge Press, Wellesley, Massachusetts, 1986.

[78] T. S. Tavares. *Aerodynamics of Meneuvering Slender Wings with Leading-Edge Separation.* PhD thesis, M.I.T.., 1990.

[79] R. R. Thareja, J. R. Stewart, O. Hassan, K. Morgan, and J. Peraire. "A Point Implicit Unstructured Grid Solver for the Euler and Navier-Stokes Equations." AIAA Paper 88-0036, January 1988.

[80] J. L. Thomas, S. T. Krist, and W. K. Anderson. "Navier-Stokes Computations of Vortical Flows Over Low-Aspect-Ratio Wings." AIAA Paper 87-0207, January 1987.

[81] S. Thompson, S. Batill, and R. Nelson. "The Separated Flow Field on a Slender Delta Wing Undergoing Transient Pitching Motions." AIAA Paper 89-0194, January 1989.

[82] W. J. Usab, Jr. *Embedded Mesh Solutions of the Euler Equation Using a Multiple-Grid Method.* PhD thesis, M.I.T., December 1983.

[83] G. Vemaganti, E. Thornton, and A. Wieting. "A Structured and Unstructured Remeshing Method for High Speed Flows." AIAA Paper 90-0401, January 1990.

[84] N. Verhaagen and P. van Ransbeeck. "Experimental and Numerical Investigation of the Flow in the Core of a Leading Edge Vortex." AIAA Paper 90-0384, January 1990.

[85] N. G. Verhaagen and A. C. H. Kruisbrink. "The Entrainment Effect of a Leading-Edge Vortex." AIAA Paper 85-1584, July 1985.

[86] G. P. Warren, W. K. Anderson, J. L. Thomas, and S. L. Krist. "Grid Convergence for Adaptive Methods." AIAA Paper 91-1592, June 1991.

[87] W. P. Webster and J. S. Shang. "Numerical Simulation of Vortex Breakdown Over a Delta Wing." AIAA Paper 91-1814, June 1991.